
Generation, characterization and sub-cycle shaping of intense, few-cycle light waveforms for attosecond spectroscopy

Bálint Horváth



München 2009

Generation, characterization and sub-cycle shaping of intense, few-cycle light waveforms for attosecond spectroscopy

Bálint Horváth

Dissertation
an der Fakultät für Physik
der Ludwig-Maximilians-Universität
München

vorgelegt von
Bálint Horváth
aus Salgótarján, Ungarn

München, den 26. Mai 2009

Erstgutachter: Prof. Dr. Ferenc Krausz

Zweitgutachter: Prof. Dr. Wolfgang Zinth

Tag der mündlichen Prüfung: 22. Juni 2009

Abstract

Our desire to observe electron dynamics in atoms and molecules on their natural time-scale with the tools of attosecond physics demands ever shorter laser pulse durations. The reliance of this young field on laser pulses is understandable: both the generation and the characterization of attosecond pulses, as well as time-resolved measurements directly use the electrical field that lasts only for a few oscillations of the wave.

This also means that exerting control over the evolution of the waveform on a sub-cycle scale can modify the characteristics of attosecond pulses and possibly in a favorable way. In this thesis we introduce a laser system that provides near single-cycle laser pulses and generate through their interaction with gases coherent XUV radiation. Our measurements indicate that the thus produced XUV spectrum supports the potential compressibility to an isolated attosecond pulse of a sub-100 as duration. Considering our already broadband fundamental laser spectrum, we demonstrate moreover a technique to further enhance our spectral intensity in the blue. By frequency-doubling a part of the original spectrum, and controlling the time-delay between the two harmonic laser pulses we show that we can induce a change in the waveform on an attosecond time-scale, suppress or increase some half-cycles or change the effective wavelength of the laser light. Our method's influence on the generation of XUV light is tested via spectral characterization, and we found that broad tunability of the central XUV-energy is possible by a change of the time-delay between the fundamental and the second-harmonic laser pulses. Our results furthermore give strong evidence that waveform-dependent interference of two quantum-paths was observed, which effect comes from two electron-trajectories that are inside one half-cycle of the laser field.

It is also of utmost importance to know the level of control over the waveform. To characterize the waveform, we demonstrate here the first single-shot measurement of the carrier-envelope phase (CEP) of a lightpulse. We measured with no phase-ambiguity the CEP of high repetition-rate (3 kHz) non-phase-stabilized and phase-stabilized laser pulses consecutively with an unprecedented measurement precision. Our method uniquely requires no prior phase-stabilization. It opens the door to CEP-tagging with non-phase-stabilized pulses using emerging few-cycle laser systems with relativistic peak intensities.

Zusammenfassung

Unser Wunsch die Elektronendynamik in Atomen und Molekülen auf ihrer natürlichen Zeitskala mit den Werkzeugen der Attosekundenphysik zu untersuchen erfordert immer kürzere Laserpulse. Das Vertrauen dieser neuartigen Wissenschaft auf Laserpulse ist verständlich: sowohl die Erzeugung als auch die Charakterisierung von Attosekundenpulsen, wie auch die zeitaufgelösten Experimente nutzen das elektrische Feld, welches nur wenige Oszillationen andauert.

Dies bedeutet auch, dass die Kontrolle über die Entstehung einer Wellenform auf einer Zeitskala von weniger als einer Oszillation des fundamentalen Lichtes die Eigenschaften eines Attosekundenlaserpulses beeinflusst und dies möglicherweise in einer vorteilhaften Art und Weise. In dieser Arbeit stellen wir ein Lasersystem vor, welches Laserpulse mit einer Dauer nahe der Periodendauer des sichtbaren Lichtes zur Verfügung stellt und durch die Wechselwirkung mit Gasen kohärente XUV-Strahlung erzeugt. Unsere Messungen deuten darauf hin, dass das dadurch erzeugte XUV-Spektrum die mögliche Kompression zu einem isolierten Attosekundenpulse mit weniger als 100 as Pulsdauer unterstützt. In Anbetracht unseres bereits breitbandigen fundamentalen Spektrums zeigten wir darüber hinaus eine Methode zur weiteren Verstärkung der spektralen Intensität mit kürzerer Wellenlänge. Durch die Frequenzverdopplung eines Teiles des ursprünglichen Spektrums und die Kontrolle der zeitlichen Verzögerung zwischen der Fundamentalen und der zweiten Harmonischen zeigen wir, dass wir eine Änderung der Wellenform auf einer Attosekundenzeitskala herbeiführen, die Amplituden der verschiedenen Halbzyklen entweder verstärken oder verringern und die effektive Wellenlänge des Laserlichtes ändern können. Der Einfluss unserer Methode auf die Erzeugung von XUV-Licht wurde durch eine spektrale Charakterisierung getestet und wir fanden, dass eine breite Verschiebung der zentralen XUV-Wellenlänge durch die Änderung der zeitlichen Verzögerung zwischen Fundamentaler und zweiter Harmonischer des Laserlichtes möglich ist. Des weiteren geben unsere Ergebnisse einen deutlichen Hinweis darauf, dass eine von der Wellenform abhängige Interferenz zwischen verschiedenen Quantenwegen beobachtet wurde, welche durch zwei Elektronentrajektorien innerhalb eines Laserhalbzyklus' verursacht werden.

Ebenso ist die Kenntnis über die Kontrolle der Wellenform von größter Bedeutung.

Um die Wellenform zu charakterisieren demonstrieren wir hier die erste Einzelschussmessung der absoluten Phase (CEP) eines Lichtpulses. Wir maßen mit bisher unerreichter Präzision und ohne Zweideutigkeit die absolute Phase eines nicht phasenstabilisierten und darauf folgend eines phasenstabilisierten Laserpulses mit hoher Repetitionsrate (3 kHz). Unsere Methode erfordert in einer einmaligen Art und Weise keine vorgeschaltete Phasenstabilisierung. Sie ermöglicht das Verfolgen der absoluten Phase eines nicht phasenstabilisierten Laserpulses der aufkommenden Lasersysteme mit Pulsdauern von nur wenigen Zyklen und relativistischen Intensitäten.

Publications

Journal articles

Publications that are included in the thesis are marked with *. The entries for both lists below have been arranged in reverse chronological order.

- 1* T. Wittmann, **B. Horvath**, W. Helml, M. G. Schätzel, X. Gu, A. L. Cavalieri, G. G. Paulus, R. Kienberger
Single-shot carrier-envelope phase measurement of few-cycle laser pulses.
Nature Physics, **5**, 357–362 (2009).
- 2* **B. Horvath**, M. Fieß, T. Wittmann, J. Gagnon, B. Zeng, Y. Cheng, Z. Xu, V. S. Yakovlev, E. Goulielmakis, R. Kienberger, F. Krausz
Shaping of single-cycle waveforms for tunable XUV continuum generation.
In preparation.
- 3* A. L. Cavalieri, E. Goulielmakis, **B. Horvath**, W. Helml, M. Schultze, M. Fieß, V. Pervak, L. Veisz, V. S. Yakovlev, M. Uiberacker, A. Apolonski, F. Krausz, R. Kienberger.
Intense 1.5-cycle near infrared laser waveforms and their use for the generation of ultra-broadband soft x-ray harmonic continua.
New Journal of Physics, **9**, 242 (2007).
- 4 A. L. Cavalieri, N. Müller, Th. Uphues, V. S. Yakovlev, A. Baltuska, **B. Horvath**, B. Schmidt, L. Blümel, R. Holzwarth, S. Hendel, M. Drescher, U. Kleineberg, P. M. Echenique, R. Kienberger, F. Krausz, U. Heinzmann
Attosecond spectroscopy in condensed matter.
Nature, **449**, 1027 (2007).
- 5 J. A. Fülöp, Z. Major, **B. Horvath**, F. Tavella, A. Baltuška, F. Krausz
Shaping of picosecond pulses for pumping optical parametric amplification.
Appl. Phys. B, **87**, 79 (2007)

- 6 T. Bánky, **B. Horváth**, T. Berceci
Optimum configuration of multiloop opto-electronic oscillators.
JOSA B, **23**, 1371 (2006).
- 7 T. Berceci, T. Bánky, **B. Horváth**,
Opto-electronic generation of stable and low noise microwave signals.
IEE Proc.- Optoelectron, **153**, 3 (2006).

Conference contributions

In the list below the presenter has been indicated by an underline.

- * T. Wittmann, **B. Horvath**, W. Helml, M. G. Schätzel, X. Gu, A. L. Cavalieri, G. G. Paulus, R. Kienberger
Single-shot carrier-envelope phase measurement of few-cycle laser pulses.
Ultrafast Phenomena, Stresa, Italy (2009).
- T. Bánky, **B. Horvath**, T. Berceci, V. Polo
Reliability of the design method for optimized multiloop opto-electronic oscillators.
MIKON, Wroclaw, Poland (2008).
- * **B. Horvath**, A. L. Cavalieri, V. Pervak, X. Gu, W. Helml, T. Wittmann, F. Tavella, L. Veisz, A. Apolonski, R. Kienberger, F. Krausz
Latest developments in harmonic continuum generation.
XTRA meeting, Lund, Sweden (2007).
- F. Tavella, T. Wittmann, K. Schmid, **B. Horvath**, A. L. Cavalieri, L. Veisz, A. Marcinkevicius, F. Krausz
Stronger seed for a multi-terawatt few-cycle OPCPA.
postdeadline at CLEO Europe/EQEC, Munich, Germany (2007).
- **B. Horvath**, V. S. Yakovlev, F. Krausz
Numerical and Experimental Studies of Optical Parametric Chirped-Pulse Amplification.
XTRA meeting, London, UK (2006).
- **B. Horváth**, T. Bánky, T. Berceci
Short-term Stabilization of Opto-Electronic Oscillators with Multiple Optical Resonators.
Int. Topical Meeting on Microwave Photonics, Ogunquit, USA (2004).

Contents

Abstract	i
Zusammenfassung	iii
Publications	v
Contents	vii
1 Introduction	1
Outline of the thesis	5
2 Atoms in strong laser fields	9
2.1 Strong field phenomena	9
2.2 The three-step model	10
2.2.1 Ionization	11
2.2.2 Acceleration	13
2.2.3 Recombination or re-scattering	16
2.3 Above-threshold ionization (ATI)	16
2.3.1 Phase sensitivity of re-scattered ATI spectra	18
2.3.2 Macroscopic effects - volume effects	20
2.4 High-harmonic generation (HHG)	20
2.4.1 Macroscopic effects - phase matching	22
2.4.2 Isolated attosecond pulse generation	24
2.4.3 Broadband HHG with a 1.5-cycle pulse	28
3 1.5-cycle carrier-envelope phase-stabilized laser system	33
3.1 The laser system	34
3.1.1 Oscillator	34
3.1.2 Multi-pass amplifier and hybrid prism/chirped-mirror compressor	35
3.1.3 Hollow-core fiber and chirped-mirror compressor	38

3.2	Carrier-envelope phase-stabilization	42
3.2.1	The carrier-envelope phase (CEP)	42
3.2.2	Fast compensation of the CEP change - f-to-0 method	44
3.2.3	Slow compensation of the CEP change - f-to-2f method	45
3.3	Summary	47
4	Single-shot CEP measurement of intense few-cycle laser pulses	49
4.1	Introduction	49
4.2	Single-shot stereo-ATI measurement apparatus	51
4.3	Conventional representation of phase-stabilized pulses	52
4.4	Parametric representation of non-phase-stabilized pulses	57
4.5	Precision of the CEP measurement	62
4.6	Complete characterization of CEP-stabilization	66
4.7	Dispersion-free pulse duration measurement	71
4.8	Summary	75
5	HHG with broadband two-color waveforms	77
5.1	Introduction	77
5.2	Control of electron trajectories	80
5.3	Analysis of the collinear setup	84
5.3.1	Second-harmonic generation (SHG) crystal	89
5.3.2	Timeplate	92
5.3.3	Waveplate	94
5.3.4	Pellicles	97
5.4	Experimental results and theoretical analysis	98
5.4.1	CEP slippage due to the SHG crystal	99
5.4.2	Time-scans	100
5.4.3	Broadly and finely tunable continuum source in the XUV	102
5.4.4	Comparison of isolated attosecond pulse purities	105
5.4.5	Quantum path interference within a half-cycle	108
5.5	Summary	110
6	Conclusions and outlook	113
A	XUV transmission of common materials	117
	Bibliography	119
	Acknowledgements	135

Chapter 1

Introduction

In the macroscopic world the majority of events happening around us are observable with our eyes. When processes occur on a time-scale that we cannot follow, a camera is usually employed. Driven by our desire to track and finally understand phenomena that unfold in a world that is hidden from our eyes, we try to take snapshots of the microcosm, as well. Unfortunately, normal cameras, such as charge-coupled devices are not good enough for the observation of events that happen extremely fast, such as the motion of atoms and electrons - not even the world's fastest camera can capture the dynamics with enough frame and shutter speed [1].

This lack of an appropriate device called for a new approach. The invention of the laser by T. H. Maiman at Hughes Research Labs in 1960 [2] inaugurated a new era in science. Ultrafast physics [3] and nonlinear optics [4] emerged shortly after the first successfully operating laser and they provided the solution to the above problem: light pulses were produced that could act as fast shutters for temporally resolving the fastest dynamical processes in nature. Most interestingly, light fields not only allowed us to time-resolve dynamic events, but they gave us the power to control them, as well. Namely, the electrical field strengths of a light pulse can be so huge that it became possible to apply them to form and break molecular bonds, control chemical reactions [5], influence the motions of electrons in atoms, which we can call light-field induced manipulation of the small constituents of matter. We can already see that these are unique conditions: observation and control go hand in hand.

When spatial dimensions shrink, the motion of electrons will be more and more confined in space. Quantum-mechanics dictates that at the same time the separation of energy levels of a system will also change and in turn the associated time-scales will vary. A particle can be regarded as a wavepacket, which is a superposition of a number of energy states, and this particle's (an electron's for example) oscillatory motion will connect these two concepts. If the constituent states of the superposition are far away in energy,

the period of the particle's oscillatory motion will be short. The millielectronvolt (meV) energy spacing of the vibrational energies of a molecule entails a time-scale that is in the femtosecond regime. The motion of atoms in molecules happens also with such a speed and they form the operational ground for a field, called femtochemistry. Ultrafast lasers that have been capable of routinely generating femtosecond pulses permitted access to this area of research. The revolution that took place in it is also indicated by the Nobel prize of 1999 that was given to A. Zewail for his contributions to unveiling the potentials of femtochemistry [5]. In this field and in attosecond physics [6] for studying physical processes in a time-resolved manner the pump-probe scheme became ubiquitously used. In such a setup isolated pulses are used, where a pump pulse puts the system into an electronically excited state, and another pulse subsequently probes the evolution of the system at various time instances. Information on the evolution will be encoded either on the probe pulse, or on photons, ions or electrons that are born along the way. This is the essence of time-resolved spectroscopy. Evidently, other methods, such as purely frequency-domain spectroscopy is not relevant here if our goal is to investigate transient phenomena or the response of a nonlinear system.

On even smaller dimensions, on the level of atoms, for our studies attosecond resolution becomes necessary. For example, the quantum-mechanical "breathing" of the superposition state of the 1S-2S levels of Hydrogen has an associated period of 400 as. Going more and more deeper inside atoms, where the energy spacing becomes larger and larger we even start to approach the atomic unit of time, which is 24 as. Attosecond physics in its current implementation which relies on attosecond streaking uses both a laser pulse (probe) that has a strong, high gradient electrical field, with a rise-time already in the attosecond range, and an attosecond pulse (pump) that can liberate bound electrons. In fact, such a scheme is used not only for tracking the evolution of fundamental processes but also for characterizing both of these pulses [7, 8]. It is basically a variation of the streak camera [9], where the time-evolution of a light pulse is mapped into a distribution of electrons in space by a fast-varying electrical field. In the version of its attosecond implementation, it is the high gradient laser electric field that acts as the streaking field to create in energy a distribution of the photoelectrons. Attosecond streaking has allowed us so far to access a plethora of electron dynamics, the first one being that of Auger-decay [10], while the latest ones being shake-up [11] (both connected to the rearrangement of the electrons after photoionization), and energy-band dependant photoemission in solids [12], to name a few. More experiments are expected to follow as collective motion of electrons (plasmons) on surfaces [13], charge-transfer in molecular structures, electron-electron interactions all happen on an attosecond time-scale.

Femtosecond and attosecond spectroscopy were born because of technological break-

throughs in the last decades. Laser mode-locking is the mechanism for ultra-short pulse formation in an oscillator [14, 15] which requires that millions of longitudinal modes (which constitute a frequency comb) that a cavity can support become simultaneously phase-locked. Interference phenomenon manifests itself here that through constructive and destructive wave-addition for frequency components in a wide spectral range allows the generation of a train of short and intense pulses. For ultrafast lasers passive mode-locking proved to be the most favorable way of achieving short pulses. These type of lasers employ a passive nonlinear material that exhibits a lower loss for high intensities, which leads to the efficient build-up of a pulse after many round-trips in the cavity. First fast saturable absorbers were used as a nonlinear medium [3]. Together with organic dyes as active medium, these lasers were the most common tools of femtosecond spectroscopy until the 80's, when the pulse duration achieved by another active medium, Ti:Sa reached the same value and soon surpassed it. Today Ti:Sa-based oscillators produce the shortest few-cycle pulses, the achievable pulse duration being below two-cycles, that is less than 5 fs at 800 nm (for reviews see [16, 17] or a more recent one [18]). For them the saturable absorber-like effect is embodied by the Kerr-lens effect that causes both self-phase modulation (SPM) and self-amplitude modulation (SAM). Going into the sub-10 fs pulse generation regime with Ti:Sa oscillators required another breakthrough in ultrafast science, which is the precision-dispersion-control with Chirped-Mirrors (CM) [19]. They are used nowadays virtually in every short-pulse oscillator and also for compression of amplified pulses [20, 21].

The single-cycle pulse duration (2.6 fs at 800 nm) imposed apparently a limit to further pulse shortening. Breaking the femtosecond-barrier became only possible by moving to shorter wavelengths [22]. It was already proposed in the '90s that gases could be ideal candidates for reaching sub-femtosecond durations by using lasers [23, 24]. It was high-harmonic generation (HHG), a strong-field phenomenon, which provided a solution for the frequency-conversion that was necessary to go from 1.55 eV (800 nm) to 100 eV (12.4 nm). The high peak intensities of the ultrashort laser pulses are most ideal also for influencing other strong-field processes, such as above-threshold ionization (ATI), non-sequential double-ionization (NSDI). It is a common feature of them that they are all sensitive to the electrical field and thus to its exact time-evolution inside a pulse. In very recent times we have been witnessing another major achievement, which is the control of the shape of the electrical field. This control in the time-domain came about due to a breakthrough in research in the frequency-domain, in frequency metrology. The frequency comb of a mode-locked laser in that research discipline serves as a ruler that helps in the determination of an unknown frequency. Unfortunately, such a comb is not static by nature, but its location dynamically moves. Access to and subsequently control of

the lowest frequency component, called offset frequency [25, 26], revolutionized frequency metrology, indicated also by the Nobel prize of 2005 having been awarded to T. W. Hänsch and J. Hall. In attosecond science such a control permitted a reproducible generation of isolated attosecond pulses [27], which heralded the time of lightwave-electronics [28].

In nano-science the use of Atomic Force [29] and Scanning-Tunneling Microscope [30] have already become the working tools not only for observing the nano-world, but also for atomic manipulations, for placing atoms to certain locations. Specific light waveforms can also act like tiny robotic hands, but now for carrying out manipulations on individual electrons. Such waveform-controlled placement of electrons in molecules was first demonstrated via the attachment of electrons to a specific molecule during the dissociative ionization of deuterium (D_2) [31]. To gain even more control, by taking frequency components from a multi-octave spectral bandwidth waveform-synthesis strives to construct electrical fields that we have not seen before: single and sub-cycle pulses, saw-tooth-like ramp-up, square-like on-off switching of the field. Naturally, not only a broad enough spectral span has to be available [32] for tailoring the waveform, but also amplitude and phase control over such spectral bandwidth has to be performed. Especially dispersion control is most difficult to attain; but the technology of chirped-mirrors is constantly evolving [33] and it shows huge potentials for overcoming this problem. In the work that is outlined in this thesis we carried out broadband two-color waveform synthesis with a simple setup. We added up two pulses, one of a near-single-cycle duration, and another that is its second-harmonic. We furthermore, showed its usefulness for HHG.

It is of utmost importance also to know what degree of control we have achieved. To this end, we again had to step out of the perturbative regime of optics and relied on ATI to measure the alignment of the phase of the lightwave inside the pulse. Fig. 1.1 illustrates a few selected waveforms that allows us to conclude that there are an unlimited amount of ways to draw an electrical field-shape for a certain pulse duration. The figure also shows that as a direct consequence of the various field evolutions, the response of strong-field phenomena (in the fig. HHG) will differ between one pulse shape and another [27, 34]. In this thesis we used the phase-dependent effect in ATI to determine the phase of individual laser pulses [35].

We can also turn around the idea. If one wants to see the effect of all the outcomes of a control over the waveform, what would be the most efficient way of achieving this? We have developed a method, based on our single-shot phase measurement capabilities, that can do exactly this. Before, phase-stabilized lasers had to be used to perform measurements, even to measure the phase [36]; from now on, however, it will be possible to perform a scan (by continuing the above analogy to scan the robotic arm) over the phase by using non-phase-stabilized pulses from a laser. So-called CEP-tagging is within reach,

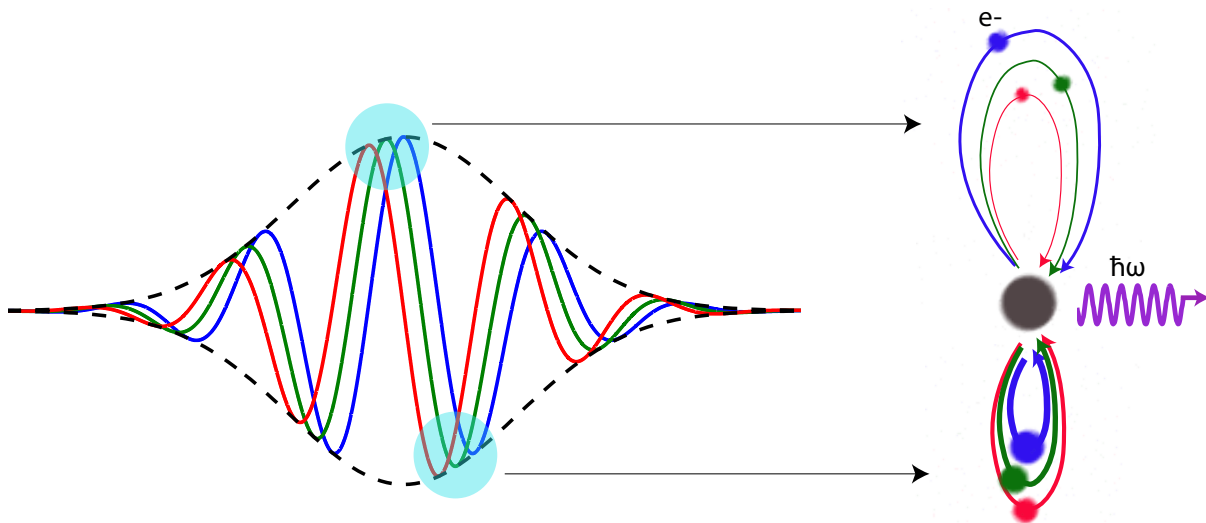


Figure 1.1: Illustration of various waveforms and the sensitivity of strong-field processes, such as HHG that leads to the emission of a photon. Black dashed line is the pulse shape (envelope), which is here Gaussian, while the colored lines correspond to three different electric field alignments under the envelope. To the right the motion of the electrons can be seen that can be accelerated in two consecutive half-cycles (semi-transparent light magenta circles) of the laser pulse. The thickness of the 'loops' and the size of the electrons (filled circles) are proportional to the number of liberated electrons.

which means that in every experiment the information on the phase of the lightwave with the highest demonstrated precision (to be discussed in this thesis) will be on hand and requiring no stabilization of the phase. Importantly, few-cycle lasers in high intensity versions [37, 38] without phase-stabilization are already available. Employing these sources will give access to nonlinear optics with extreme ultraviolet pulses, as well as allow us to carry out experiments with a well-known waveform in the relativistic optics regime, where intensities beyond $10^{18} \text{ W cm}^{-2}$ are needed.

Outline of the thesis

The main topic in this thesis is studying the shaping possibilities of near-single-cycle pulses by using another pulse that is a second-harmonic of the fundamental. The spectral measurements were performed in collaboration with Markus Fieř. Both of us were involved in the HHG generation and the final test of our collinear setup. His work and topic focuses mainly on streaking measurements. He set up the beamline to which I also assisted. Beyond our common work, however, I chose all the optics elements of our setup through theoretical calculations; tested each of them experimentally; conceived the initial setup. Moreover, I carried out a feasibility study by relying on the classical trajectory calculation code that I wrote to assess the effect of the two-color waveform on HHG. I was in

charge of the analysis of the spectral measurements, as well, which has proceeded in close collaboration with Ya Cheng's group (Shanghai Institute of Optics and Fine Mechanics) and Justin Gagnon (MPQ). In fact Prof. Cheng's group carried out the single-atom response calculations, which support our claims. The laser that we used for the experiments was set up mostly through the work by A. L. Cavalieri and me, with alignments carried out by me during our experiments.

Regarding the single-shot phase meter measurements, T. Wittmann built the single-shot device; I took part in the single-shot measurements, and with him we developed our novel analysis method.

The results that are presented in this thesis can be structured as follows:

- *Chapter 2* provides an introduction to the underlying physics that we build on throughout thesis, with special emphasis given to above-threshold ionization (ATI) and high-harmonic generation (HHG). These two have become one of the most important phenomena in strong-field science that describe the response of media to an intense laser pulse, in our case to an extremely short, a sub-two-cycle pulse. Numerical calculations will be shown that illustrate the basic concepts of both ATI and HHG. In this chapter experimental results will also be discussed that give strong evidence of the interaction of a near-single-cycle pulse with a noble gas through HHG. This type of pulse will serve as the starting point for later investigations.
- The generation of near-single-cycle laser pulses necessitates technological improvements that are the subject of *Chapter 3*. We will show a laser system that is composed of an oscillator, an amplifier and a pulse broadening stage, with dispersion controlling elements at various steps. We have developed a novel hybrid compressor that will also be presented. These results have been published in [21]. Moreover, the term carrier-envelope phase (CEP) shall be introduced in more detail, as well as the methods for its stabilization.
- The measurement of the CEP in a single shot was realized for the first time that opens up a new way of performing strong-field experiments via CEP-tagging of individual laser pulses. Detailed discussion of our device and a new method that we have developed for measuring the CEP unambiguously and with ultra-high precision form *Chapter 4*, which appeared in [35].
- In *Chapter 5* we are going to present two-color waveform-synthesis that was realized by superimposing our fundamental pulse of one-octave with its detuned second-harmonic. After an overview of research achievements by others and discussing the benefits of having an SH pulse, supported also by our simulations, we will show a

feasibility study. We will enlist the properties of the elements that are needed for our implementation, and eventually we will discuss HHG that was carried out by our unique driver laser (manuscript in preparation).

- In *Chapter 6* we will summarize our results and outline future prospects.

Chapter 2

Atoms in strong laser fields

2.1 Strong field phenomena

When atoms are exposed to high intensity laser fields, the response of matter will have a nonlinear nature: we enter the field of nonlinear optics. Atoms show different response based on the amount of influence (characterized by the intensity) and the exposure time (set by the wavelength) by the laser field. Therefore, it is customary to talk about various regimes of nonlinear optics. With laser field intensities below $10^{13} \text{ W cm}^{-2}$, assuming visible and near-infrared (NIR) wavelengths, the perturbative regime is dominant. It gives rise to phenomena that have served as building blocks in ultrafast optics, among many others second- and third-harmonic generation, self-phase modulation, self-focusing. To describe the interaction of laser light with atoms in this framework it suffices to resort to a perturbative treatment. According to this, during the description of the nonlinear response the external laser field can be considered to be only a weak perturbation to the atomic potential, and the electrons remain bound to the atom. However, when the laser field strength reaches higher values a significant distortion of the atomic Coulomb potential happens and perturbation theory has to be discarded. The intensity that is necessary to enter this so-called strong-field regime is $10^{14} - 10^{15} \text{ W cm}^{-2}$. As a result, $10^{14} \text{ W cm}^{-2}$ already corresponds to an electric field that is almost 10% of the field that is seen by the electron on the first Bohrian orbit. Since the atomic potential gets lowered, the truly quantum-mechanical phenomenon of optical-field ionization (tunneling through the classically-forbidden potential barrier) can occur, which constitutes the first step of all subsequently unfolding processes. This regime of operation when the electron is liberated from the atom leads to the emergence of high-harmonic generation (HHG), a way to coherently convert laser light to the extreme-ultraviolet (XUV) or even soft X-ray domains. A regime that can still be described on the grounds of perturbation theory (though requiring the introduction of higher-order terms) is that of multi-photon

ionization. To subdue the binding force the atom absorbs several photons, and a peak comes up at $N\hbar\omega - I_p$, where N is the minimum number of photons needed to match I_p , the ionization potential of the atom. When the photon number N is in excess of what is minimally necessary to ionize, a series of peaks will appear in the spectrum that are separated by one photon energy. This scenario is a characteristic of above-threshold ionization (ATI). Lastly, non-sequential double ionization (NSDI) is another strong-field phenomenon whereby doubly charged ions are created due to the high kinetic energy of the laser-accelerated electrons that return to the ion core to liberate more electrons.

As the laser intensity approaches 10^{18} W cm⁻², for the accurate description of the motion of electrons relativistic effects have to be taken into account. It is the realm of relativistic nonlinear optics. Few-cycle pulses that can reach such relativistic laser intensities are already available [39], and an area that opened up recently is that of laser-based electron acceleration [40, 41]. Our work as outlined in this thesis, however built on the perturbative regime (mostly chapters 3 and 5 are where we will use concepts from this field) to be able to carry out investigations in strong-field area (chapters 4 and 5).

2.2 The three-step model

It is a peculiarity in nonlinear phenomena that all the salient points of such highly nonlinear processes as HHG and ATI can be described by a theory based on classical considerations. The model was developed by Corkum and it is known as the 'three-step model' or 'simple man's model' [42]. Later his theory was further justified and extended by quantum-mechanical calculations [43], and these two serve as the ground for strong-field science. According to the three-step model the electron is not a bound particle, as has been wrongly assumed in earlier works. Instead, the electron gets ionized due to the strong electric field of the laser, leaves the atom and its motion will be steered by the electric field that set it free. The moment of ionization is closely connected with the field strength of the laser. In fact, the electron is lifted up into the continuum when the field becomes highest, that is when the Coulomb force exerted by the atom gets suppressed. After the ionization step, acceleration under the laser field will follow. About a quarter of an optical cycle will have to pass when the sign of the electric field reverses, and it will slow down the electron, eventually turning its path back towards the parent ion. In HHG the trajectory of the field-accelerated electron finally ends when it recombines with the atom close to the next zero-crossing of the electric field. The electron gains energy from the laser through efficient acceleration, and this energy plus the ionization potential of the atom will be transferred to the emitted photon upon recombination. This last step, emission of a high energy photon completes the picture of HHG. With some likelihood,

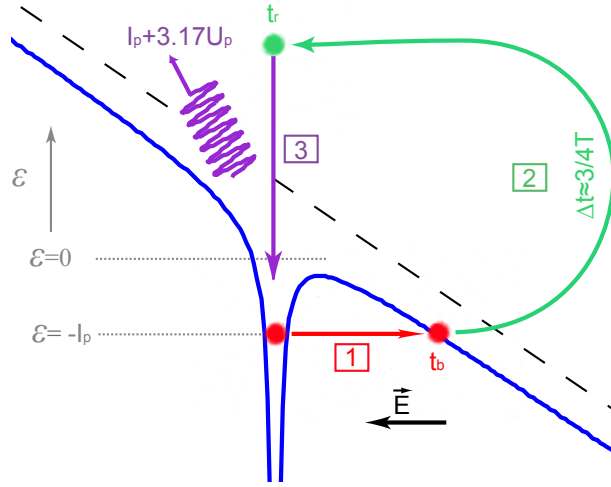


Figure 2.1: Illustration of the three-step model for HHG. Each step has been numbered: 1) liberation of the electron through tunnel-ionization, 2) acceleration of the free electron in the laser field, 3) recombination and emission of an energetic photon. t_b and t_r indicate birth and re-collision instances and Δt in the figure corresponds to the time spent by the electron that emits the highest energy photon (close to the cut-off region), its energy being $I_p + 3.17U_p$. ϵ stands for energy, the arrow showing the direction of change, while I_p is the ionization potential of the atom. The black long dashed line is the potential of the laser field, while the blue is the superposition of the atomic potential with that of the laser's. E denotes the laser electric field.

instead of recombining, during the ATI process the electron can also scatter from the atom and get further accelerated by the laser field. These three steps have been illustrated in Fig. 2.1 for HHG. Concerning the last step, the difference in ATI is that at t_r the electron scatters and turns back and then leaves the atom.

2.2.1 Ionization

The most common form of ionization happens when an atom absorbs a photon of energy $\hbar\omega$ and emits afterwards an electron with an energy in accordance with the photoelectric equation: $E_{kin} = \hbar\omega - I_p$. I_p is the ionization potential and E_{kin} is the kinetic energy of the electron. Alternatively, another way of ejecting an electron from the atom can be realized by distorting the atomic potential by a laser field: if the laser electric field becomes comparable in strength to the binding force experienced by the electron, the potential well of the atom can change so much that the electron can eventually escape from the atom. The effective potential felt by the electron can be written as:

$$V(\vec{r}, t) = -\frac{e^2}{4\pi\epsilon_0 r} + e\vec{E}(t) \cdot \vec{r}, \quad (2.1)$$

where the first term is the atomic potential, while the second describes the potential created by the laser field. We can see that due to the laser field that changes its sign every half-cycle, the potential well will also oscillate. A snapshot of one moment when their superposition allows the ionization of an electron can be seen in Fig. 2.1.

Depending on the laser parameters (peak electric field and its frequency) and the atomic species (its ionization potential) the potential barrier can be suppressed by different amounts. The work by Keldysh [44] quantified the difference between various levels of potential barrier suppression. To be able to differentiate between these regimes of operation, he introduced some important parameters. The Keldysh parameter γ and the ponderomotive potential U_p were defined to be:

$$\gamma = \sqrt{\frac{I_p}{2U_p}} \quad U_p = \frac{e^2 E^2}{4m_e \omega^2} \quad (2.2)$$

In the above, the parameter U_p emerges, which is the average kinetic energy of the electron during its wiggling motion under the laser electric field. e and m_e are the charge and mass of the electron, while ω and E are the angular frequency and the electric field of the laser. Using these parameters, we can now determine whether ionization occurs in the tunneling-regime, with $\gamma < 1$, or the multi-photon-regime, when $\gamma > 1$. In the latter case ionization takes place continuously, during multiple cycles of the laser field, that is even when the instantaneous electric field becomes zero. We enter this regime when the electric field changes so fast (i.e. its frequency being high) that there is no ample time for the electron to respond to the changes of the field. Here the quasi-static approximation of ionization breaks down. On the other hand this approximation, that is the assumption that the field is constant during the ionization time, remains valid when the tunneling-ionization or also called optical field ionization is the dominant mechanism. This can happen either by providing a low frequency laser field or by making sure that the laser field is strong enough. The tunneling time, that is the time for the electron to tunnel through the barrier, is a fraction of the period of the laser, so tunneling occurs almost instantly at certain phases of the field (an upper limit was determined recently, which gave 380 as [11]). Experimentally, typically a few times 10^{14} W cm⁻² is sufficient for tunnel-ionization (at 800 nm) in Ne. If a too high field strength is applied, the electron no longer has to tunnel through the barrier, which is allowed by quantum-mechanics, but the effective potential will be suppressed so much that it can just leave the atom without seeing any potential barrier. This is called the barrier-suppression, which for Ne necessitates an electric field intensity of $\approx 10^{15}$ W cm⁻².

Tunnel-ionization plays a major role in HHG. As we have seen, the three-step model involves different stages that evolve during certain phases of the laser field. All three stages

are linked together to allow HHG to occur. In the tunneling-regime the ionization depends sensitively on the actual value of the field. It means that ionization which determines the HHG yield will efficiently take place whenever the field is high. Incidentally, maximum HHG energy will result for the birth time of the electron close to the peak of the electric field, where the ionization will be pronounced, too. We thus see that the tunneling regime of ionization favors greatly the production of high-harmonic radiation.

Ionization is dependent on the electric field in a nonlinear manner. Adiabatic or quasi-static ionization rates (for $\gamma < 1$) rely on the assumption that the total potential that the electron is subject to is the sum of the Coulomb field of the atom and the instantaneous value of the electric field as we have discussed above. The ionization rate (i.e. ionization probability per unit time) $W(t)$ and the total ionization yield $\Sigma(t)$ can be expressed as:

$$W(t) = Ge^{-\frac{2(2I_p)^{3/2}}{3E(t)}} \quad \Sigma(t) = 1 - e^{-\int_{-\infty}^t W(t')dt'} \quad (2.3)$$

Ionization rates that are based on the quasi-static scenario have been derived by Keldysh [44] and Ammosov, Delone and Krainov (ADK) [45]. In equation 2.3, for $W(t)$ the ADK formula has been shown. The rate by Keldysh does not take into account the kind of atom that is involved in the ionization process, while that of ADK considers various species and thus it can be used more ubiquitously. Both descriptions of ionization, however share a common feature, which is that they have an exponential dependence on the electric field. The parameters of the atom (its quantum numbers) for the ADK rate show up in the factor G standing before the exponential dependence (the explicit dependence on the quantum numbers not shown here).

The second equation for Σ , for the total ionization yield allows us to assess how much ionization during the evolution of the laser field occurs. We will see it in section 2.4.2 that it has huge repercussions when it comes to generating high-harmonics with a multi-cycle pulse or with a few-cycle pulse. The situation will favor the usage of very short pulses both from a single-atom response view and regarding macroscopic effects.

Experimentally, it is common to work in a regime somewhere between the tunneling- and multi-photon cases, when $\gamma \sim 1$. However, even here it is widely accepted that the quasi-static rates can be used.

2.2.2 Acceleration

After an electron is liberated from the atom through the laser-field-induced suppression of the atom's potential barrier, its motion will be governed by the slowly-varying laser electric field. Within a small amount of time, it will no longer feel the pull of the atom. This is exactly the force, the Coulomb attraction which is neglected in the strong-field

approximation (SFA). The electron after its ionization at x_b and time instance t_b is sent onto a trajectory by the laser field, and due to the classical treatment its motion can be described by using Newtonian equations. If we use atomic (Hartree) system of units ($m_e=e=\hbar=1$), the acceleration under the influence of the field can be written as:

$$\ddot{x}(t) = -E(t) \quad (2.4)$$

Moreover, the semi-classical model assumes that the velocity of the electron at the birth time is zero, so $\dot{x}(t_b) = 0$. If the vector potential of the laser field is $A(t) = -\int_{\infty}^t E(t')dt'$ then the instantaneous velocity that the electron will reach can be written as:

$$\dot{x}(t) = A(t) - A(t_b) \quad (2.5)$$

Let us assume that our laser light is monochromatic with an angular frequency ω_0 and amplitude E_p , so its evolution can be written as $E(t) = E_p \cos(\omega_0 t)$. The velocity of the electron can simply be calculated as:

$$\dot{x}(t) = \frac{E_p}{\omega_0} [\sin(\omega_0 t_b) - \sin(\omega_0 t)] \quad (2.6)$$

The final velocity or drift velocity of the electron (at $t \rightarrow \infty$) can be obtained from an equation similar to 2.6, but now assuming that the pulse has some temporal shape ($E_p(t)$). We have to rely on the slowly-varying envelope approximation to arrive at the following expression for it:

$$-A(t_b) = E_p(t_b)/\omega_0 \sin(\omega_0 t_b) \quad (2.7)$$

From equation 2.7 and using the formula $-1/2A(t_b)^2$ the maximum kinetic energy of these "direct" electrons will be $E_p^2/2\omega_0^2 = 2U_p$, where U_p is the so-called ponderomotive potential. In ATI these "direct" electrons (which never return to the atom) are abundantly present (as opposed to re-scattered electrons), and their spectral intensity decreases as a function of ATI harmonic order (defined as $k\omega$, with k being an integer number, ω being the laser frequency). We can immediately see the existence of the cut-off at $2U_p$ and the monotonous decrease from the comparison of the form for the vector potential (which determines the drift velocity) with that of the laser light above [46]. Specifically maximum ionization occurs at the peak of the electric field, where the final velocity will be zero, while at the zero-crossing of the field a low number of electrons (ionization being zero here) will reach maximum drift velocity. If we integrate equation 2.5 the electron

trajectory will result:

$$x(t) = x(t_b) + \int_{t_b}^t A(t')dt' - A(t_b)(t - t_b) \quad (2.8)$$

or alternatively, we can integrate equation 2.6 to get the electron trajectory under the influence of a monochromatic light:

$$x(t) = x(t_b) + \frac{E_p}{\omega_0^2} [\cos(\omega_0 t) - \cos(\omega_0 t_b)] + \frac{E_p}{\omega_0} \sin(\omega_0 t_b)(t - t_b) \quad (2.9)$$

The amplitude of this oscillatory motion is referred to as ponderomotive radius a_0 or "quiver" amplitude, which is E_p/ω_0^2 . For a typical laser intensity of 10^{14} W cm⁻² it is on the order of a few nanometers, which is a larger value than the atomic radius, and thus it justifies the treatment of the electron as a free particle. For HHG, the electron has to return to the ion core to set free a high energy photon. The condition for this to happen is that at the re-collision time t_r the location of the electron should be again the starting position at birth time, $x(t_r) = x(t_b)$, which we can set to zero. Along this line we can get to the equation, which needs to be solved when we want to look for the birth and re-collision times of the electron. In turn, it will allow us to know the associated kinetic energy of an electron following a particular trajectory. From equation 2.8 and the condition for the location of the electron at t_r the equation to solve is:

$$A(t_b)(t_r - t_b) = \int_{t_b}^{t_r} A(t')dt' \quad (2.10)$$

or again, for our light-wave:

$$\frac{E_p}{\omega_0} \sin(\omega_0 t_b)(t_r - t_b) = \frac{E_p}{\omega_0^2} [\cos(\omega_0 t) - \cos(\omega_0 t_b)] \quad (2.11)$$

We will show in section 2.4.2 that it is possible to solve the above equation numerically, even for a non-monochromatic light, so for a laser pulse and obtain different trajectories for the electrons that eventually re-collide with the atom. For both ATI and HHG, there exists two types of trajectories, one that is characterized by a short excursion time called short-trajectory, and another kind that has a long travel time, which was given the name long-trajectory. In Fig. 2.3 on page 25 these trajectories have been indicated with arrows, connecting the pair of birth (t_b) and re-collision times (t_r), their separation distance defining the type of trajectory. Interestingly, different behavior can be ascribed to the electrons that follow either of these trajectories. In a HHG experiment it is necessary to get rid of the contribution of one of them (the long-trajectory) to obtain an isolated

attosecond pulse. We will see that the dipole-phase associated with them will show different dependencies on the intensity, in particular there is a large dependence for the long-trajectories, while it is smaller for the short-trajectories. Thus, the spatial intensity variation due to a real laser pulse will wash out the long-trajectory contributions. Another way to eliminate them is via a careful selection of the HHG gas jet position with respect to the laser focus. If the laser is focused before the jet, phase-matching will favor mainly the short-trajectories, and the long ones will not survive [47].

An effect that we have to mention here is that during the electron's travel in the laser field, according to the laws of quantum-mechanics, the electron wavepacket will expand laterally, that is dispersion of the wavepacket will occur. This will decrease the probability of recombination with the parent ion, which greatly affects the HHG efficiency. To attribute a number to it, upon re-collision the lateral spread is typically $\approx 5 - 10 \text{ \AA}$ [6].

It is possible to exert control over the trajectories in this step in various ways. One such method, as was pointed out in theory [48] in 1994, is the manipulation of the polarization state of the pulse on a time-scale equivalent to the oscillation period of the light pulse. By permitting the polarization state to be linear during one cycle and circular outside this region (called gate-window) we can switch off the contribution of other half-cycles to the HHG process. A single re-collision event will lead to an isolated attosecond pulse. The reason for this selection capability comes from the strong dependence of the HHG efficiency on the ellipticity of light field [49], that is only the linear polarization will allow the electrons to return to the atom. Manipulation of the waveform is also possible via another technique, which builds on using the second-harmonic field to change the original shape of the field. This will be discussed in detail in chapter 5 of this thesis, as well as mentioning similar experiments done for ATI.

2.2.3 Recombination or re-scattering

It is possible to solve the above trajectory equation 2.11 numerically (or graphically, which is possible for a continuous wave) and it turns out that it allows one to determine the return (or re-collision) times for the possible birth times. Recombination with the parent ion that emits an XUV photon in case of HHG, and the re-scattering event in ATI that produces high-energy electrons will be discussed in more details in the following respective sections.

2.3 Above-threshold ionization (ATI)

ATI has been known for a long time; actually it was discovered a few years before HHG in 1979 by Agostini [50]. It is based on a multi-photon process, when atoms absorb many

photons to overcome the ionization potential. For ATI even more photons are involved than what is absolutely necessary to ionize, which is therefore above the threshold, as the name implies. In the measured photoelectron spectra this process leaves its fingerprint via the creation of a peak structure, the spikes being at multiples of the fundamental energy of the laser ($n\omega$ in atomic units, n being an integer). They come up at every integer values, unlike for HHG where only odd harmonics exist, because ATI has a directionality in the sense that every half-cycle the electrons are created, and then go either to the left or the right directions (perpendicular to the laser beam propagation and parallel to the laser polarization). In one detector (either left or right) we thus measure electrons every full-cycle, which leads to the peaks at integer multiples of the laser energy. Typical theoretical ATI spectra corresponding to two different waveforms, which spectra can be measured by two detectors (usually a micro-channel plate or MCP) can be seen in Fig. 2.2. They were provided by G. G. Paulus (Friedrich-Schiller-Universität, Jena), and they are the result of numerical calculations that were done by solving the 1 dimensional time-dependent Schrödinger equation. Indicated by arrows with the labels $2U_p$ and $10U_p$ we can observe two cut-offs, one that is lower in energy and another one that is higher. All these important features can be understood from the three-step model [46], the existence of the lower lying cut-off requiring only the first two steps. Below the first cut-off we have "direct" electrons that are generated by the laser field and then sent onto a trajectory that has no corresponding return times to the atom. The decreasing nature of the intensity as a function of energy in this region and the position of the first cut-off being at $2U_p$ were explained above in section 2.2.2 of this chapter.

The first observation of the spectrum above the $2U_p$ cut-off can be attributed to G. G. Paulus in 1994 [51]. It was found that similarly to HHG a flat spectral part follows the first cut-off, and this plateau-like feature ends with a steep second cut-off. Based on the three-step model, it can be argued that this plateau is created by electrons that revisit the atom, elastically back-scatter and then are re-accelerated by the laser field to even higher energies than before. The instantaneous velocity of the electron can be written as in equation 2.5, where $-A(t_b)$ represents a constant as determined by the initial conditions. Applying the condition that the velocity will change sign upon return to the atom, the drift energy (average kinetic energy) of the electron after the re-scattering event can be expressed as:

$$W_{drift} = \frac{[2A(t_r) - A(t_b)]^2}{2} \quad (2.12)$$

This equation is similar to the instantaneous kinetic energy of the electron that returns and then recombines with the ground-state atom in HHG (see equation 2.14), except here there is a factor '2' before the vector-potential evaluated at the return time, and it is coming from the condition above regarding the change of velocity. From numerical

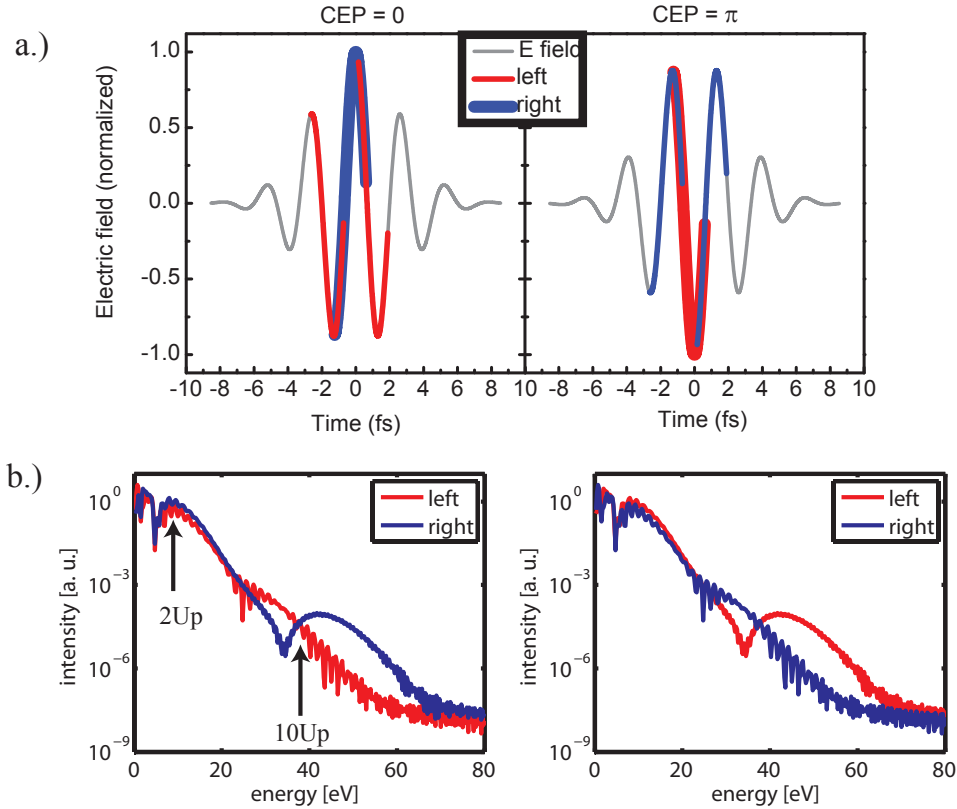


Figure 2.2: a.) Travel times of rescattered electrons (red and blue lines) in the ATI process during the presence of the electric field of a 1.5 cycle (4.1 fs) cosine (CEP=0) and anti-cosine (CEP=π) laser pulse (grey lines). Red and blue means final arrival to the left or the right MCP, respectively. Obtaining the trajectories entailed classical calculations. b.) Time-of-flight (TOF) spectra obtained by theory for two different CEP settings, for CEP=0 (left fig) and CEP=π (right fig). They show a close resemblance to the experimentally measured TOF data, which are plotted in Fig. 4.7 on page 59.

evaluation of the trajectory equation (equation 2.8) a similar (but not the same) birth and return times can be obtained as for HHG for the electrons that will give a maximum drift energy. The value of this maximum, however, will be much higher than before, as instead of 3.17 we have a factor of 10.007, so the energy will be $10.007U_p$ [46]. As already conspicuous in Fig. 2.2, this high-energy part is an important one, as its position shows a sensitivity to the waveform. This behavior will be discussed next.

2.3.1 Phase sensitivity of re-scattered ATI spectra

Strong-field processes, including ATI, depend sensitively on the exact time-evolution of a pulse, on the value of the electrical field. The alignment of the fast-oscillating carrier-wave under the envelope gains importance as the pulse duration shortens. Therefore, it necessitates the introduction of a property of a short pulse, which is its carrier-envelope

phase (CEP). The CEP is defined through the equation that describes the change of the electrical field of a pulse, $E(t) = g(t)\cos(\omega_0 t + \phi_0)$, where $g(t)$ is the envelope function and ϕ_0 is the offset of the the highest peak of the carrier-wave from the maximum of the pulse envelope. It is a dynamically changing quantity in few-cycle laser systems, and the reasons of its fluctuating nature, as well as its stabilization will be discussed in more detail in chapter 3. Examples of some waveforms that result from different CEP values have been plotted in Fig. 2.2 and Fig. 2.3 on page 25.

It was already anticipated [52, 53] before the first successful demonstration of phase-sensitivity in ATI [34] that re-scattered electrons for few-cycle pulses could provide us a highly efficient way to measure the actual value of the CEP [36] and not only its rate of change [25, 26]. As we have shown above ATI process occurs every half-cycle of the laser, which gives photoelectrons a directivity, i.e. due to the sign reversal of the laser field they will be emitted in two opposing directions (left and right) parallel to the laser polarization (for p-polarization, otherwise for s-polarization the emissions will be up and down). For a few-cycle cosine pulse (Fig. 2.2) there are dramatic differences in the heights of the electric field extrema in consecutive half-cycles and it will cause a main emission in one of the directions, left or right. The rescattered electrons can acquire high energies due to their relatively long excursion time of three quarters of an optical cycle that occurs after their ionization time at t_b and before their rescattering time of t_r . Importantly, the plateau region that they create shows a high sensitivity to the CEP [51], and the dependence is about an order of magnitude higher than for "direct" electrons [54, 55]. A qualitative manifestation of this disparate dependencies is also reflected in the simulations in Fig. 2.2. For the the low-energy "direct" electrons, asymmetric ionization yields at instant t_b are largely canceled by the deflection of the photoelectrons in the laser field [56]. However, the conditions for rescattered electrons to be efficiently accelerated by the field are strict. Not only a large enough field has to be present at the time of their ionization at t_b to get a significant electron yield, but also following the backscattering event at t_r the electric strength has to be significant to give them high kinetic energies. Because t_b and t_r are separated in time by approximately three quarters of an optical cycle, the above two conditions are difficult to be fulfilled. As a result, strong CEP dependence can be observed for the plateau region.

In HHG there is a CEP dependence, as well. However, because of the inversion-symmetry of the process there is no difference when measuring HHG spectra between left or right emissions for cosine and anti-cosine pulses, so the spectra will be identical when the electron recombines from the left or right directions. It makes the ATI process more favorable for CEP measurements because there is no such π phase-ambiguity. The lack of phase-ambiguity, unfortunately is only partial. We will see in chapter 4 that with the

conventional representation (phase-asymmetry parameter vs. CEP) we still have phase-ambiguity. Chapter 4 addresses this issue, where we will present a new method that eliminates this ambiguity.

2.3.2 Macroscopic effects - volume effects

Experimentally we always irradiate a large number of atoms to get a measurable signal. In ATI, unlike in HHG, the wavepackets of the electrons have a small spatial extent, and in addition typically a very low gas pressure is used (in the range of 10^{-2} mbar, while in HHG it is usually above 100 mbar). Both of these conditions will lead to the fact that the electrons' wavepacket will be below the mean inter-atomic distance and no interference will occur between them. Thus ATI can be treated as a single-atom phenomenon: coherent interaction that is prevalent in HHG, which is manifested in phase-matching is not present here. It helps greatly in the interpretation of results through simulations as opposed to the case when one has to deal with phase-matching in HHG, which is a complex issue that is influenced by numerous parameters.

The previous explanation does not obviate the need to take into account the macroscopic effects. Electrons from individual atoms will arrive at the the detector and because our laser pulse varies both spatially and temporally, there will be an averaging effect concerning the positions of the cut-offs due to their strong dependency on the electric field strength. The results of advanced calculations (3D), together with comparing these with experimental findings will be discussed in chapter 4.

2.4 High-harmonic generation (HHG)

High-harmonic generation (HHG) is the phenomenon of converting laser light at a given frequency to integer multiples of it through a highly nonlinear and non-perturbative process. The first experiments were conducted by McPherson [57], followed by Ferray [58] in the 1980s. It was found in their work that the harmonic conversion drops suddenly for low energies (perturbative regime) and then remains constant over an extended number of harmonic orders, which spectral region was given the name plateau. Conversion does not stay flat towards high energies, but the measured spectrum ends abruptly at a certain energy called the cut-off. Perturbation theory failed to explain this observation, because it predicted an exponentially decreasing harmonic intensity as a function of the harmonic order. It suggested that another mechanism is responsible for this feature. Quasi-classical theory (three-step model) could finally give a successful explanation to the behavior of the plateau harmonics. The model basically entails that in every half-cycle of the field a HHG photon is generated. The consequence of such a periodically occurring event is that in

the frequency domain the spectrum will contain only odd harmonics of the fundamental, which means that the spacing between the harmonic lines will be $1/(T/2)=2/T$, T being the period of the fundamental field (2.6 fs for 780 nm).

The last step of the three-step model for HHG is the recombination of the electron with the parent ion, which will emit a photon of a shorter wavelength than that of the laser's. Quantum mechanically speaking, emission results from the interference of the continuum wavepacket with the part of the wave function that was left behind in the ground state. The photon will have a shorter wavelength, that is a higher energy, because it will carry away the recombining electron's kinetic energy plus the energy associated with the ionization potential of the atom. The energy of the photon generated through HHG can be simply expressed as:

$$\omega_{HHG} = W_{kin} + I_p \quad (2.13)$$

where I_p is the ionization potential of the specific gas that is irradiated by the laser light and W_{kin} is the kinetic energy of the accelerated electron. In general, with the help of the vector-potential of the field the final kinetic energy will be:

$$W_{kin} = \dot{x}(t_r)^2/2 = \frac{[A(t_r) - A(t_b)]^2}{2} \quad (2.14)$$

Not all the trajectories will lead to an emission of a photon. In equation 2.6 the first term is the drift velocity of the electron. If in the phase dependence we include the CEP, then the drift velocity becomes positive at a phase of $\omega_0 t_b + \phi_0 = 0$, and trajectories that are initiated later than this time will return to the ion. To every birth time there is a certain kinetic energy. By solving equation 2.11 numerically one finds that maximum energy can be attributed to a launching phase of $\approx 18^\circ$, so this time-instance is ≈ 0.05 optical cycle away from the electric field peak. High-harmonic radiation above this energy vanishes, therefore this energy is called the cut-off, which has been determined to be [42]:

$$\omega_{HHG,cutoff} = I_p + 3.17U_p \quad (2.15)$$

To obtain the cut-off energy, the peak electric field of the half-cycle that accelerates the electron has to be considered. This particular one according to the above outlined steps will come half a period later than when the electron is ejected into the continuum.

There are some interesting developments that aim at pushing out the location of the cut-off. One spectacular demonstration of such possibilities was achieved by using few-cycle light pulses with an energy higher by a factor of 2 than what is normally available from a few-cycle Ti:Sa (at 800 nm) laser. The cut-off in their experiment was in the

keV range [59]. This achievement was made possible due to an increased fundamental laser energy, and the exposure of the atoms to higher field strengths by relying on a few-cycle pulse (see section 2.4.2). An alternative future direction to reaching keV photons seems realizable by manipulating not the intensity, as in [59], but the wavelength of the driving laser [60]. By looking at the cut-off law it is obvious that a dramatic shift of the cut-off position can result due to its quadratic dependence on the wavelength [61]. However, it has to be noted that the harmonic yield depends on the wavelength, too, and unfortunately on a single-atom response level it decreases according to $\approx 1/\lambda^5$ [62]. On the other hand phase-matching on a macroscopic level promises to help us overcome such limitations regarding the yield [63].

2.4.1 Macroscopic effects - phase matching

Generation of high-harmonic photons experimentally is achieved not from one, but from an ensemble of gas atoms. Consequently, apart from the single-atom response, which is influenced through all stages of the three-step model, the collective response of matter has to be considered. The electromagnetic wave in the form of XUV light that is radiated by the tiny dipole antennas that the atoms represent can add up in phase or out-of phase. Phase-matching describes this phenomenon: it tells us what contributions exist to the total phase and whether efficient build-up of the coherent light is possible. Physically, what causes an imperfect phase-matching is the nonequal propagation speeds of the laser light and the generated harmonic radiation. Assuming a collinear interaction, for the generation of the q th harmonic the phase-mismatch can be written quite generally as:

$$\Delta k_q = qk(\omega_L) - k(q\omega_L) \quad (2.16)$$

In equation 2.16 ω_L denotes the laser frequency and k the wavenumber. There are a number of reasons why the above expression cannot become zero. This equation can be rewritten for our case, at the same time indicating the physical contributions:

$$\Delta k_q = \Delta k_{disp} + \Delta k_{plasma} + \Delta k_{foc} \quad (2.17)$$

A brief summary of the individual effects that hinder us in achieving perfect phase-matching will follow.

- *Normal dispersion.* Every medium exhibits a dispersion due to the resonances in them, which manifests itself in the frequency dependence of the refractive index, $n(\omega)$. This mismatch is $\Delta k_{disp} = [n(\omega_L) - n(q\omega_L)]q\omega_L/c$. In the XUV spectral region $n(\omega)$ assumes a negative value, while in the visible and near-infrared it is

positive, and as a result $\Delta k_{disp} > 0$ holds.

- *Plasma dispersion.* Ionization is the first step of the HHG process. During the second stage, when the electrons get accelerated, only a small portion will follow such trajectory that will end by the emission of a photon; most of them do not re-collide with the atom, but form a free-electron cloud. As with normal dispersion, here owing to the plasma resonance, plasma dispersion exists. The contribution of this mismatch is: $\Delta k_{plasma} = \omega_p^2(1 - q^2)/(2qc\omega_L)$, where ω_p is the plasma resonance frequency. Obviously, this term has a negative value.
- *Focusing geometry.* This term would be zero, if our laser beam was a plane-wave. We have to reach sufficient peak intensities for the ionization to occur and this is done by a combination of temporal and spatial effects. The former is essentially realized by the usage of a short pulse, while it is the latter effect, which we have to consider here that will cause a phase-mismatch. Another effect that falls into the more general 'geometry' category is that of the application of a waveguide, where a propagating waveguide mode can ensure a negative geometrical phase-mismatch term [64]. We consider now only the focusing geometry in the form of a beam that is incident on a reflective focusing mirror, which we apply in our experiments. Near the focus the Gouy-phase will play a major role. It means that after and before the focus the phase will be flipped by π . This term will be $\Delta k_{foc} = (q - 1)/z_R$, where z_R is the Rayleigh-range (its value being positive).

The coherence length L_c can be calculated from the above phase-mismatch. It is the length where the phase-mismatch becomes π , which is the distance where constructive interference will end ($L_c = \pi/\Delta k_q$). Additional macroscopic effects that need to be accounted for are:

- *Absorption.* Reabsorption of the XUV photons by the medium occurs, because a lot of media have their outermost electrons attached to the atom with such a binding energy that this value is matched by the energy of the HHG photons. It means that these gases have high photoionization cross-sections ρ . The absorption length, the point where the intensity lowers by $1/e$ is $L_{abs} = \zeta\rho$, where ζ is the density of atoms.
- *Intensity-dependence of the atomic dipole phase.* Strictly speaking the dependence of the dipole-phase on the intensity is a single-atom property. However, we have to consider it here, because it affects phase-matching. In the semi-classical formulation of the three-step model the dipole phase gives the phase of the electron that it acquires during its time spent in the continuum [43]. Interestingly, this phase for the short-trajectories is almost flat with a change of the intensity, while for the

long-trajectories there is a linear dependence. Following propagation the latter will give a fast varying phase with a small off-axis area where good phase-matching dominates (before the laser focus), while the former provides good phase-matching in a wider region on-axis (after the focus). Hence, with the focusing geometry it is possible to select one of them, which is critically important for isolated attosecond pulse generation.

In an experiment there are a few knobs that one can adjust to arrive at an optimal phase-matching. The density of the gas can be varied, which will change the absorption of XUV. The plasma dispersion can be altered by turning up the laser intensity and changing the pulse duration. The distance of the laser focus from the jet will also cause the phase-matching conditions to change.

We will examine more in detail in section 2.4.2 how the pulse duration will affect the phase-mismatch through the plasma dispersion, and we will discuss furthermore its far-reaching consequences.

2.4.2 Isolated attosecond pulse generation

The three steps of the HHG process repeat during every half-cycle of a lightwave, which in the time domain gives an attosecond pulse train (APT), whereas in the spectral domain harmonic lines will appear [65, 66]. If each half-cycle looks identical to the others, i.e. when one deals with a long pulse, this APT will be made up of attosecond pulses with the same characteristics (except for a π phase-shift between consecutive pulses). Clearly, for the isolation of a single attosecond pulse the time-evolution of the long pulse has to be broken on a cycle-scale. The most successfully used technique for achieving this condition is that of the application of a few-cycle pulse [16, 67]. For a multi-cycle pulse each recollision event will give a HHG photon energy that is nearly the same for half-cycles close to the peak of the pulse. Conversely, a few-cycle pulse introduces both energy and intensity variation of the XUV photons. During a short pulse substantial field variation exists. As a result, the highest energy of the XUV bursts in consecutive half-cycles will be altered, the most energetic burst being the result of the most intense electrical field value. If we have at most one such burst which stands out among the others in energy, we can select its highest energy portion by a high-pass filter, and thus only one attosecond pulse will remain. In the frequency domain now, unlike earlier for long pulses, such a single pulse close to the cut-off region corresponds to an unmodulated spectrum, a continuum [27]. Along this line of reasoning, it is also obvious that the spectral extent, the bandwidth of this continuum is set by the highest energy burst and the next one closest to it in energy. Fourier-transformation that creates a connection between time and frequency space tells us that the broader this bandwidth is, the shorter the pulse duration will be. It stresses

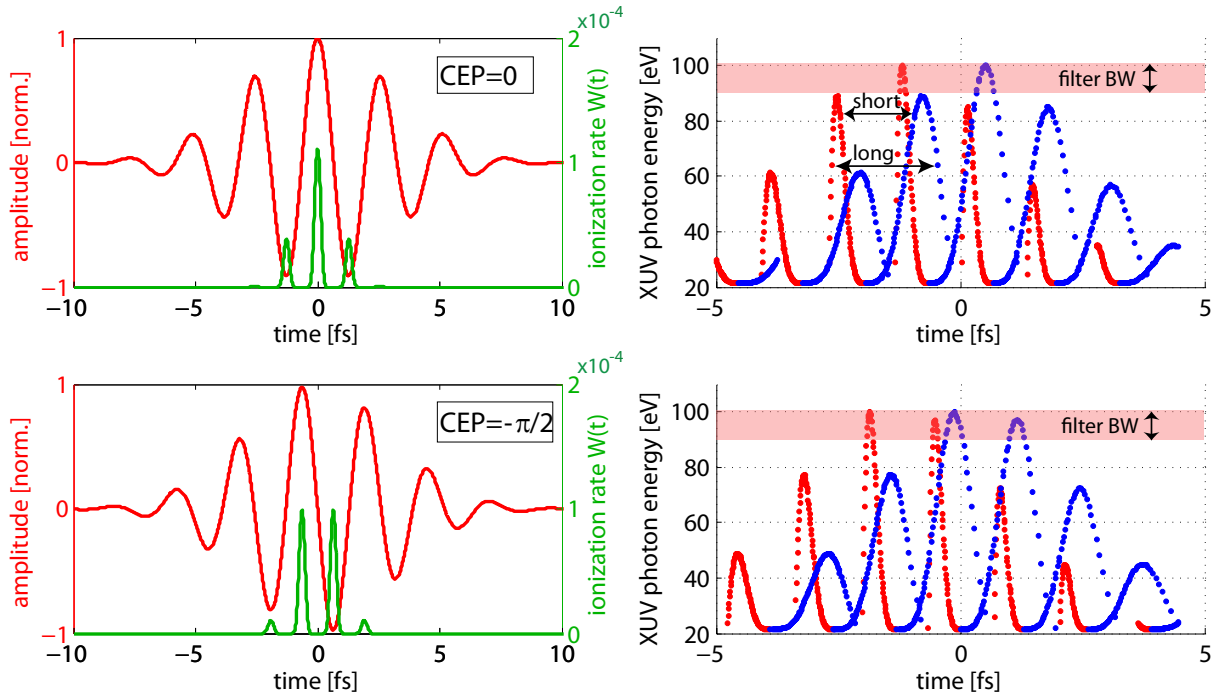


Figure 2.3: Two characteristic waveforms and the XUV bursts corresponding to them. Classical trajectory calculations were performed for the cosine-pulse (upper plots) and the anti-sine-pulse (lower plots) assuming a 5 fs fundamental pulse with a peak intensity of $4.4 \times 10^{14} \text{ W cm}^{-2}$ and Ne as the gaseous medium. Blue dots indicate energy as a function of birth time, red stands for energy vs re-collision times. The short- and long-trajectories that electrons can follow have been shown, too. From the upper right plot it becomes apparent that among the two depicted CEP settings only the cosine pulse creates one XUV burst that stands out in energy among the others. Filtering out these harmonics for the cosine case in the energy range shown by the pink transparent rectangle permits the generation of a single attosecond pulse.

thus the importance of broadening the width of the continuum. If a truly few-cycle or a near single-cycle pulse is available, we can ensure that some continuum or in the latter case a very broad unmodulated spectral bandwidth exists.

Because the HHG process depends critically on the electrical field and not only on the cycle-averaged intensity of the pulse, we can expect that the CEP of a pulse will play a major role. To show waveforms corresponding to two CEP settings for a two-cycle pulse (at 800 nm), in Fig. 2.3 we plotted two markedly different cases, which have a CEP of 0 and $\pi/2$, respectively. The CEP setting with 0 phase gives a pulse, which became known as cosine-pulse (CEP= π being anti-cosine), while the name of a pulse corresponding to CEP= $\pi/2$ turned out to become a sine-pulse (for CEP= $-\pi$ the name is anti-sine pulse). These names apparently stem from the resemblance of the waveforms to cosine and sine waves with $t=0$ being the maximum of the envelope. Assuming these two types of pulses we carried out numerical calculations by solving the classical equation of

motion (equation 2.10) to illustrate their effect on the final outcome of HHG. Accordingly, the right plots depict the energies of XUV bursts as a function of birth (blue dots) and re-collision times (red dots). The ionization rates from the ADK-model have been calculated (equation 2.3), too, which appear as peaks at the crests of the wave, where the electric field reaches extrema. From the plots we can determine the width of the continuum for the cosine-pulse (indicated by the label 'filter BW'), which according to the above discussions amounts to a bandwidth of about 10 eV. In fact, two-cycle laser pulses, that is pulses with a duration of 5 fs (at 800 nm) were the shortest available ones for HHG for many years [16, 68, 69]. Doing energy filtering in this 10 eV bandwidth provided a single attosecond pulse, which experimentally entailed a duration of 250 as [7]. Here, we tacitly assumed that the contribution from the long-trajectories have been canceled, which can be achieved by a proper focusing geometry (placing the focus before the position of the HHG jet). From observing the lower plots (anti-sine pulse) the scenario of single attosecond pulse generation changes distinctly. Now this particular pulse creates two XUV bursts with nearly the same energies. Their energies fall exactly into our filter bandwidth and as a result, two XUV pulses are kept after our filtering. Such extreme difference between the outcomes of experiments can be circumvented by using phase-stabilization, which is to be further elaborated on in chapter 3.

Interestingly, there is another significant benefit of having a short pulse as opposed to a long one [70]. Another parameter of a pulse is its intensity. Evidenced by equation 2.3 the pulse duration of the driver laser influences the value of the ionization yield. For a long and weak pulse (with relatively low peak intensity) high ionization yield can happen already after a few cycles of the laser field. In essence, the gaseous medium can get fully ionized even before the maximum field can be reached. For few-cycle pulses the situation is quite different. The main advantage when using them comes from the fact that the atoms can survive to higher laser intensities prior to ionization. The accelerating electrons can be exposed this way to a stronger, rapidly increasing laser field, which in the end means that more energy will be transferred to them. Re-collision with the parent ion will induce the emission of photons, and it explains why such high cut-off energies are observable in experiments with very short pulses (for an extreme case see [59]). The lower overall ionization yield will affect phase-matching, as well, and in a positive way. The free electron density can be minimized and a longer coherence length will result through the modification of the contribution from the plasma dispersion. This latter improvement will translate to a high XUV photon flux. The most recent exploitation of this phenomenon was realized during HHG with a near-single-cycle pulse [71].

We conducted experiments that aimed at shortening the pulse duration during HHG by making a broad continuum available. To this end, we focused our laser beam (5 fs,

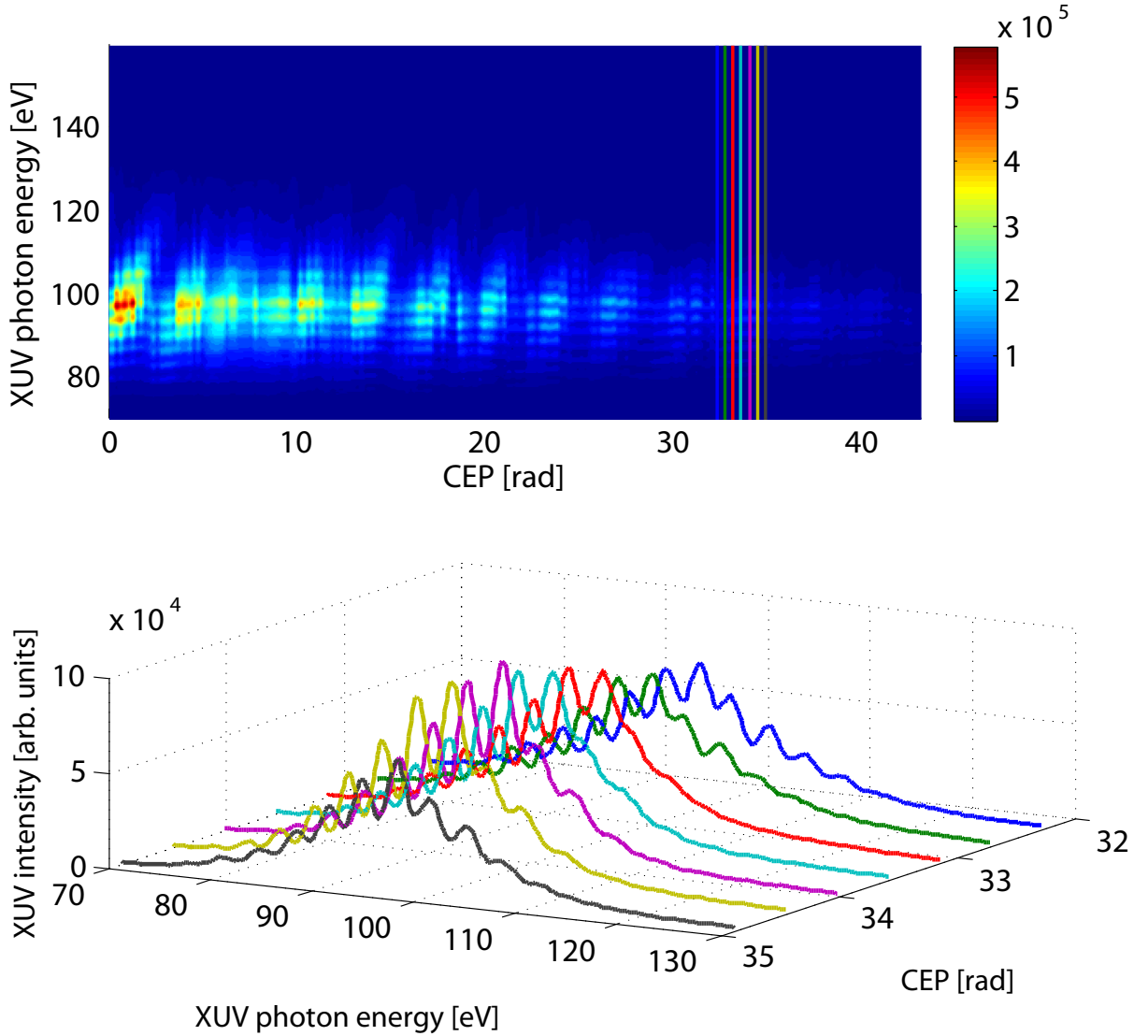


Figure 2.4: A long CEP scan showing HHG spectra with ~ 5 fs pulses. The low intensity harmonics (higher CEP values) were generated by a two-cycle pulse, and the higher intensity region in the scan shows a transition towards HHG with even shorter, near-single-cycle pulses. Thus, due to the long scan we slowly change the pulse duration, too. The 7 selected spectra below the false-color 2D plot all have CEP values that lie in an interval of $\sim \pi$ to show the switching between sine-shaped (modulated cut-off region) and cosine-shaped pulses (smooth cut-off part). The CEP values here are only relative values. However, from earlier work [27] we know that a modulated spectrum near the cut-off is indicative of a $\text{CEP}=\pi/2$ and an unmodulated spectral portion is a characteristic feature of a pulse with $\text{CEP}=0$. In the latter case a bandwidth of ≈ 10 eV exists, which permits the generation of an isolated attosecond pulse.

150 μJ) from a phase-stabilized Ti:Sa laser system (see chapter 3 for the description of the laser) with a focusing mirror ($f=500$ m) and generated high-harmonic radiation (with a gas pressure of 250 mbar). To be able to detect the XUV radiation we rejected

the more intense laser light by inserting Zr filters into the beam path (thickness of 650 nm when a grating was used afterwards). This filter's transmission characteristics, as well as some other filters we used in our experiments can be seen in Appendix A. Our high-harmonics were spectrally resolved after passage through the Zr filter by sending them onto a grazing-incidence grating (Hitachi) that angularly dispersed the different wavelengths. Our laser beam propagated through our setup that we used also later when we did HHG with a fundamental and its second-harmonic (chapter 5). In order to eliminate the second-harmonic for now, we simply turned the SHG crystal by 90° in a plane perpendicular to the laser beam's propagation direction so that the crystal's nonlinear coefficient was extinguished. Our beam still went through the half-wave plate, which gave a small bandwidth-reduction of our fundamental due to its imperfect rotation of all wavelength components by 90° . Results from our measurement for a wide CEP range (CEP scan) can be seen in Fig. 2.4. A more detailed description of the experimental setup will follow in chapter 5. The spectral measurements after HHG are summarized in Fig. 2.4. In the 2D plot the CEP was scanned (in steps of $\approx \pi/15$ by using a motorized pair of wedges) in a wide range, and below it a few representative cases have been selected, which show spectra for 7 different CEP settings (the step size being $\approx \pi/7$). The spectra corresponding to HHG with a cosine- and sine-shaped fundamental pulses have also been included. The bandwidth of the continuum in our measurements was approximately 10 eV. The CEP scan in a wide interval caused a slow change of the pulse duration, as well. The changing pulse duration is manifested in the broadening of the continuum and the higher observed XUV intensity, which will be presented in the next section.

2.4.3 Broadband HHG with a 1.5-cycle pulse

Assuming an appropriate compensation of the dispersion to reach a close to Fourier-transform-limited pulse length the shortest attosecond pulse duration is directly influenced by the bandwidth of the continuum. Specifically, there exists an inverse relationship between the pulse duration and the spectral bandwidth. During the unfolding of attosecond science numerous and various steps have been taken in the direction of generating progressively shorter attosecond pulses. One such method relies on the application of a few-cycle pulse, which allowed us to break the femtosecond barrier [22]. Another technique employs few-cycle pulses, as well, but with a changing polarization (circular-linear-circular in time) to cancel the contribution from half-cycles other than the main one [72] (see also the end of section 2.2.2). The measured pulse duration was as short as 130 as [73]. A third method creates a superposition of the fundamental and its second-harmonic. Spectral measurements in accordance with this latter technique will be extensively discussed in chapter 5 of this thesis.

In our experiment we were interested in reaching a near-single-cycle pulse duration for the generation of sub-100 as pulses. Our unique laser pulse source [21] was the same as the one that we also employed in the previous section. The spectral bandwidth supported compressibility to near-single-cycle duration, and this possibility was realized by using chirped-mirrors. As a matter of fact, our results that were presented in the previous section were the "by-products" of our optimizations towards further reducing the duration. Those measurements produced HHG spectra that supported a 10 eV bandwidth and through inference our laser pulse was approximately 5 fs long. A major difference resulted, however from exposing our atoms to a much shorter laser pulse duration. In Fig. 2.4 for low CEP values the indications of a transition towards a near-single-cycle fundamental pulse is already visible. In this region a broadening of the continuum and high XUV flux is present, which is due to the combination of an increased peak intensity and a shorter pulse duration. These improved laser properties eventually result in an enhanced phase-matching, thus higher XUV intensity; and additionally higher cut-off energies, broader continua. The CEP was further changed towards lower values, and again, because of the large range of variations the pulse duration was altered, too. The 2D plot on the top in Fig. 2.5 shows a CEP scan that is a continuation of the scan of Fig. 2.4 (now extending below CEP=0°). The lower plot of Fig. 2.5 is a result from theoretical calculations, which assumed a 3.3 fs pulse, a peak intensity of $6 \times 10^{14} \text{ W cm}^{-2}$ and a 10% variation of the intensity. The explanation on why we had to introduce such a 10% intensity fluctuation will be given later.

The regime of single-cycle nonlinear optics differs from the conventional HHG with two-cycle pulses from the point of view of the broadening effect the following way. First, an increase of the bandwidth of the continuum is coming from the rapidly varying very short waveform that creates a modification of the energies of XUV bursts in successive half-cycles by a magnitude which was not possible before. Second, we have a contribution from ionization gating to the broadening effect, which happens because the field strength variations on a sub-cycle time scale are so dramatic that we can almost completely switch off ionizations in some half-cycles. The intensity of the spectra created by the individual half-cycles of the laser pulse [74] can thus be different by even two orders of magnitude. This new condition during HHG means that for the best CEP setting of 70° we have only two half-cycles contributing to the total measured spectrum, and each with cut-off energies that are far apart from each other. The separation between these two cut-offs translates to a FWHM bandwidth of 30 eV, which allows the generation of an isolated 80 as pulse [71]. This ideal CEP setting, surprisingly enough, occurs for a value of 70°, which gives a near sine-shaped pulse, a waveform that for a 5 fs pulse creates two attosecond pulses. Another peculiarity is that actually most of the CEP settings for a 1.5-cycle pulse

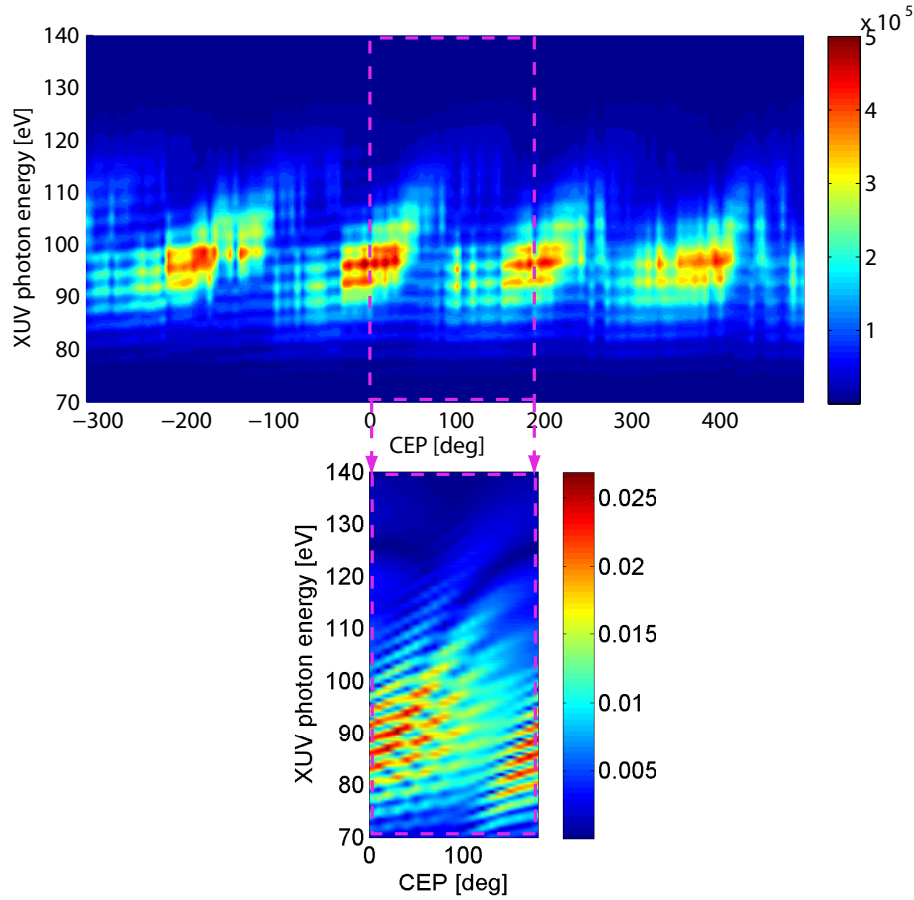


Figure 2.5: Comparison of experimental CEP scan with theoretical calculations for HHG with a 1.5-cycle pulse. The experimental spectra (upper plot) in the 2D false-color representation were obtained by changing the CEP in steps of $\approx 6^\circ = \pi/30$. The total interval covers a CEP range $> 4\pi$, and because the waveform shape has a π periodicity, the theoretical calculations (lower plot) were only performed for a π range. This comparison allowed us to calibrate our measurement (the x axis of the upper plot).

produce an isolated attosecond pulse, and the isolated attosecond pulse purity becomes the worst for $\text{CEP}=130^\circ$. The pulse purity or contrast here is defined as the ratio in intensity between the most intense attosecond pulse and the satellite pulses surrounding the main one.

In theoretical studies, unless one takes into account propagation effects that gets rid of the long-trajectories (see section 2.4.1), a slow modulation in the spectrum is observable, which is coming from the interference of short- and long-trajectories. Slow modulation results, because as we see it in Fig. 2.3, these two trajectories are inside a half-cycle sharing the same energy and with a time separation of ≈ 300 as. In the frequency domain due to the inverse relationship between time and frequency gives a long period of oscillation. Understandably, for a harmonic structure, the modulation in the spectrum is fast due to the separation of around 1.3 fs between the XUV bursts. In theoretical calculations

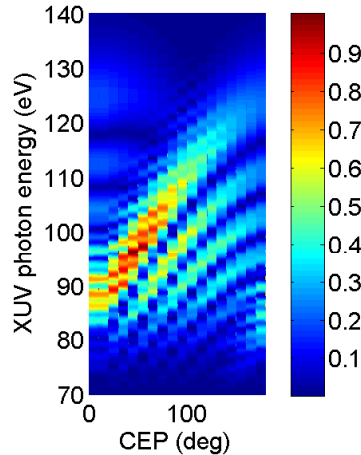


Figure 2.6: Theoretical CEP-scan with long-trajectories considered, unlike in Fig. 2.5, where their contribution was intentionally diminished. We can observe a slow modulation now that is a result of an interference between short- and long-trajectories inside one half-cycle.

when propagation effects, i.e. phase-matching is considered, and also in the experimental results long-trajectories are eliminated to a large extent (see section 2.2.2 and 2.4.1). Consequently, the fast modulation is not visible and we have an isolated attosecond pulse. In order to simulate the experimental conditions, in our theoretical calculations we intentionally introduced an artificial intensity variation for the fundamental that caused the long-trajectories to disappear, similarly to how it happens for a pulse with some spatial profile in an experiment. For the sake of completeness, we also include here the case when such intensity fluctuation was not introduced, so we keep the slow-modulation from the short- and long-trajectories. A corresponding simulation can be seen in Fig. 2.6.

We see that we have a good match between theory and experiment. By making a careful comparison, we are now able to assign to each spectrum in our 2D scan the correct CEP, unlike before in Fig. 2.4 that has relative CEP values along its x axis. We can furthermore draw a comparison between the results in [71] and ours, which show a fairly good match.

Furthermore, we selected spectra for 4 different CEPs, which are shown in Fig. 2.7. As we have seen above, a CEP value close to 70° would give the best contrast, the most pure isolated attosecond pulse. Out of the plots of Fig. 2.7 the spectra corresponding to the case with CEP= 90° is the closest one to this ideal setting. The plotted spectrum contains the lowest amount of modulation, whereas all the others show larger modulation depths, which is indicative of the pulse purity. Another notable spectrum is the one that has a CEP= 135° assigned to it. As can be readily seen, it has a double hump structure. It is an example for the configuration when two half-cycles contribute to the total spectrum, one that is located lower, and another that is higher in energy, while both

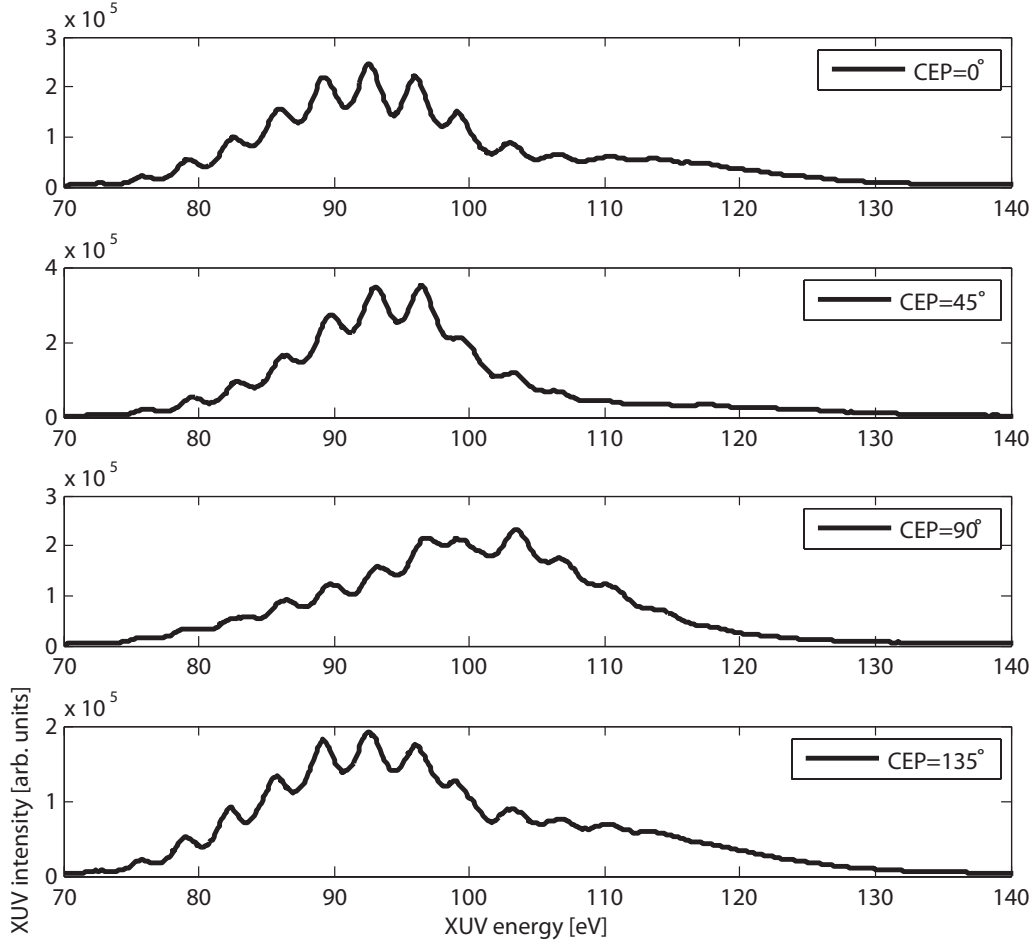


Figure 2.7: CEP dependence of HHG with 1.5-cycle pulses. Spectra corresponding to 4 CEP values are shown, which have been selected from the CEP scan of Fig. 2.5. By shifting the CEP we can tune our spectrum by approximately 10 eV. The sensitivity of isolated attosecond pulse generation to the CEP is relaxed for such near single-cycle pulses, and in accordance with [71] the purest pulse can be obtained with CEP=70°. The bandwidth of the continuum now has increased and it allows the generation of a sub-100 as pulse (with a filter with FWHM width of 25 eV).

have comparable intensities. The second hump in the total measured spectrum exhibits no spectral modulation, which means that a continuum could be filtered out above the point where the spectral modulation ends in the spectrum.

Chapter 3

1.5-cycle carrier-envelope phase-stabilized laser system

Physical phenomena that are sensitive to the electrical field rather than the intensity envelope, such as high-harmonic generation or above-threshold ionization require not only high electrical field strengths, but also a controlled temporal evolution of the few-cycle pulse. These demanding prerequisites are met by laser systems that provide broad amplification bandwidths, high energy pulses, and carrier-envelope phase-stabilization. In a proof-of-principle experiment it was demonstrated that even an oscillator together with a field strength enhancement from metallic nanostructures can produce high-harmonics [75]. Another promising method for intra-cavity HHG generation at MHz repetition rates is the usage of long-cavity oscillators, which builds on recirculating the pulses in a long cavity [76]. However, typically the laser system is composed of an oscillator and an amplifier, which will be described below. To avoid damage to the optics components during the amplification process, chirped-pulse amplification is applied [77]. It is based on stretching the pulse in time, which is derived from an oscillator, then safely amplifying the long pulses in a crystal, thus with low peak intensity level, followed by compressing them. The broadband seed pulses are usually produced by a Kerr-lens mode-locked Ti:Sa oscillator. These type of oscillators proved to give the shortest pulses as mentioned in the Introduction of the thesis, which is necessary since phase-stabilization requires near one-octave bandwidth even from the oscillator. Subsequent amplification can either come from stimulated emission or from parametric processes. The latter holds promise to revolutionize strong-field science due to the achievable extreme intensities and few-cycle pulses. However, because there are still challenges to it, in our case amplification takes place in a Ti:Sa multi-pass amplifier. Our laser system that generates the shortest (near-single-cycle) and most energetic NIR pulses to date will be elaborated on next.

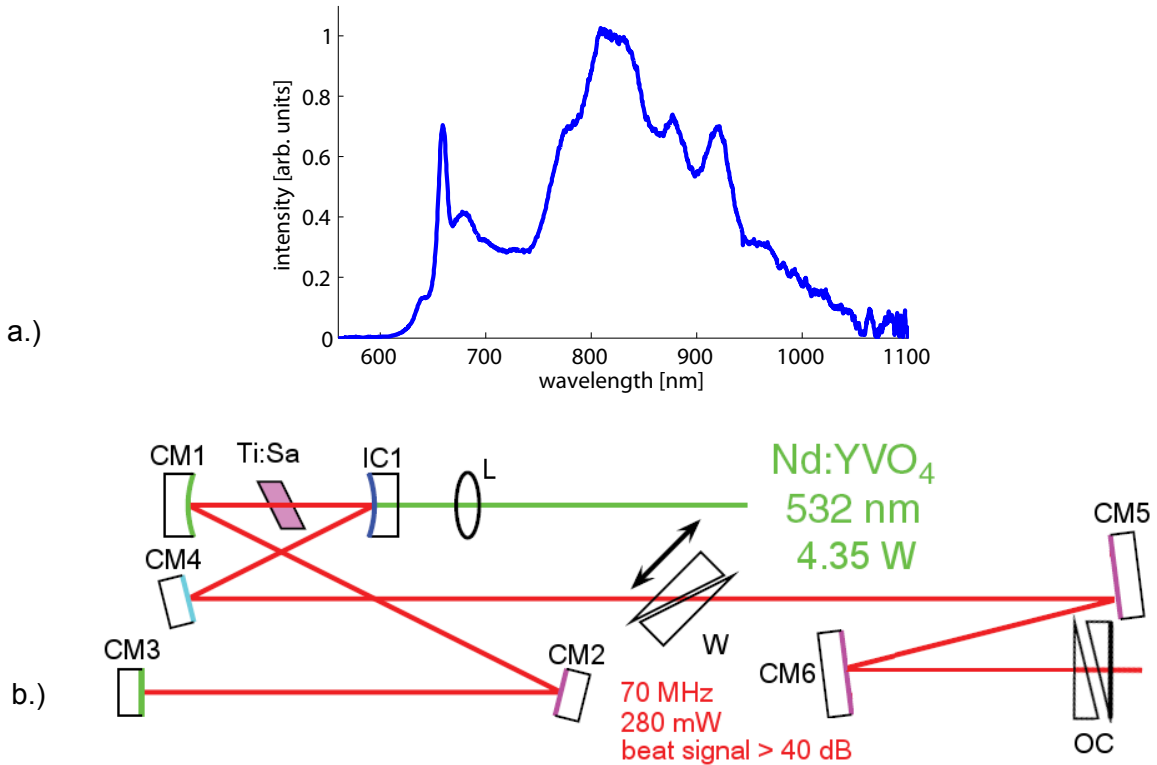


Figure 3.1: Ti:Sa oscillator. The figure shows the layout (b.) and the spectrum (a.) produced by our ultra-broadband Nd:YVO₄ Kerr-lens mode-locked oscillator. CM1-6 stand for chirped-mirrors; IC means input coupler; W is the abbreviation for the wedge used to fine-tune the dispersion of the cavity; OC means output coupler; L means lens.

3.1 The laser system

3.1.1 Oscillator

The ultrabroad-band oscillator was home-built by us, and it is very close in similarity to the commercially available Femtolasers GmbH RAINBOW. It produces pulses compressible to 6 fs pulse duration, with an energy of 280 mW, at a repetition rate of 70 MHz. A typical spectrum measured with a spectrometer (OceanOptics USB2000) and multi-mode fiber after the output couple of the oscillator is shown in Fig. 3.1. The Ti:Sa gain crystal, which is cut at Brewster-angle to minimize reflection losses, is optically pumped by a frequency-doubled Nd:YVO₄ laser. The generated pulses circulate in a cavity formed by chirped-mirrors for dispersion-compensation. After exiting the output coupler (OC) with a 15% transmission, the pulses are compressed so that they enter the periodically-poled lithium-niobate (PPLN) crystal with a high peak intensity. Here self-phase modulation (SPM) occurs, slightly broadening the bandwidth, which is necessary for phase-stabilization (section 3.2).

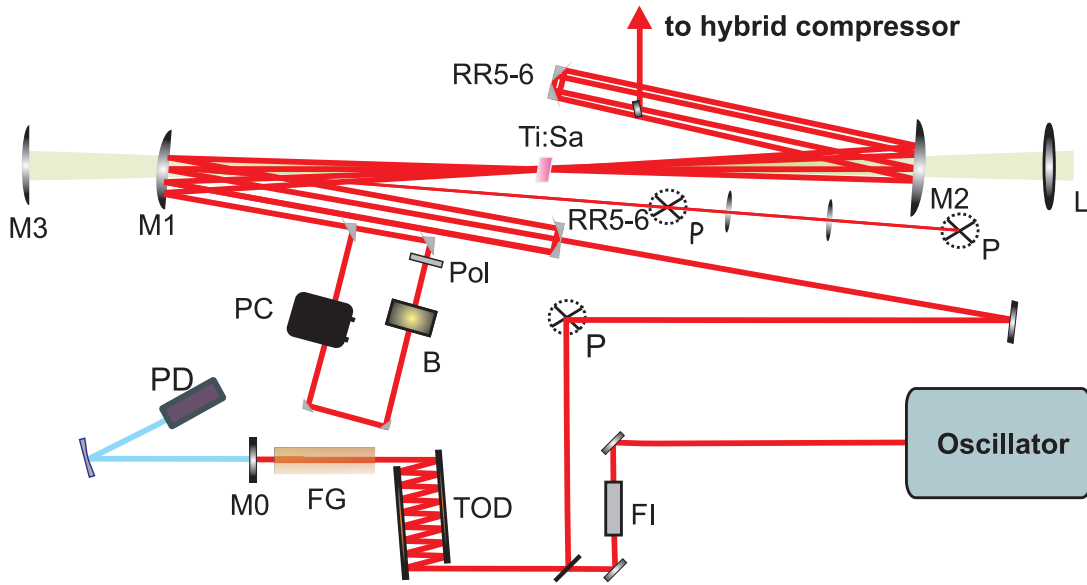


Figure 3.2: Layout of the multi-pass amplifier system. FI: Faraday Isolator, TOD: Third-order Dispersion compensation mirrors, FG: Bulk material for pulse stretching, M0-2: Dichroic Mirrors, PD: Photodetector, P: Periscope for changing the beamheight, PC: Pockels Cell for pulse selection, B: Berek polarizer, Pol: Polarizer, RR5-6: Retroreflector mirrors, Ti:Sa: amplifier crystal, M3: Focusing mirror for pump beam, L1: Lens.

3.1.2 Multi-pass amplifier and hybrid prism/chirped-mirror compressor

To reach sub-4 fs pulses of high energy, the pulses from the oscillator are amplified in a Ti:Sa multi-pass amplifier, followed by a hollow-core fiber (HCF) for spectral broadening, which supports compression to a near-single-cycle pulse duration. The key and novel technique that we have developed, leading to this extreme broadening effect, is the application of a compressor consisting of a combination of a prism and positive chirped-mirrors afterwards. A detailed description of each of these components will follow.

A sketch of the system is shown in Fig. 3.2. Only a reduced bandwidth of the oscillator will be amplified due to the narrow amplification bandwidth of Ti:Sa (725-900 nm). The 2 nJ seed signal from the oscillator is first stretched in time, according to the chirped-pulse amplification (CPA) scheme, to a duration of 20 ps by propagating through a slab of SF57 heavy flint glass. Chirped mirrors are used at this stage to precompensate for the higher-order dispersion (cubic and quartic) that the pulse accumulates during its path in the multi-pass configuration. After the fourth pass the oscillator pulses are selected at 3 kHz by a Pockels Cell (PC), which is necessary due to the low repetition rate of the pump source (Photonics Industries Inc. DM30), nonlinearities and thermal lensing in the amplifier crystal. In all the passes a Gaussian-filter (i.e. a filter with a Gaussian-shaped

transmission function) is used to compensate for the gain-narrowing introduced by the Ti:Sa crystal. In all the passes, the beam also goes through ASE-guards (ASE stands for Amplified Spontaneous Emission), circular holes, which help to obtain a clean pulse, thus with low noise before and after the pulse in time, that is a high contrast. The heart of the amplifier is the Ti:Sa crystal, which is a 3.5 mm long Brewster-cut crystal, cooled down to -70°C with a thermo-electric chiller (so that thermal effects can be kept at minimum). The total amplification factor of 4×10^6 results in pulses of 1.3 mJ energy. Operating the amplifier in saturation the energy stability becomes around 1% rms, which is an important parameter for attosecond experiments. Both spectral broadening in a later stage and phase-stabilization will be severely impacted if the energy stability gets worse than this.

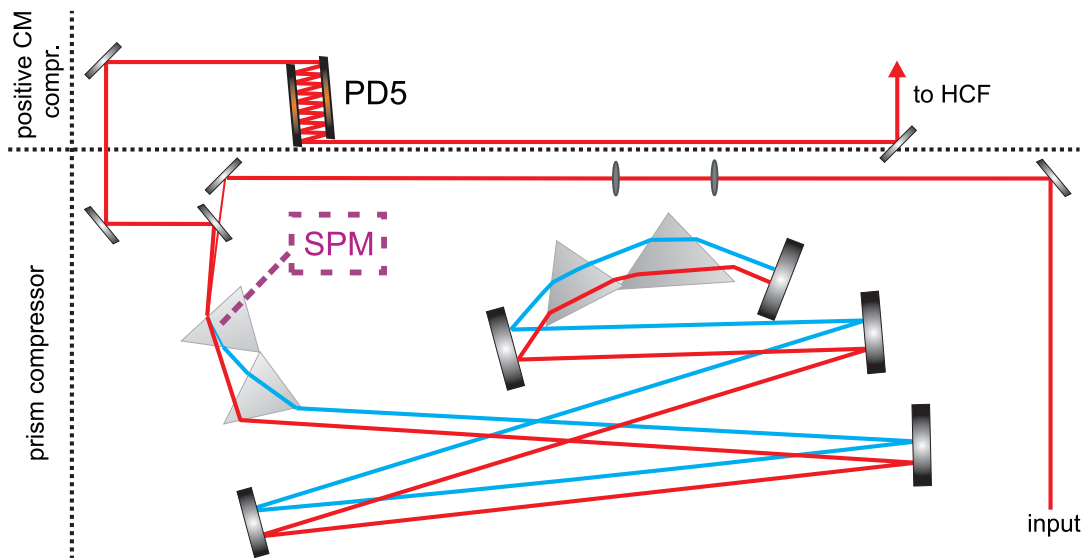


Figure 3.3: Layout of the hybrid prism/CM compressor. To avoid self-phase modulation (SPM) in the last prism of the prism-compressor that would result in spectral narrowing we rebuilt our compressor. Accordingly, due to some extra negative chirp the pulse will no longer reach its transform-limited duration in this prism. Perfect compression is instead realized after 14 reflections off two additional positive chirped mirrors (PD5).

As the pulses come out positively-chirped, they need to be compressed. In its standard form, a prism-compressor is employed. The transmission of it is around 83%. The pulses enter this compressor with a duration of ≈ 10 ps, and their positive chirp is compensated by the negative group-delay dispersion (GDD) introduced by the prism-compressor. They propagate through the last prism with their small residual negative-chirp, and close to exiting this prism, the pulse becomes perfectly compressed. Generally, when a pulse with a negative GDD and high peak intensity goes through a material (that introduces positive dispersion), self-phase modulation will happen. This phenomenon is shown in Fig. 3.3,

where a sketch of the total compressor is shown.

The shortcoming of this technique lies in the fact that unlike in the usual more beneficial case, when SPM broadens the spectrum, owing to the negative GDD it now leads to spectral-narrowing [78]. By implication, the Fourier-limited (FL) pulse duration will get longer. To eliminate this effect, we added positive-chirped mirrors following the prism-compressor. The idea behind it is that by allowing the pulses to become even more negatively chirped (by rebuilding the prism-compressor), this time throughout the last prism, we can lower the intensity level, and therefore avoid the detrimental peak intensity-dependent SPM to occur. Maximum compression now takes place after the positive-chirped mirrors. The design curves for the positive-chirped mirrors (PD5) and the ones (PC5) we used after the HCF for obtaining our sub-4 fs pulses can be seen in Fig. 3.4. The PD5 mirrors were designed such that they introduced a GDD of $+150 \text{ fs}^2$ per reflection, and thus after 14 reflections on them the pulse was elongated to a duration of around 250 fs.

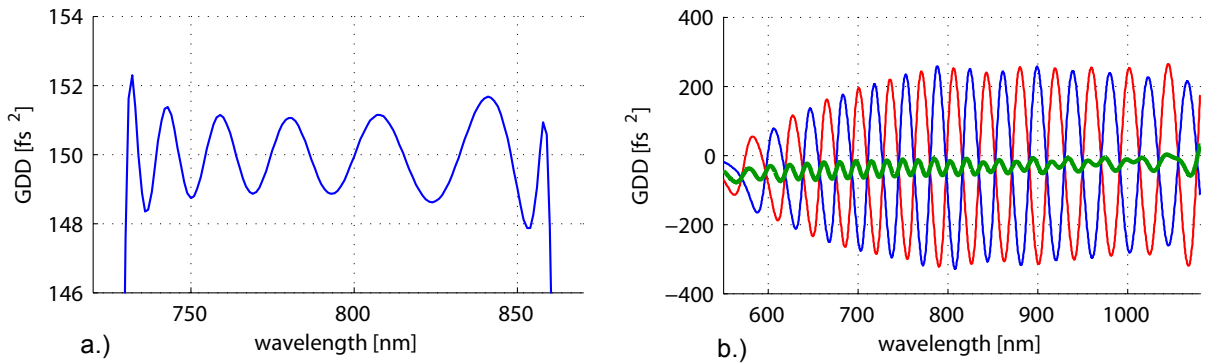


Figure 3.4: a.) Design curves of the positive chirped-mirrors and b.) of the negative chirped-mirrors. The positive ones were utilized in our hybrid compressor to alleviate the problem due to the high intensity present in the last prism of the prism compressor. The negative chirped-mirrors compressed the pulses after the hollow-core fiber to a duration of sub-3.8 fs. They were designed to be used as complementary pairs so as to minimize the oscillations in the GDD. The individual chirped-mirrors GDD curve is shown with red and blue colors, while the green curve stands for the total GDD.

The bandwidth that is preserved through the hybrid compressor is close to 70 nm (FWHM). Note that when SPM is present, spectral-narrowing will result as can be seen in Fig. 3.5. The figure also shows the spectrum corresponding to the output of previous systems, and the difference between this and ours translates to an increase of 20 nm. We performed also pulse duration characterization with a second-order interferometric autocorrelator. After the hybrid compressor, assuming Gaussian shape, the pulse was compressed to 23 fs, while with an estimated sech^2 shape, the duration was estimated to be 21 fs.

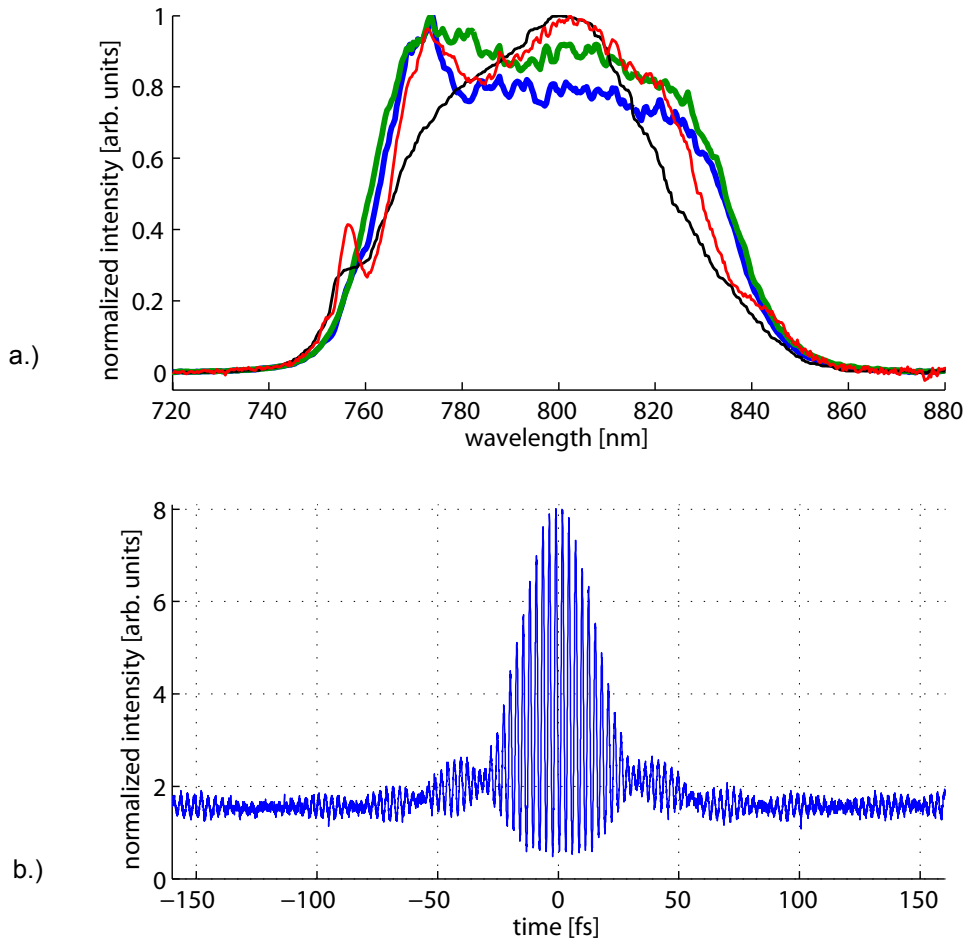


Figure 3.5: Output of the Femtopower amplifier. The part a.) in the figure shows various spectra as follows: before the prism-compressor (green), after the prism-compressor for previous system (black), after the prism-compressor with max SPM (red), after the prism-compressor (blue). It can be clearly seen that after the prism compressor our spectrum now does not shrink as opposed to the previous performance of the prism-compressor. Maximum self-phase modulation (SPM) is also visible through the narrowing of the available bandwidth, as well as a more severe modulation of the spectrum. The plot in b.) is the second-order interferometric autocorrelation trace after the hybrid prism-, chirped-mirror-compressor. The pulse duration inferred from such measurement was sub-23 fs (the exact value varying depending on the assumed temporal profile)

3.1.3 Hollow-core fiber and chirped-mirror compressor

This duration cannot be used yet for HHG to create a continuum XUV radiation. An additional step of spectral broadening is necessary to reach few-cycle pulse duration, or in our case due the extreme broadening we could reach and the well-controlled GDD of the chirped mirrors afterwards, to obtain near-single-cycle NIR pulses. There exist two major methods for further broadening the spectrum: (i) the use of noble gas-filled HCF

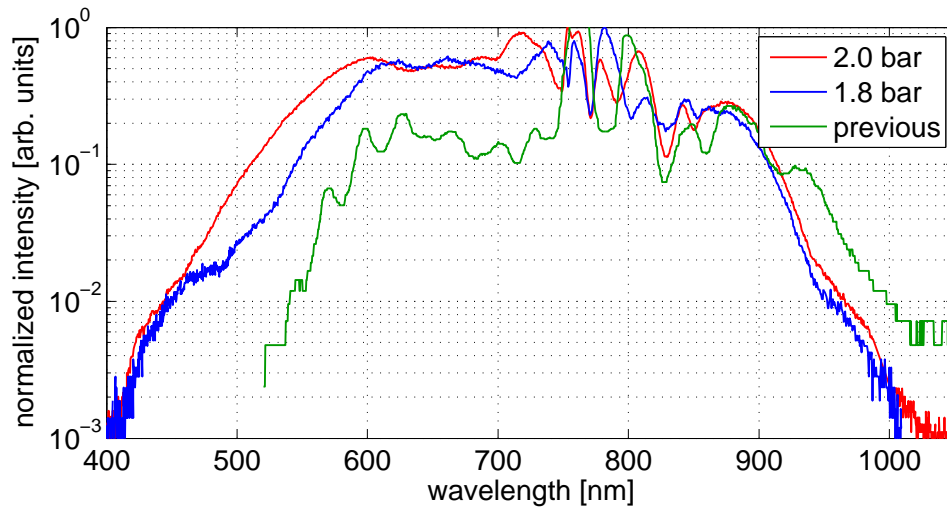


Figure 3.6: Spectral broadening after the hollow-core fiber. The red curve corresponds to a gas pressure of 2 bars, the blue to 1.8 bar, while the green curve shows the spectrum obtained by applying pulses delivered by previous Femtopower systems. The shortest pulse duration that the second-order autocorrelator measured was obtained with a pressure of 2 bars, whereas the best third-order autocorrelator measurements were reached with 1.8 bar pressure.

[68, 79], where the underlying mechanism for the effect is that of SPM, and (ii) filament generation in a cell [80], the physical explanation in the latter case being an interplay between self-focusing caused by the Kerr-effect, beam defocusing created by the plasma, pulse self-steepening, and beam diffraction. Ubiquitously the first method became the choice in many labs owing to its simplicity and low spatial-chirp at the exit of the HCF (i.e. a few-cycle pulse does reach the HHG target).

The pulses enter the fused-silica HCF with a core diameter of $260 \mu\text{m}$ and a length of 1 m, which is filled with Ne with a pressure of 1.8 bar or 2 bars. The throughput of the HCF is typically $>50 \%$. Broadening (in frequency) due to SPM is linearly dependant on the peak intensity and shows an inverse dependence on the pulse duration [79], and this is why the usage of short and powerful pulses is imperative here. At the input the pulses have an energy of $960 \mu\text{J}$ and a pulse duration of sub-23 fs, while the output delivers pulses of $500 \mu\text{J}$ with a spectrum supporting theoretical pulse-compression down to 3 fs. The various spectra corresponding to a gas pressure of 1.8 bar, 2 bars, and the performance of previous systems are shown in Fig. 3.6.

From observing the plot it becomes clear that we managed to substantially extend the spectrum towards the blue, which is an essential condition for the short-pulse compressibility. SPM induces a positive-chirp for the pulse, which means, negatively chirped mirrors (CM) had to provide the necessary dispersion-compensation. These mirrors exhibit an oscillation of their GDD as a function of wavelength, therefore we had to use

complementary pairs. For them the oscillations are shifted with respect to each other by such an amount that the resultant total GDD contains less significant oscillations. The CMs had a controlled GDD and high reflectance between 550-1000 nm. Even in spite of the mirrors' performance in terms of not covering the total spectrum available after the HCF, we reached strikingly good compression.

We carried out pulse duration measurements with two types of devices, with a (i) second-order interferometric autocorrelator (SHG-IAC) and a (ii) third-order interferometric autocorrelator (THG-IAC). The first measurement technique is based on letting two time-delayed replicas of the original pulse propagate co-linearly with each other, then generating the second-harmonic of them in a nonlinear crystal, followed by detecting their interference pattern with a photodiode. The nonlinear process in the crystal unfortunately imposes a severe limitation on the measurable pulse duration, because physically it is impossible to manufacture such a thin crystal that would enable us to phase-match the whole spectrum of the fundamental. In case of 5 fs pulses this method already reaches its still theoretically possible limit of measurement (with a 20 μm thick BBO crystal). For this reason, we could not rely exclusively on this method to accurately determine the pulse duration. However, it still allowed us to be able to roughly compare our results with previously published measurements using the same SHG-IAC technique. The measurement, as well as the calculated Fourier-limited AC function taking the whole ultrabroadband spectrum into account are shown in Fig. 3.7. The pulse duration with 2 bars of Ne pressure corresponds to 3 fs, that is during this time our 720 nm central wavelength laser field makes only 1.25 oscillations.

We performed measurements also with a THG-IAC. It uses a third-order effect taking place within a sub-micrometer layer thickness of a glass substrate (quartz glass with a TiO₂ coating), and as a result it is not subject to phase-matching limitation. Moreover, the THG signal shows a 6th power dependence on the fundamental field, so it is more sensitive to the shape of the field as compared to the SHG-IAC [81]. However, it has to be noted that this autocorrelator below 570 nm is not sensitive to the short wavelengths, since the third-harmonic is absorbed by air and above 1000 nm the sensitivity of the photomultiplier tube and the reflectivity of the dichroic mirrors is very much reduced. With this THG-IAC device the pulse duration we measured is shown in Fig. 3.8. We obtained the shortest pulse using 1.8 bar Ne pressure. On the plot the fitted transform-limited autocorrelation function has also been plotted (assuming a Gaussian shape). The fit gave a duration of 3.8 fs.

We can confirm that both measurements gave a pulse duration that is lower than 4 fs, even though both of them had limitations regarding the bandwidth they could handle. Steps were taken also towards testing an SHG-IAC device with a 10 μm thick BBO

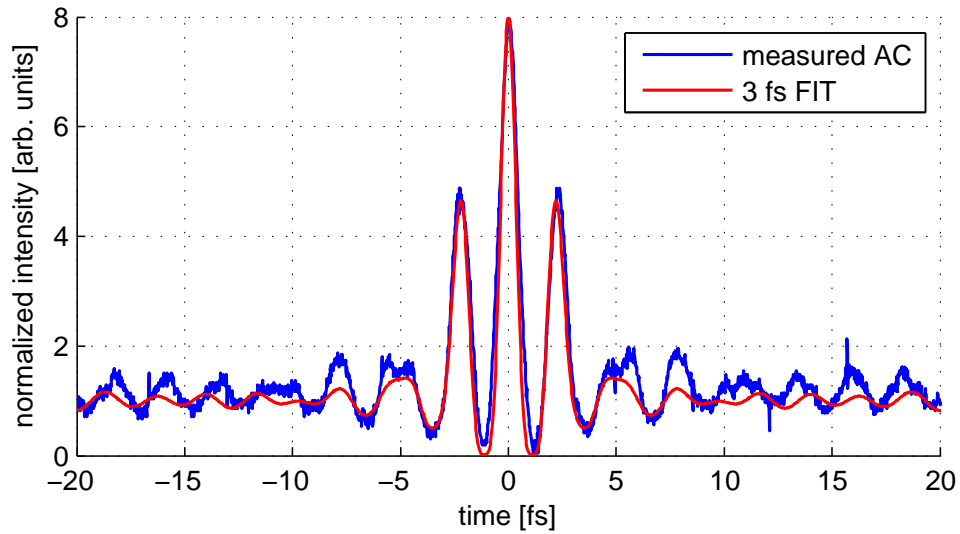


Figure 3.7: Measured second-order interferometric autocorrelation (SHG IAC) for the compressed output after the HCF. The fit autocorrelator function for the Fourier-limited pulse that the whole measured spectrum could support gave a pulse duration of 3.0 fs with a carrier-wavelength of 720nm

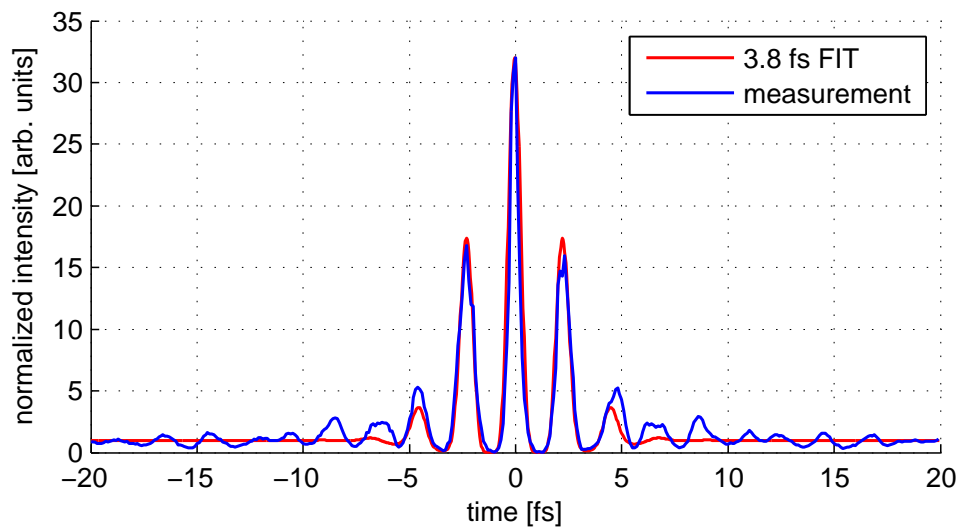


Figure 3.8: Third-order interferometric autocorrelation function (THG-IAC) showing both the measurement and the fitted function for a gas pressure of 1.8 bars. The Fourier-limited pulse duration for the fitted curve corresponds to a duration of 3.8 fs.

crystal, which could enable us to phase-match in an even broader spectral range, but unfortunately, the second-harmonic turned out to be too weak for reliable detection.

3.2 Carrier-envelope phase-stabilization

3.2.1 The carrier-envelope phase (CEP)

When the variation of the electrical field happens on a time-scale comparable to the period of the wave cycle, the exact evolution of the field becomes important. For the description of this phenomenon the term carrier-envelope phase (CEP) was called for [16], which defines the temporal alignment of the carrier wave with respect to the pulse envelope. The evolution of an electromagnetic wavepacket in time and space, which is propagating as a plane-wave, can be written as:

$$E(z, t) = \frac{1}{2} \tilde{A} \left(z, t - \frac{z}{v_g} \right) e^{i(k_o z - \omega_o t + \phi_o)} + cc. \quad (3.1)$$

where \tilde{A} is the complex envelope function, z is the propagation direction of the wave, ω_o is the carrier-wave's angular frequency, k_o is the angular wavenumber evaluated at the center frequency of the pulse ($k_o = n(\omega_o)\omega_o/c$), v_g is the group-velocity, the speed of propagation corresponding to the envelope of the pulse and ϕ_o is the offset phase or carrier-envelope phase (CEP). By a simple transformation that results in a moving retardation frame ($\xi = z, \tau = t - z/v_g$), we can identify the physical reasons for the change of the carrier-envelope phase. Thus the field can also be expressed as:

$$E(z, t) = \frac{1}{2} \tilde{A}(\xi, \tau) e^{i(\phi'(\xi)\xi - \omega_o \tau + \phi_o)} + cc. \quad (3.2)$$

Now $\phi'(\xi) = (\frac{\omega_o}{v_p} - \frac{\omega_o}{v_g})\xi$ and in this equation v_p designates the phase-velocity, which is connected to the wavenumber through $k_o = \omega_o/v_p$, while the group-velocity is the inverse of the derivative of the wavenumber with respect to frequency ($(\partial k/\partial \omega)|_{\omega_o} = 1/v_g$). It is evident from this that because the refractive index is wavelength dependent (i.e. dispersion exists), the phase-velocity and the group-velocity will not be the same and therefore phase-slippage after some propagation distance will occur. For a single pass in cavity of length L of an oscillator this gives a pulse-to-pulse CEP change of

$$\Delta\phi_{\text{CEP}} = \left(\frac{1}{v_g} - \frac{1}{v_p} \right) L\omega_o \quad (3.3)$$

As an example, a piece of glass with a thickness of $52 \mu\text{m}$ will cause a CEP change of 2π for a pulse with a center wavelength of 760 nm . This CEP-slippage manifests itself in

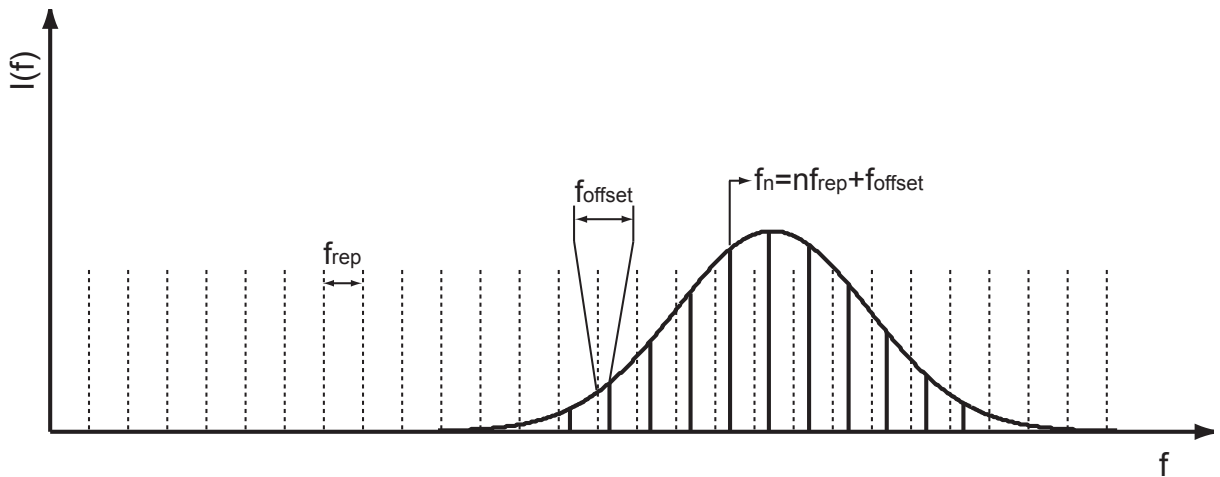


Figure 3.9: Frequency comb of a mode-locked laser. The comb (black solid lines) is offset by f_{offset} from an ideal comb (dashed lines) that would be composed of lines at integer multiples of the repetition rate f_{rep} . This offset frequency gives the rate of change of the carrier-envelope phase of a pulse (CEP), which quantity without phase-stabilization varies due to external perturbations.

the frequency domain as an offset frequency, which reads as:

$$\Delta\phi_{CEP} = \frac{2\pi f_{offset}}{f_{rep}} \quad (3.4)$$

A mode-locked laser contains millions of frequency components, which are separated by the laser repetition rate. The offset frequency, which differs from zero, and fluctuates as a result of external perturbations (air current, mechanical vibrations, amplitude-to-phase coupling due to the Kerr-effect) prevents the comb to start at zero frequency. This frequency comb is shown in Fig. 3.9. First gaining access to this parameter and later controlling its value were two major achievements. It revolutionized both frequency metrology and attosecond science. In the former application field locking both the offset frequency and one of the many modes of the frequency comb to a frequency standard ensured afterwards that every single mode could be used as a frequency standard for measuring unknown frequencies [25, 26]. In the latter case, that is in attosecond physics, the few-cycle waveforms can now be reproducibly generated in labs, with the CEP fixed to a certain value. These so-called self-referencing techniques rely on nonlinear effects, either on second-harmonic generation (f-to-2f) or difference-frequency generation (f-to-0). The conventionally used one, f-to-2f produces the offset frequency by beating the fundamental pulse' short-wavelength part with the frequency-doubled long-wavelength, thus due to the spectral and spatial overlap they interfere to generate a beat signal (offset frequency).

The interaction can be very simply expressed as:

$$2f_n - f_{2n} = 2nf_{\text{rep}} + 2f_{\text{offset}} - (2nf_{\text{rep}} + f_{\text{offset}}) = f_{\text{offset}} \quad (3.5)$$

The developed methods for stabilizing the phase, however do not allow us to know the actual value of the CEP, only its relative change can be controlled. We will see it in the next chapter that for the measurement of the CEP some other physical effects are necessary.

3.2.2 Fast compensation of the CEP change - f-to-0 method

The other scheme for detecting the offset frequency, which possesses more advantageous characteristics than the f-to-2f is that of the f-to-0. Here, a difference-frequency (DFG) signal is generated in a nonlinear crystal (typically PP-MgO:LN), which is automatically a phase-stabilized signal with zero offset frequency. The expression for the DFG process can be written as:

$$(mf_{\text{rep}} + f_{\text{offset}}) \otimes (mf_{\text{rep}} + f_{\text{offset}}) \rightarrow (m - k)f_{\text{rep}} \quad (3.6)$$

This long-wavelength signal $(m - k)f_{\text{rep}}$, which is the result of mixing the wings of the original spectrum, is then overlapped with the fundamental $(nf_{\text{rep}} + f_{\text{offset}})$ to form the beat signal (for $m - k = n$). It has to be noted that unfortunately the already CEP-stabilized DFG signal cannot be used directly as it is very low in intensity and it is not in the original spectral location as the original fundamental. In both self-referencing schemes it is necessary to work with an octave-spanning spectrum. In case of the f-to-0 method the full beam is utilized for generating the beat signal, and this has many consequences. First, due to the high peak power of the pulse not only DFG, but also self-phase modulation (SPM) will occur, which broadens the fundamental, leading to a significant increase in the strength of the offset frequency signal. Second, with the f-to-2f an auxiliary beam is split off from the main pulse, and any phase jitter that accumulates in this arm is written back to the original pulse. Now with the DFG technique the full beam is detected and then controlled without any splitting. Third, the pulse that propagates through the nonlinear crystal remains to be re-compressible due to the small amount of dispersion, thus it stays useable for later applications. Fourth, the tedious alignment issues into a tiny microstructured fiber as well as the amplitude-phase instabilities associated with the entrance of the fiber will be eliminated.

The offset frequency signal after emerging from the crystal passes through a long-pass filter (FEL 1400, Thorlabs with cut-off at 1400 nm), and is detected after free-space propagation (no fiber coupling) with an InGaAs photo-diode. Normally a beat signal of at

least 30 dB (measured with a 100 kHz Resolution Bandwidth) is desirable to reach reliable CEP-stabilization. The phase-locking electronics (MenloSystems) has the task of trying to set the beat signal to a predefined value, which in our case was $f_{\text{rep}}/4$. This means that this box generates an error signal, which is proportional to the difference between the preset value and the actual value of the beat signal, and sends a control signal to the oscillator through an acousto-optical modulator (AOM). The pump power of the oscillator is varied, and this change through the Kerr-effect results in an alteration of the CEP in the oscillator cavity. By making the offset frequency equal to $f_{\text{rep}}/4$, essentially every fourth pulse in the train will exhibit the same CEP. The selection of these "right" pulses is done by the Pockels Cell of the amplifier, which anyway has to reduce the repetition rate of the oscillator from 70 MHz to 3 kHz.

3.2.3 Slow compensation of the CEP change - f-to-2f method

The fast-loop for CEP-stabilizing the oscillator's output would normally suffice, if its output was directly used for experiments. However, since we need an amplifier, long propagation of the pulse will happen, during which small pointing movements as well as external perturbations will occur, which will cause a slow change of the CEP over time. This long path leads through 9 passes in the multipass amplifier, followed by the prism-compressor, then the positive chirped-mirror pairs, hollow-core fiber, and negative chirped-mirrors before the pulse arrives to the experiment. Evidently the resulting slow drift of the CEP needs to be compensated. To this end, we first detected the change of the CEP, which was done with an f-to-2f interferometer. A sketch of the setup with the components that we used can be seen in Fig. 3.10. Our pulse was split into two, one that went to the experiment, and another that was sent into our interferometer setup, the latter pulse with $\approx 4\%$ energy of the original having been created by reflection off our wedge pair that we used later for dispersion-control in our experiment. The pulse in our scheme then went through a nonlinear crystal (BBO) to generate a second-harmonic pulse. We filtered our light to reject the strong fundamental outside the spectral window where we wanted our useful signal to appear (explained later). Afterwards, with the help of the half-wave plate we could fine-tune the polarizations so that the polarizing cube (Glan-Thomson) could select the common polarization component of the fundamental and its second-harmonic. Again, to observe a beat signal the pulse has to have an octave-spanning spectrum, and if the f-to-2f setup is placed before the hollow-core fiber (HCF), the necessary spectral broadening is achieved by SPM in a sapphire plate. If the detection setup, however is after the HCF, provided the bandwidth is large enough, one can eliminate the need for additional broadening. Since our pulses' spectrum spans a bandwidth larger than one octave, we could benefit from this and thus we had our f-to-2f

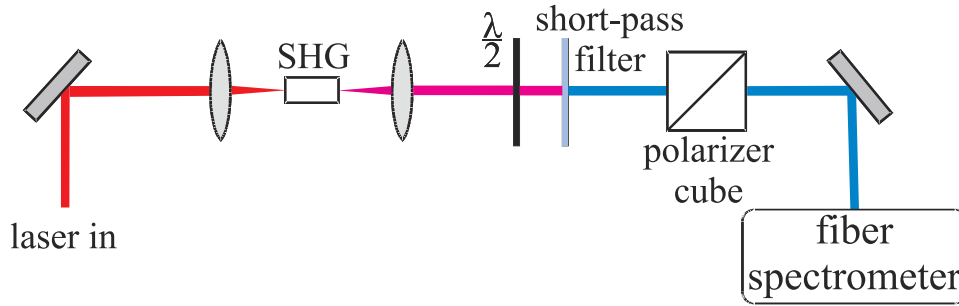


Figure 3.10: Setup for the detection of the slow CEP drift using an f-to-2f interferometer. In the figure, 'laser in' means the $\approx 4\%$ laser pulse in, which is a reflection from a surface of the wedge used for dispersion-adjustments, SHG: second-harmonic generation in a BBO crystal, $\lambda/2$: half-wave plate, short-pass filter: a filter that transmits only low wavelengths.

scheme implemented after the HCF. Thus, the advantage over previous implementations was two-fold: (i) we included in our measurement of the CEP drift the effect of the HCF, which affects also the pulse that is to be delivered to the experimental target, and (ii) we no longer use the sapphire plate, which through the SPM process would create phase-noise in the measurement arm, and apparently without influencing the original pulse. We reached this way a more accurate determination of the change of the CEP. Further characterizations of the CEP-stabilization with our unique single-shot stereo-ATI phase-meter will be discussed in chapter 4.

According to the principle of the f-to-2f, in the spectrally overlapping regions of the fundamental and its second-harmonic interference will take place, and this manifests itself as a fringe pattern. The modulation depth is highest when there are equal contributions from the two spectra that are derived from the two harmonic laser pulses. The CEP change is encoded in the fringe pattern, and this information can be obtained by applying a linear Fourier-transform spectral interferometry algorithm. Basically by keeping the fringes with our CEP-control system as much fixed as possible, the CEP change will be minimized. The error signal derived from the algorithm is sent back either to modulate the oscillator's pump power, or tiny movements are done to one of the prisms in the prism-compressor (in the same direction as how the pulse is propagating) to reach a dispersion-induced CEP change. The latter feedback method proved to give the best CEP-stabilization performance (i.e. lowest standard deviation for the CEP change) and long-term operation of phase-stabilization due to the decoupling of the control signals (fast and slow compensation of the CEP) back to the oscillator and the amplifier [82]. An exemplary fringe pattern is depicted in Fig. 3.11.

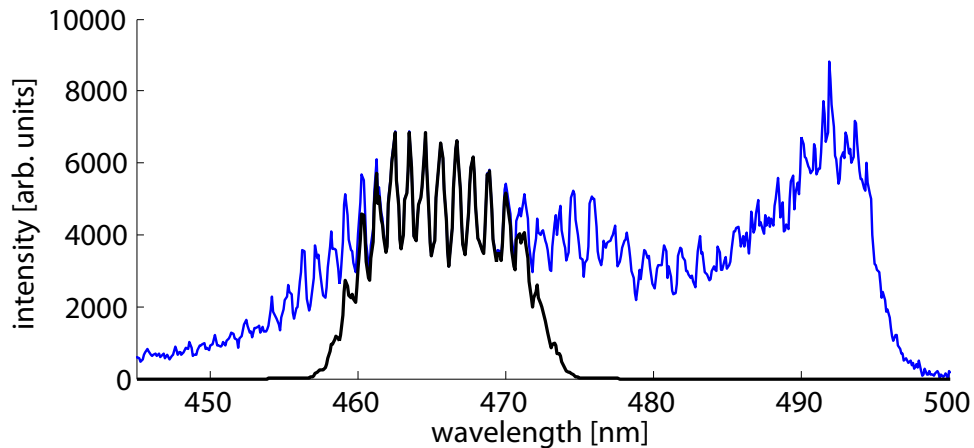


Figure 3.11: Fringe pattern of the f-to-2f slow-loop. The fundamental and the second-harmonic overlap in the same spectral range (between 450-480 nm in the plot) and an interference between them appears (blue line). For easier viewing purposes, the spectral part that contains pure fringes has been highlighted by a black line. From the movement of these fringes, relying on Fourier-transform Spectral Interferometry it is possible to extract the changes in the CEP and then use this information to control the CEP.

3.3 Summary

In summary, we have shown a laser system that can produce NIR pulse with sub-4 fs duration. The key to achieving the necessary spectral broadening was the hybrid compressor design and implementation, which helped us keep the pulse duration from the Ti:Sa amplifier short. As a direct consequence, we could enter the HCF with the highest possible peak intensity, and an efficient broadening towards low wavelengths resulted. Further proofs for our short duration are given throughout the thesis.

Chapter 4

Single-shot CEP measurement of intense few-cycle laser pulses

4.1 Introduction

Investigating strong-field phenomena, which exhibit high sensitivity to the electrical field requires precise control over the shape of the field under the envelope. The term carrier-envelope phase (CEP) serves as the property to describe this alignment of the field, the meaning of which and its stabilization with interferometric techniques was elaborated on in the previous chapter. In this chapter we are interested in knowing the actual value of the CEP - not only in measuring and stabilizing its rate of change, the offset frequency.

Several methods have been demonstrated [25, 26, 83, 84] and proposed [85] so far, capable of measuring the change of the CEP. All of the techniques require, however phase-stabilization and they can measure only the average of many shots. Apart from the already extensively discussed f-to-2f method, other proof-of-principle measurements have been carried out that exploit various physical phenomena, and such are solid-state detection of the carrier-envelope offset frequency (f_{ceo}) via control of quantum interference in semiconductors [83, 86] or even the relatively simple concept of linear interferometry [84] can be applied to derive the evolution of the CEP. Especially the former technique, as well as the CEP-dependent photoemission on metal surfaces [87] hold the future potential of substantial reduction in device size for f_{ceo} detection. Determination of the CEP and not only its rate of change has become possible through other novel experiments. Access to this vital parameter of the few-cycle pulse is possible through the detection of THz emission by looking at the amplitude and polarity of the THz signal generated in a plasma [88]. Electron localization during the dissociation of D_2 was demonstrated [31], which exhibited also a sensitivity to the CEP, and it was the first experiment carried out to show sub-fs light-driven electron control in molecules.

Another category that allows the retrieval of the absolute phase relies on strong-field phenomena, the two most successfully used ones being that of high-harmonic generation (HHG) and above-threshold ionization. As a matter of fact, in HHG with the stabilization of the phase using the self-referencing technique, control of the harmonic structure becomes possible, which shows a dependence on the CEP in the cut-off region [27]. To the formation of this high-energy spectral region (a continuum) in case of a few-cycle pulse only the part close to the peak of the fundamental contributes, and since this region of the electrical field is altered when the CEP is changed, this variation will leave its fingerprint on the shape and the location of the cut-off part. This idea has been taken to another level recently with the insight that each half-cycle of the pulse will create its own cut-off energy. Earlier it was predicted in theory [89] that each half-cycle will generate an XUV burst with a cut-off energy proportional to the extrema of this half-cycle, and subsequently this concept was experimentally implemented and used to retrieve the CEP [74]. This method, however demands 0.1 mJ energy, requires again phase-stabilization, and has a drawback that the average CEP of many shots has to be detected (2000 shots). The other important physical effect, where CEP dependence manifests itself is based on the observation of the spatial asymmetry of electrons in above-threshold ionization [34, 36]. The details of such measurements will be discussed in this chapter. The state-of-the-art until now used the average of 300 laser shots for determining the change of the CEP and later via a feedback to the laser system to control its value [82].

There have been a number of theoretical proposals for the single-shot measurement of the CEP [90–93], and the experiment getting closest to this challenge could measure single-shot rate of change of the CEP, and for non-consecutive pulses [93].

In this chapter we show the first single-shot CEP measurement of intense few-cycle laser pulses [35]. According to the structure of this chapter we first give a short description of our measurement apparatus, followed by presenting the conventional representation of phase-stabilized pulses, which was developed previously by others using multi-shot measurement devices. Enabled by our single-shot measurement capability, we have developed a new method for determining the CEP of consecutive pulses unambiguously, that is with no phase-ambiguity, without the need for CEP-stabilization by relying on comparing the left-right asymmetries of photoelectrons with different energies. This will be the main topic to be outlined in detail afterwards. Our method now allows us to separate the device precision from the CEP fluctuation, which in turn permits the determination of our unprecedentedly high CEP measurement precision and allows the characterization of phase-stabilization. Sensitivity of the phase meter to the energy fluctuation can be

assessed, as well and furthermore we present a novel dispersion-free pulse duration measurement, which exhibits a sensitivity increasing with pulse duration approaching the single-cycle limit.

4.2 Single-shot stereo-ATI measurement apparatus

The CEP measurements were performed with a single-shot stereo-ATI phase meter, which is composed of two ideally identical time-of-flight spectrometers in opposing orientation to each other (Fig. 4.1). They measure ATI electron-spectra from xenon atoms at the two sides of the polarization axis of few-cycle laser pulses. Xenon gas is located in a small cell in the center of the apparatus held at a constant pressure of 1.6×10^{-2} mbar by continuous gas inlet and simultaneous pumping. In all other parts of the apparatus, differential pumping by a turbo pump maintains a high vacuum of 4×10^{-6} mbar. This is necessary for the safe operation of the microchannel-plate (MCP) detectors and it ensures free flight of the electrons.

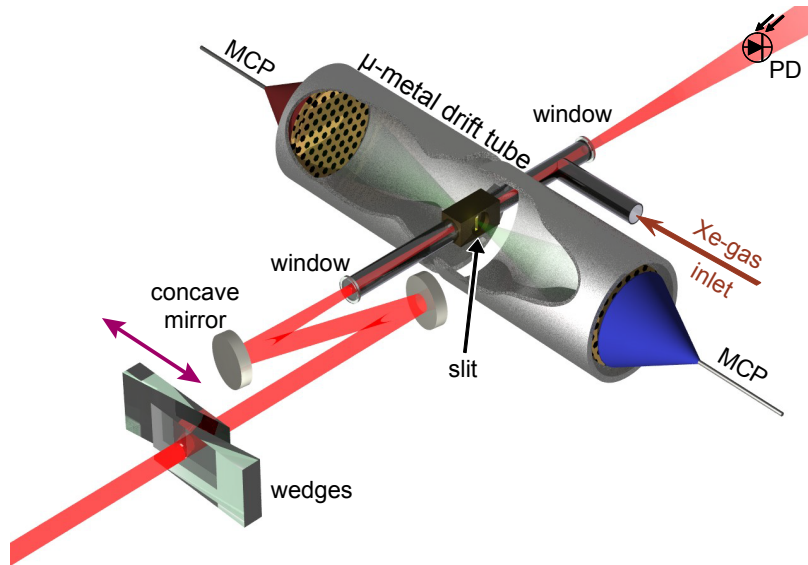


Figure 4.1: Single-shot stereo-ATI phasemeter (courtesy of M. G. Schätzel). Two opposing time-of-flight spectrometers are mounted in a compact high vacuum apparatus, carefully shielded (symbolized by the mu-metal-shielding tubes) from electrical and magnetic fields. The xenon atoms that fill the inner part of a differential pumping stage are ionized near the focus of the laser beam, and enter the ultrahigh vacuum drift-tubes through the vertical slits. The electrons are detected with a pair of microchannel-plate detectors. The color-coding of the detectors corresponds to the colors used in the time-of-flight plots in Fig. 4.2 and all the other subsequent graphs. Vacuum pumps are not shown.

A 10 % split-off of the 400 μJ total laser output is focused into the interaction cell by a concave mirror with a focal length of 250 mm. Alternatively, the apparatus can be operated as a non-invasive CEP diagnostics tool by using the entire beam and focusing it slightly. Electrons are ionized by the linearly polarized laser field close to the focus at an intensity of $8 \times 10^{13} \text{ W cm}^{-2}$ and leave the cell through 0.7-mm-thin vertical slits which hold back electrons generated outside the laser focal region. After a 15.5-cm-flight, the electrons are detected by microchannel-plate detectors (Del Mar Photonics). A -25 V blocking potential allows only electrons with a kinetic energy $>25 \text{ eV}$ to reach the detectors. As explained later and in section 2.3.1 of chapter 2, these high-energy electrons have a much higher phase-sensitivity than low-energy electrons. The drift tubes and the interaction zone are protected from electric and magnetic fields by a mu-metal-shielding. The signals of the MCPs are amplified by two wide band amplifiers and recorded by a digital oscilloscope (Tektronix). With the digital data acquisition we are able to consecutively record pulses up to 100 kHz repetition rates. Currently, the maximum number of pulses is limited to 4500 shots by the oscilloscope (due to memory constraints), which corresponds to 1.5 s at 3 kHz repetition rate of the laser. With suitable digitizer cards, which are now available commercially, this limit vanishes and recording of all laser shots is technically possible. Moreover, our method moreover is non-invasive as the electron density in the target is too low to affect the laser beam. It can even be realized at an intermediate focus in a laser beam, without any impact on the spatial and temporal characteristics of few-cycle pulses.

Our CEP-stabilized laser system is composed of a Ti:Sa oscillator and a multipass amplifier as described in chapter 3. The CEP measurements were carried out for pulses with a duration of 4.1 fs. In order to ensure that the pulses have identical CEP, we employ an f-to-0 phase-stabilization scheme ("fast-loop") for the oscillator and an f-to-2f setup ("slow-loop") after the amplifier.

4.3 Conventional representation of phase-stabilized pulses

In our method for determining the CEP of pulses as already noted we rely on above-threshold ionization (ATI) in an isotropic gaseous medium (Xe). The linearly polarized few-cycle pulse generates photoelectrons that are emitted in two opposing directions. The key feature of this emission that is a signature of the specific evolution of the few-cycle pulse under the envelope is the asymmetry observed in the number of electrons reaching the left or the right MCP. There are two types of photoemission processes that play a role: one that creates direct and another that generates rescattered photoelectrons (see sections 2.3 and 2.2.2 in chapter 2 for the theoretical explanations). The largest portion of the

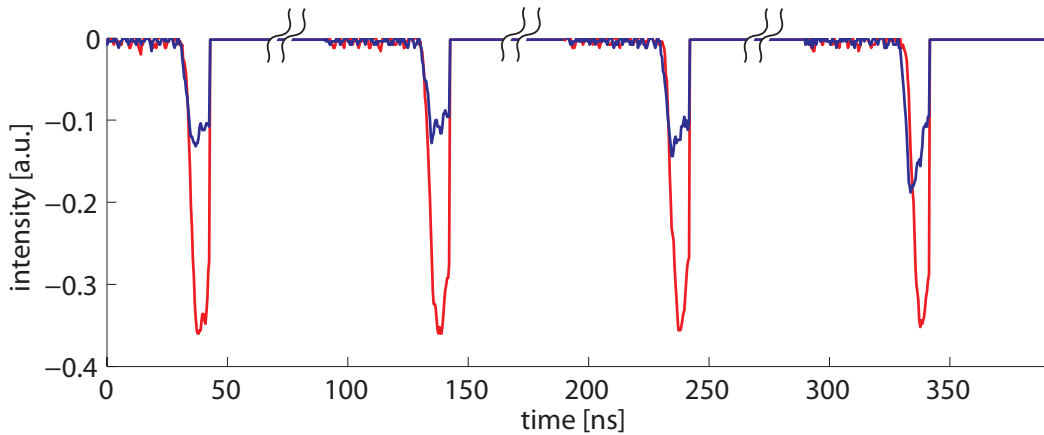


Figure 4.2: Single-shot time-of-flight (TOF) signal of consecutive laser pulses with CEP-stabilization. The laser repetition rate was 3 kHz, therefore the time-delay between successive pulses was 0.33 ms. The time axis in the TOF data should not be confused with the laser pulses' arrival time, and to stress this difference the discontinuity was indicated with two wavy lines. Red and blue curves correspond to the electrons detected by the left and right MCPs in accordance with the color coding applied in Fig. 4.1. The CEP-setting was chosen such that a pronounced asymmetry was visible between the two MCP signals.

total electron yield is coming from the low-energy direct electrons (<25 eV under typical conditions of our experiment), while high-energy rescattered electrons that return to the ion core represent a smaller number, approximately 1 % part of the total electron number. In our experiments we rely on the CEP dependence of these rescattered electrons (that have energies up to 60 eV in our case) that form a plateau [51] in the ATI photoelectron spectrum (as also explained in section 2.3).

Our steteo-ATI phase meter acquires single-shot data for consecutive pulses, and such raw measurement for CEP-stabilized pulses as obtained by the digital oscilloscope can be seen in Fig. 4.2. The CEP was setting was such that a strong asymmetry in the signals for the two channels, MCP left and right, were observable. From these first data it is not possible to directly determine the CEP, and further processing of the data is necessary. The useful signal that facilitates the establishment of a connection between theory and experiment is the spectrum of the ATI electrons. To this end, a conversion needs to be done between the time-of-flight (TOF) data and the spectral representation. The photodetector (PD), situated after the exit window of the phase meter as shown in Fig. 4.1, is used as a trigger signal for our single-shot measurements, and thus it serves as a reference point in time. This means that the time difference between the arrival time of light into the PD and the arrival time of the photoelectrons into the MCPs would correspond to the flight time of the electrons in the drift tube. However, the measured signal appears on the oscilloscope screen, and therefore the propagation time of the signal

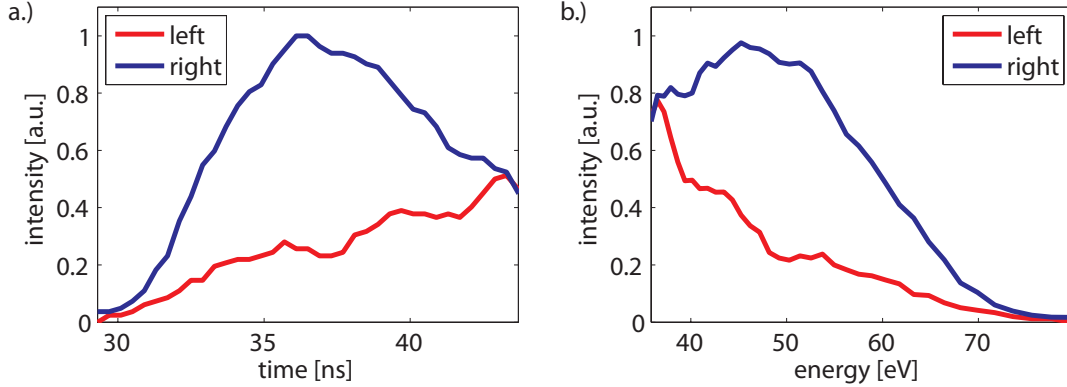


Figure 4.3: a.) TOF and b.) energy representation of single-shot ATI electrons. The red and blue curves again indicate the electrons arriving to the left and right MCPs, the same two colors as also used in Fig. 4.1 and Fig. 4.2. The CEP of this specific pulse was such that it resulted in a considerable difference between the the left and right channels.

from the MCPs to the oscilloscope has to be subtracted. Knowing the total travel time of the electrons (either by measuring previously the flight tube length or by subtracting the delay-time between the MCP and the oscilloscope from the total time) it is now possible to carry out the time to energy conversion.

Such time-of-flight electron spectrometers are used ubiquitously in science, such as for XUV spectroscopy, nuclear physics, ion and mass spectrometry. Charged particles are accelerated by a static electric field, and if they have the same charge but different mass, they will reach the detector at various time instances. This allows one then to determine the masses of these particles. In our case they are used to measure the electrons' velocity, thus their kinetic energy. The conversion of our TOF data to energy can be done by using simple maths. An electron with a velocity v and a mass m_e will acquire an energy $E = m_e v^2 / 2$. Knowing the travel time of the electron t and the length of the drift tube L , naturally $v = L/t$. After substituting this into the equation for energy, followed by a derivation with respect to time, one arrives at $dE/dt = m_e L^2 t^{-3}$. If we have a function $f(t)$ that represents the TOF data, and we want to convert our data to $g(E)$ expressed as a function of energy, we need a straightforward stipulation that the two functions have to have the same area under their curve, that is $f(t)dt = g(E)dE$ (energy conservation). This gives $g(E) = f(t)dt/dE = -f(t)t^3/m_e L^2$. Another important property of our electron spectrometer is its energy resolution. What influences this quantity are the length of the drift tube, the time resolution (set by the acquisition device), and the energy region we want to look at. By similar consideration as discussed above, the exact dependence of the resolution on these physical quantities can be expressed as:

$$\Delta E = \frac{2\sqrt{2}\Delta t}{m_e L} E^{3/2} \quad (4.1)$$

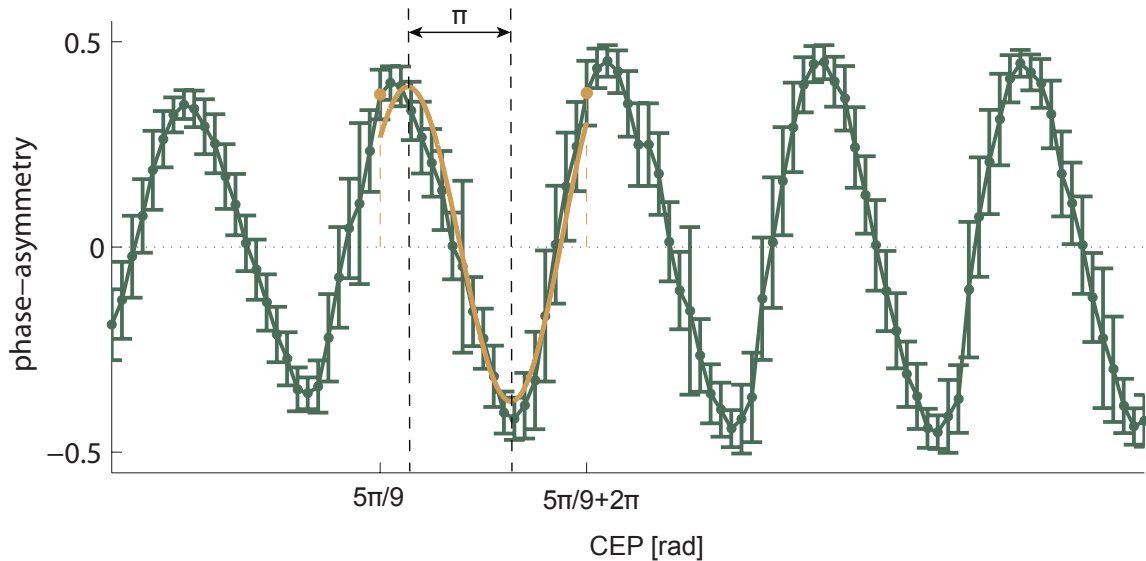


Figure 4.4: Phase-scan performed with a laser running in a phase-stabilized mode. At each CEP setting (the step size being $\pi/10$) we calculated the phase-asymmetry parameters of 4500 shots (integration done for the whole energy range), and the corresponding mean value, as well as a curve (dark green) created by connecting these measurement points are shown in the figure. We selected one full period in this scan (a 2π interval), its ends highlighted by two brown-colored dots. Furthermore we fitted a damped sinusoid onto the data in this range, which is shown in brown. The CEP values for the two ends were obtained from TDSE calculations.

In our measurements we utilized a drift tube with a length of 15.5 cm, the time-resolution of our digital oscilloscope corresponded to 0.4 ns, and we were interested in the region 30-70 eV, where the rescattered electrons were located. In this energy range, this gave us a resolution of $\approx 2.2\%$. The TOF data along with the energy representation can be seen in Fig. 4.3.

It is possible to quantify the phase-asymmetry of a pulse, and the usual way of doing it is based on the integration [36] of the whole spectrum for the left and right channels or integrating only in a certain energy range (designated as P_L and P_R , respectively). If PAP stands for phase-asymmetry parameter, then it can be expressed as:

$$PAP = \frac{P_L - P_R}{P_L + P_R} \quad (4.2)$$

This parameter shows a close to sinusoidal dependence on the CEP, which has been analyzed both experimentally [36] and theoretically [54, 55]. The established method for obtaining this curve until now was through a measurement done on a phase-stabilized laser, by averaging over many shots using a multi-shot phase meter. The task was to acquire averaged CEP values at user-defined nominal CEP settings, the whole scan being

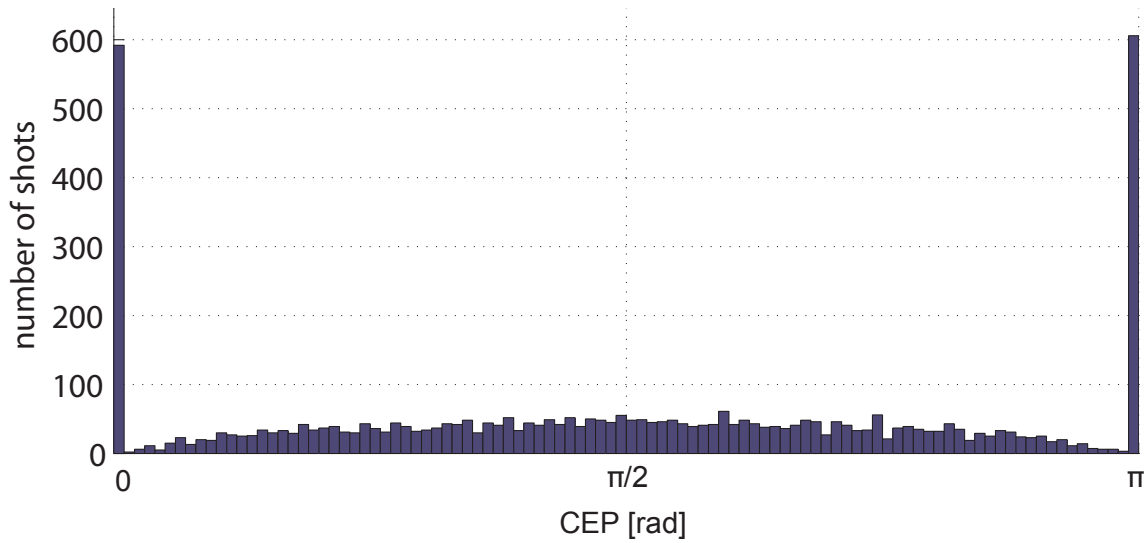


Figure 4.5: Histogram showing the distribution of non-phase-stabilized pulses. Due to the non-monotonously changing fit curve the conversion from phase-asymmetry parameter to CEP is viable only in a π range. Even in this smaller CEP range this assignment gives a result that is not satisfactory, since the distribution goes up at the edges, while it should be actually flat everywhere.

performed for a large range of CEPs. The result of such a scan, done in steps of $\pi/10$, is plotted in Fig. 4.4, where the phase-asymmetry parameter was evaluated based on the integrations carried out for all energies. The total range of CEP values lie in an interval of approximately 10π . The mean values for the phase-asymmetry parameter were calculated for 4500 shots at each step of the scan, and these were connected with a line as seen on the plot. Naturally, the phase-stabilization is not perfect, and this is reflected in the standard deviation, which shows the fluctuation of the CEP. The standard deviation varies along the sine-like curve since the phase meter exhibits the highest sensitivity close to the zero-crossing of the phase-scan, where the phase-asymmetry parameter changes rapidly, while our stereo-ATI measurement device shows the lowest sensitivity at the top of the phase-scan. Consequently, both the device precision and the imperfect phase-stabilization are present, and they are seemingly inextricably intertwined with each other. The phase scan at this stage allows one to get only relative CEP values. In order to extract the real CEP one has to solve the time-dependent Schrödinger equation (TDSE) and compare the simulation with the experimental phase-scan. This phase assignment will be explained more in detail later. The thus obtained CEP values at the two ends of a 2π range can also be seen on the plot. Furthermore, we fitted a damped sinusoid to the mean values inside this 2π interval (brown curve). Experimentally, the physically measurable quantity is the phase-asymmetry parameter as determined from the TOF data, but our ultimate goal is to know the CEP. Now this fit curve serves as the means to convert our phase-asymmetry

values to CEP - for each of our recorded shots. Unfortunately, we have to be content with being able to do this conversion only in a narrow range of π using this method. To create a one-to-one connection between phase-asymmetry values and CEP (i.e. without ambiguity) it is necessary to have a monotonously changing fit curve, which is not the case in the whole 2π interval. Only between the two maxima of the fit curve is this condition satisfied (thus the π range). We also recorded shots with no CEP-stabilization running. A check is possible to see whether our fit curve is roughly good enough and this can be achieved by requiring that the converted CEP values of the non-phase-stabilized shots show a flat distribution. This simply means that during our measurement all CEPs should appear with equal likelihood. Such distribution has been plotted in Fig. 4.5 for a π interval by utilizing the fit function obtained from a previous phase-stabilized measurement. As we can see it, the edges of the histogram go very high, which is the result of many shots being badly converted owing to the flattening out of the sine curve as we approach the maximum of the fit curve. This error in the phase asymmetry-CEP mapping cannot be cured even if one tries to choose a different fit function (such that for example the fit function rises higher so that even the shot with the highest phase asymmetry parameter will stay below the fit function). There are two reasons for the failure of this effort: (i) this conversion method builds on using phase-stabilized shots, which fluctuate in their phase as a consequence of the imperfect phase-stabilization, and (ii) phase-ambiguity exists, because our conversion curve is not changing monotonously as a function of CEP.

4.4 Parametric representation of non-phase-stabilized pulses

There is, however, another method that we have conceived, which solves the above problems. In the past it was already noticed by others [36] that the phase-asymmetry parameter becomes phase-shifted when this parameter is evaluated for different energies, starting from the lowest energy values and all the way until the highest observed photoelectrons. This feature can be readily seen on a 2D plot in a false-color representation as shown in Fig. 4.6 for our experimental data. The phase-asymmetry value has been encoded in the color representation, x axis being the CEP, y axis the energy. This plot stems from our single-shot analysis, therefore it represents single-shot, non-phase-stabilized pulses, unlike before when phase-stabilized, multi-shot data had to be used [36]. It can be seen that the phase-asymmetry parameter assumes a higher absolute value when the ATI photoelectron energy increases. The phase-shift between different energy values is an important property of the rescattered photoelectrons, and we heavily rely on this to overcome the above difficulties associated with the phase-ambiguity and the coupled nature (device precision

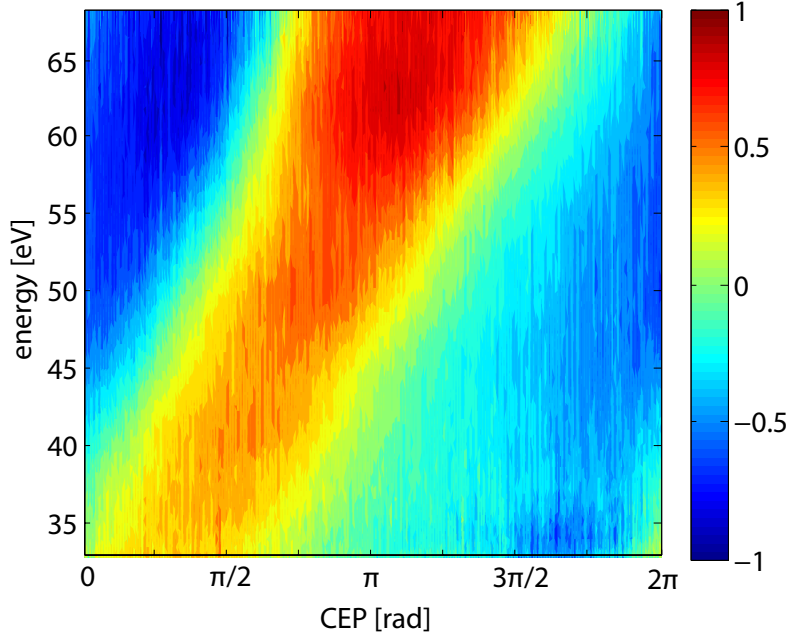


Figure 4.6: Phase asymmetry plotted as a function of both the CEP and the energy. This 2D plot has been reconstructed relying for the first time solely on single-shot, non-phase-stabilized pulses. There exists a gradual phase-shift with the increase of the energy. This feature enables us to eliminate phase-ambiguity so that we can make use of the non-phase-stabilized pulses, and not the phase-stabilized ones that inherently contain the CEP-fluctuation of phase-stabilization.

and CEP fluctuation being inseparable from each other) of the measurement technique so far. The other fact that we have not exploited yet, which is unique to our measurements is that for the first we can measure the CEP on a single-shot basis. We will see that this, in turn means we can make use of non-phase-stabilized pulses. As a result, CEP measurements will be viable in the future even for large-scale systems, which cannot be phase-stabilized in advance (as of now), that is where performing a phase-scan curve is not realizable.

Regarding the mentioned phase-shift, we can choose two different energy ranges for the evaluation of the phase asymmetry parameters. These two energy ranges for our integrations, where the phase-asymmetry parameters are calculated, were 37.9 eV to 57.5 eV for the first, and 57.5 eV to 64.8 eV for the second parameter. These ranges are indicated with dark green and dark purple areas on the time-of-flight (TOF) and energy spectra for the cosine and anti-cosine waveforms of the laser pulse in Fig. 4.7. During our CEP retrieval we used the TOF spectra, because these constitute the raw, unprocessed data. Earlier in chapter 2 we also plotted the excursion times of the photoelectrons that are accelerated under the effect of the field and this can be seen in the top plot of Fig. 2.2

on page 18, where the color coding red and blue translate to main propagation into the left or the right MCP.

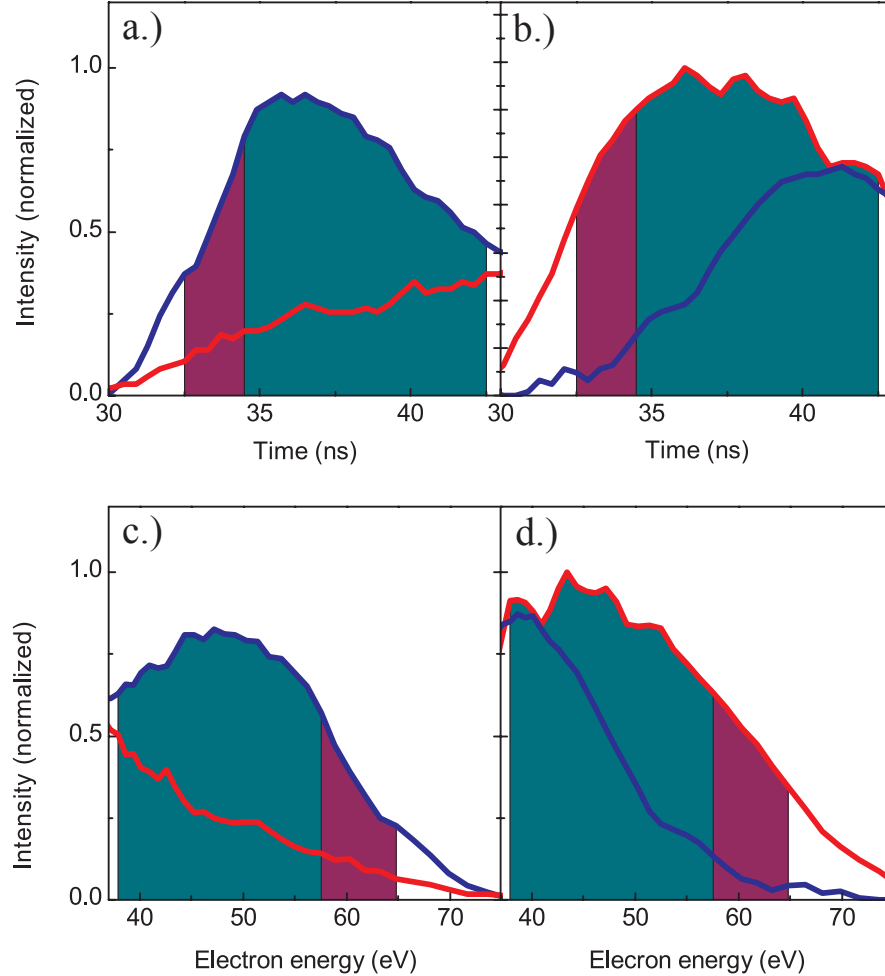


Figure 4.7: a.)-b.) Experimental time-of-flight spectra and c.)-d.) converted energy spectra for cosine (left plots) and anti-cosine (right plots) pulse. Red and blue means final arrival to the left or the right MCP, respectively. We used a blocking potential of -25 V to let only electrons with a kinetic energy >25 eV to reach the detectors and therefore only the high energy parts of the spectra have been plotted. The dark purple and dark green shaded areas show the two integration ranges that we used to derive two phase asymmetry parameters, x and y , respectively.

We can plot two phase-scans, their phase asymmetry parameters derived from the two energy ranges, for the case when the phase-stabilization is running, and also for the single-shot non-phase-stabilized case, and these are shown in Fig. 4.8. The phase-scan builds on a conventional, multi-shot method, while our single-shot curve is directly coming from single-shot, non-phase-stabilized data, as obtained from using our method described below. We chose the above integration ranges so as to obtain high phase asymmetry values for both curves, which as a result gives also low measurement noise. These two

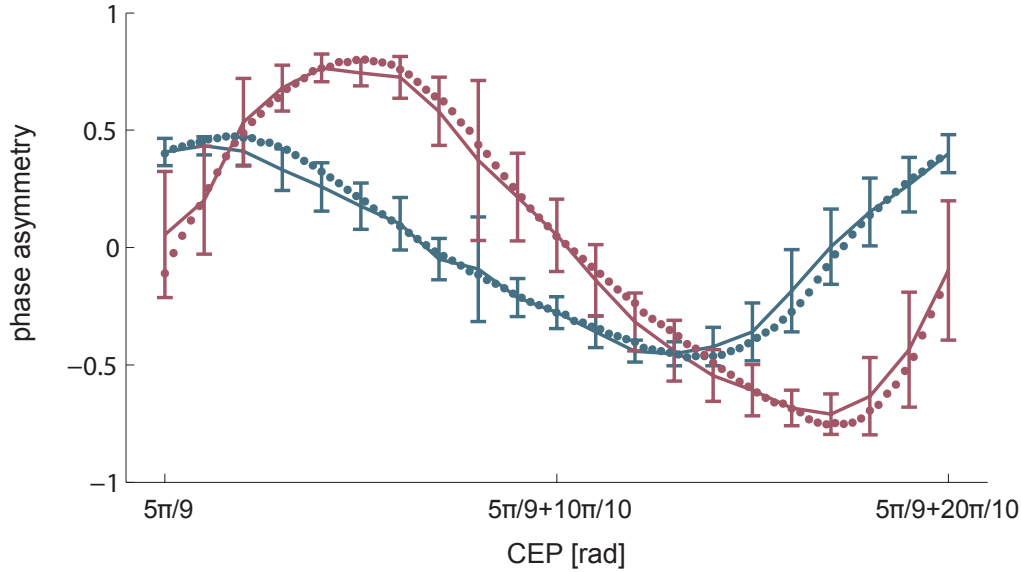


Figure 4.8: Phase asymmetry parameters x and y for both a CEP-stabilized (continuous line with the error bars indicated) and non-CEP-stabilized (dots) laser pulses. The so-called phase scan for the CEP-stabilized case was performed by stepping the CEP in $\pi/10$ step-size with the help of a pair of wedges (see the measurement apparatus of Fig. 4.1). The mean values of the curve (where the error bars, so the standard deviations are also shown) were the average of 4500 shots. The plot corresponding to the non-CEP-stabilized mode of operation of the laser was obtained by applying our developed method, and thus it was reconstructed directly from single-shot data. Depending on the selection of the spectral ranges from which the parameters are derived the sinusoidal curves in both cases are shifted, in our case by 60° .

parameters are linked to each other, since a high maximum phase asymmetry will result in a high CEP measurement sensitivity in the region of the zero-crossing of the phase scan curve (where the gradient of the sin-like curve will be maximized). The two curves, as one can see it in the figure, are phase-shifted by approximately 60 degrees with respect to each other. If two signals with sine-like dependencies are phase-shifted, one should recall that then a two dimensional Lissajous-representation is called for. A Lissajous plot is the visual representation of a system of parametric equations. Complex harmonic motion can be described with it if the two components x and y are sine-like curves. A complicated structure will be created if the two signals' harmonic frequencies are not equal to each other, but if they are the same, and only a phase-shift as well as different amplitudes are associated with them, then we will obtain an ellipse. Depending on the phase-shift the major and minor axis lengths will be varied, and the inclination angle between the major axis and the x axis will be altered. It is used in many fields of science - in electronics for example it serves as the visualization tool to obtain the phase-shift introduced by a linear time-varying system, by connecting the input and output signals to the two channels

of an oscilloscope in order to observe the trace that the time-varying signal follows. In optics, the polarization of a field can be visualized, such as that of elliptical polarization. Moreover, connected to high-harmonic generation it is used to follow the trajectory of an electron as it is accelerated by the laser field with a polarization other than linear [94, 95]. In our case, the two components x and y will be the two phase asymmetry values and the parameter for the two axis that is changing linearly is the CEP. Along this 2D curve one and only one location is assigned to each CEP value (in a range of 2π). Phase-ambiguity is therefore nonexistent in this representation. We plotted non-phase-stabilized laser shots, so with random CEPs using the parametric plot viewing, and this graph can be seen in Fig. 4.9. The CEP in the figure was retrieved by performing one-dimensional TDSE simulations (by G. G. Paulus) on rescattered electrons with parameters used in the experiment. The reason for the somewhat deformed so not perfectly shaped ellipse is that the phase asymmetry curves are not perfectly sinusoidal (see dotted lines of Fig. 4.8), and moreover our two MCP detectors were not identical. The figure shows consecutively recorded shots, and it demonstrates that they are arriving in a random fashion, that is the CEP values are uncorrelated with one another. This randomness justifies our assumption with regard to a flat distribution for the CEPs of a free-running laser.

The prerequisites are given (single-shot capabilities and no phase-ambiguity) now to make use of the non-phase-stabilized pulses as briefly alluded to above. According to our method for each pulse with a random CEP, we can calculate the two phase asymmetry parameters, both evaluated in the non-overlapping energy ranges mentioned earlier. We can then plot these two values for every pulse on a 2D coordinate system to obtain the Lissajous-like curve. Because the shots have a random CEP, they have to show a flat distribution over the 2π interval. We can put these 4500 shots in a monotonously changing order, ascending or descending order based on their θ value in their polar representation (after a cartesian to polar conversion). Again, since they have a flat distribution, then we know, each of these points on the 2D plot will have a unique value, the separation in CEP value between them being equal to $2\pi/4500$. This way we have made a connection between the polar angle in the polar representation (each point described by its θ and r values) and the CEP value ($\theta \rightarrow \phi_{\text{CEP}}$ and $r \rightarrow r$). The conversion between the two angles can be handled to some extent similarly to how the time to energy transformation of the TOF data was done. If according to ϕ_{CEP} the histogram is flat, then $\int_0^{2\pi} f(\phi) d\phi = 4500$, where $f(\phi)$ is the distribution of the shots as a function of their CEP, and from this $f(\phi) = 4500/(2\pi)$. We also know that the distribution $g(\theta)$ according to θ contains 4500 shots, too, so by implication $4500/(2\pi) d\phi = g(\theta) d\theta$. Thus we get:

$$\phi_2 - \phi_1 = \frac{2\pi}{4500} \int_{\theta_1}^{\theta_2} g(\theta) d\theta \quad (4.3)$$

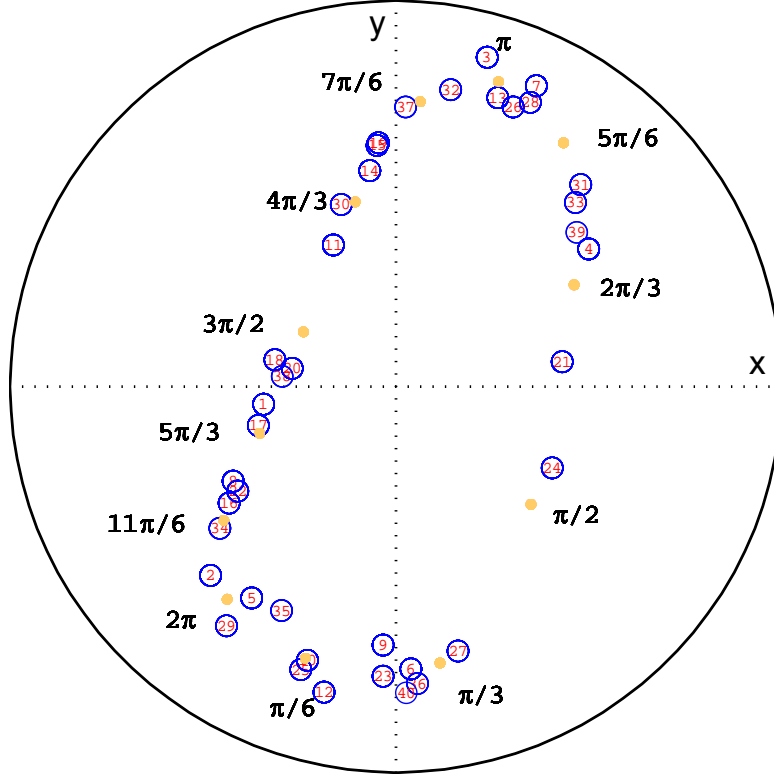


Figure 4.9: Non-phase-stabilized pulses depicted on a parametric plot. The pulses shown here arrived consecutively, with a random CEP and only the first 40 were selected for viewing purposes. Each point has an x and y coordinate, and these are their phase asymmetry parameters calculated for two neighboring energy ranges. The numbers inside the circles correspond to the pulse position in the row of 40 pulses. The dark yellow points are labels indicating the values of the CEP in steps of $\pi/6$. Their relative positions were determined by assuming a flat distribution regarding the CEP of 4500 non-phase-stabilized pulses, while their absolute position was derived through comparison with the results coming from solving the 1 dimensional time-dependent Schrödinger equation.

Therefore, if we have, let's say 10 shots in an interval between $\theta_2 - \theta_1$, so the above integral being equal to 10, then between $\phi_2 - \phi_1$ the CEP difference will be $2\pi/450$. The relative positions of the labels in Fig. 4.9 were obtained also in this manner, that is by grouping $4500/12 = 375$ pulses and the difference in CEP between them being $\pi/6$.

4.5 Precision of the CEP measurement

As we have made efficient use of the non-phase-stabilized pulses in drawing a CEP map for the arriving pulses, without any need for phase-stabilization, we are now able to make important statements about the precision of the CEP measurement, to know the device precision. It has to be reemphasized here that in earlier work by others separation of the

device precision from the total observed precision was not possible. The CEP-fluctuation of phase-stabilization always overshadowed the precision of the CEP measurement, the number of which therefore had been unknown.

Precision, in general characterizes the spread of a measured quantity, while accuracy is the deviation of the measurement from the true value. Therefore, precision in physics quantifies the degree of reproducibility. There are several random variables, noise sources that will lead to an uncertainty in the CEP measurement. Such noises that are added to our measurement system are thermal noise in the electric circuitry, noise from the MCP detectors, oscilloscope. In probability theory and statistics the random variables can be described by a function called Probability Density Function (PDF). The PDF function has two important parameters, which help us describe the variation of our measurement. These parameters are the mean value and the variance of the PDF. The mean gives the location of the distribution, while the spread of the data can be characterized by the variance. The other quantity that is directly linked to the variance is the standard deviation (std), which is simply the positive square root of the variance. Thus, the mean is $\mu = E(X)$, while the std can be calculated through $\sigma = \sqrt{E[(X - \mu)^2]}$, where E denotes the average or expected value of the random variable X .

In most cases noise will exhibit a Normal or Gaussian distribution. In our CEP measurement we carried out the precision analysis by assuming that we have Gaussian distributions of the data for both the radial and the tangential directions on the parametric plot, at a certain CEP location. Out of these two possible directions for the distributions, the tangential spread is of prime interest for us, as this gives the precision of the CEP measurement. It is reasonable to assume that the distributions in the two orthogonal directions had the same standard deviations, and this allowed us to infer the CEP precision from the radial spread. To determine the mean and the standard deviations, we did the following. First, the shots were inserted into bins, that is we selected subsets of 50 out of the 4500 points. These 50 points were neighboring one another based on their polar angle on the plot and this means that the separation between the bins corresponded to an interval of CEP phases of $\pi/45$ ($50 * 2\pi/4500 = \pi/45$). These 90 CEP values, after a comparison with 1 dimensional TDSE calculations, are indicated as blue dots in the enlarged views in Fig. 4.10. The points with the highest asymmetry at the cutoff energy (where y is maximum) define the distinguished CEP settings of $\phi_{\text{CEP}} = 0$ and $\phi_{\text{CEP}} = \pi$. Following the binning of the shots, the mean and the standard deviations were obtained in the boxes of 50 shots along the ellipse-like curve, and the dots were connected to form lines, shown as blue and red lines in the figure, respectively. The area where we can reach the highest precision has been enlarged, and this is located to the right of the main polar plot. It can be expected that the sensitivity of the phase measurement is the highest where

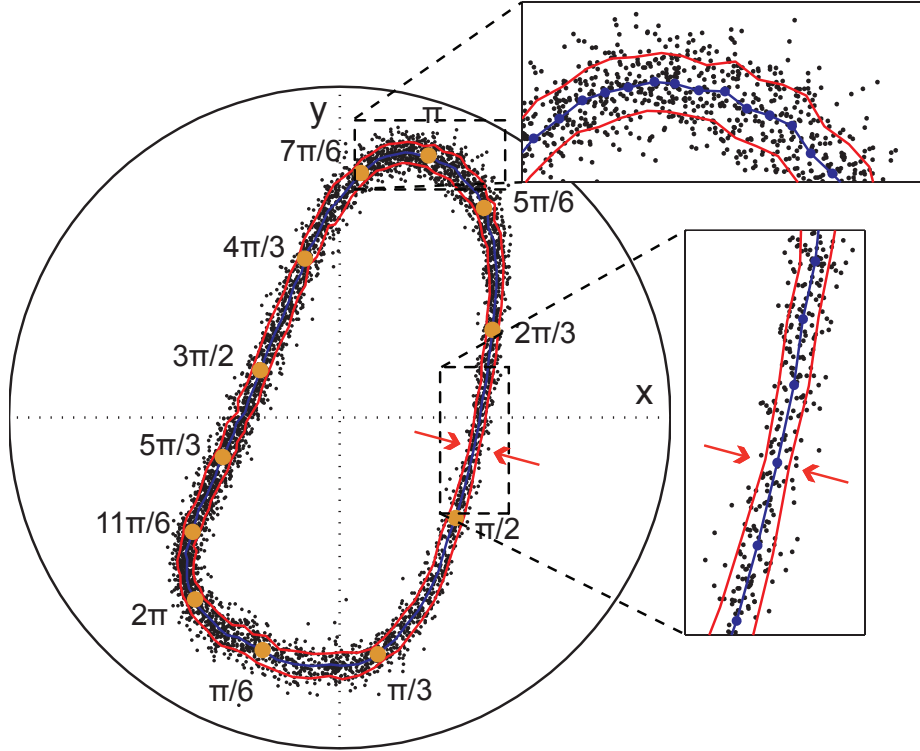


Figure 4.10: Mapping the CEP of non-phase-stabilized consecutive laser pulses. Consecutive single laser shots (black dots) from a non-phase-stabilized laser at 3 kHz repetition rate are depicted on a parametric plot whose axes x and y are the phase asymmetry parameters derived for different energy ranges in the ATI spectra. The CEP of the 4500 measured laser shots varies randomly in a range leading to a distribution along a nearly elliptical curve. Using the random CEP distribution of non-phase-stabilized laser shots, the phase asymmetry was linearized: 90 blue dots (zoomed in view) indicate $\pi/45$ phase intervals. The values of the CEP indicated around the quasi-ellipse (orange dots) were retrieved by 1D TDSE simulations, and these are similar to the hour ticks on a watch (12 points). The blue line connects 90 mean value points of the distribution of all the shots. The red lines show the standard deviation of the measurement. At the operating point of $\text{CEP} = 5\pi/9$, highlighted by red arrows, close to the zero value of phase asymmetry parameter y (highest energy range of the ATI spectra) the measurement precision was evaluated to be $\pi/300$ (std).

the CEP changes the most rapidly, that is when the distance in polar angle on the plot between two CEP values becomes the highest. Indeed, this is the case as can be observed in the magnified area on the right of the polar plot, as the radial spread shrinks to its minimum (for a $\text{CEP} = 5\pi/9$). To verify the assumption of having a Gaussian distribution, we plotted a histogram of the shots, as well as a Gaussian fit (Fig. 4.11) to this data. The distribution was constructed by using shots residing in 7 adjacent small boxes in the area surrounded by the dashed rectangle of Fig. 4.10, close to the zero-crossing of the y parameter. The more shots we choose, the closer the correspondence will become to

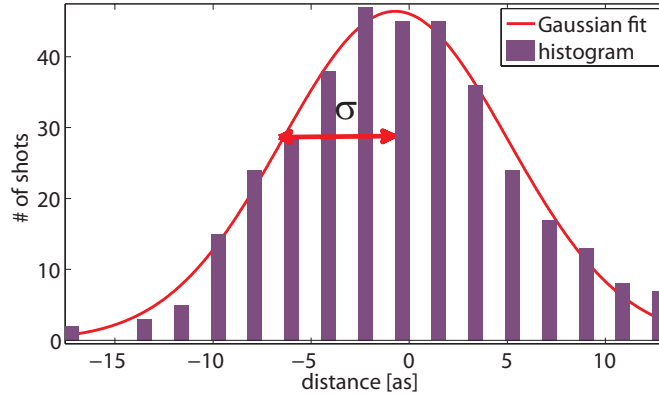


Figure 4.11: Histogram showing the precision as calculated close to the region of highest sensitivity. The shots that make up this plot are contained in 7 bins, the center of this row of bins being close to the zero-crossing of the y phase asymmetry parameter. The precision has been calculated from the distance of the shots from the mean curve, and is expressed in attoseconds.

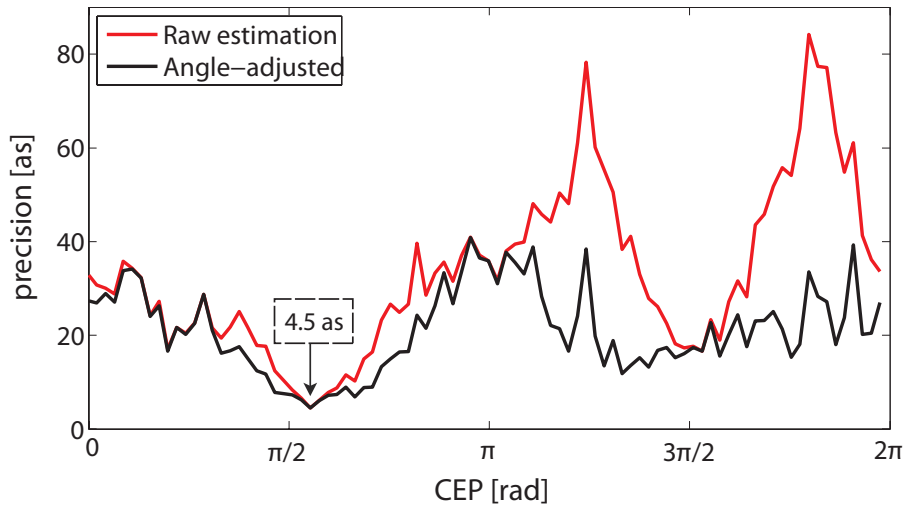


Figure 4.12: Precision as a function of CEP. In the raw estimation (red curve) we applied binning for the shots and the radial and tangential directions in these boxes, each had two components, one being parallel and another one being perpendicular to the line drawn from the center of the polar plot to the center of the box. In contrast to this, the angle-adjusted estimation implemented the case when an angular change resulted only in a CEP change and no radial variation. Therefore, the latter method provided more accurate results.

a real Gaussian bell-shaped curve. It represents essentially the CEP precision for $7 \cdot 50$ shots, as for these 7 bins the computed radial standard deviation was transformed to a tangential one. From this raw analysis, it can already be seen that our precision lies below 10 attoseconds (10 as is $\pi/135$ if 2π is 2.7 fs).

When a phase-stabilized laser is available, and the CEP of every shot has to be

recorded, it is best to operate the phase meter in the region of highest sensitivity, close to a CEP-setting of $5\pi/9$. One can always make sure that the device is working in this range by moving the pair of wedges situated before the entrance window as much as needed to adjust the CEP, and observe at the same time whether the acquired shots have CEPs in the vicinity of highest sensitivity. However, when the task is the measurement of the CEP of a non-phase-stabilized laser, all CEPs will necessarily appear after a while. In this case, knowing the precision for all phase values becomes an important factor. Thus, similarly to the above, for each of the 90 bins we calculated the radial standard deviation, and then transformed this value to get the same parameter, but now in the tangential direction. This quantity, expressed in attoseconds has been plotted in Fig. 4.12. The precision is below 40 attoseconds in the whole interval, and the best sensitivity is reached for a CEP of $5\pi/9$, which amounts to 4.5 as or $\pi/300$. The raw estimation corresponds to the just described method. Both the radial and the tangential directions had two components each, one that is parallel and another that is orthogonal to the line drawn from the center of the Lissajous-plot to the center of the specific bin. This entails that a tangential movement along the ellipse-like distribution is not purely such that only a CEP variation will result, but it involves also a radial change. This problem is completely eliminated in the angle-adjusted calculations, where all data points were subject to a coordinate transformation to get a circular distribution. Along a circle now an angular shift, which is tangential along the circular-shaped curve, will really give only a CEP-change with no radial shift. Therefore, it can more accurately estimate our precision. As can be seen, the deviation between the two applied methods is negligible close to our highest sensitivity, where the radial line going to the center of the bin in both cases is nearly perpendicular to the angular change along the ellipse-like or circular curves.

4.6 Complete characterization of CEP-stabilization

So far, several groups have characterized the phase stability of CEP-stabilized lasers by measuring the relative CEP change with f-to-2f interferometers [96–99]. These measurements were made at acquisition rates far below the laser repetition rates and by averaging over tens to hundreds of shots. In the literature both in-loop and out-of-loop measurements can be found, though strictly speaking only out-of-loop measurements can provide a reliable means for measuring the change of the CEP. An in-loop measurement essentially means that the CEP-drift measurements are carried out with the same interferometer as the one that is used to control the phase, while the out-of-loop technique uses another f-to-2f setup, which is not in the control loop. Thus, the in-loop case only shows the effectiveness of the stabilization electronics [98]. State-of-the-art phase-stabilization in-

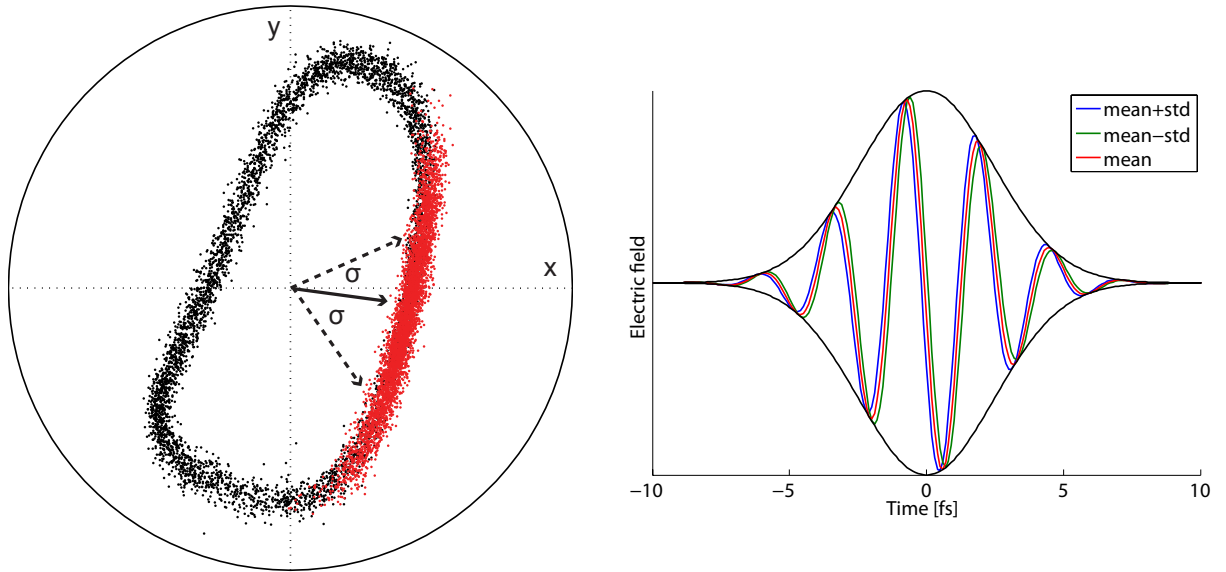


Figure 4.13: Left figure: 4,500 consecutive phase-stabilized (red dots) and non-phase-stabilized (black dots) laser shots in parametric representation. The stabilized shots are distributed around the preset CEP with a standard deviation of $\sigma=278$ mrad, which is indicated by arrows on both sides of the median CEP point. Right figure: waveform of the phase-stabilized pulse corresponding to the median (or mean) CEP setting, as well as the mean+std and mean-std to show the amount of phase-jitter.

stalled for systems similar to the one we also used for our experiments with the phase meter provides a stable CEP with a precision of 50 mrad (standard deviation or std) [71]. Here, the f-to-2f interferometer that sets the CEP on a long time-scale of seconds has been implemented after the hollow-core fiber, as described in chapter 3 of this thesis.

Next, we present the first consecutive single-shot characterization of a stabilized laser using the same method that we described before for non-stabilized lasers, and furthermore we demonstrate superior precision in comparison to established methods. We could carry out this characterization thanks to our new evaluation method that could decouple the phase fluctuations of the laser from the precision of the apparatus. We have to note at this point that the stereo-ATI technique, beyond its ability to measure the CEP, has been already applied to stabilize the phase [82], as well. However, again there they averaged over many shots (300 pulses) due to the multi-shot nature of the device. The red points obtained through our measurements as shown in Fig. 4.13 indicate 4,500 consecutive laser shots recorded now with the laser being CEP-stabilized to a nominal value of $5\pi/9$. As both our measurement fluctuation and the distribution of the stabilized shots is nearly Gaussian (Fig. 4.11 and Fig. 4.15, respectively), with a crude approximation the ratio of measurement precision over laser stability (i.e. precision of phase-stabilization) equals the ratio of width over length of the ‘stripe’ made by the red dots. Even with our state-of-the-art phase-stabilization scheme, the standard deviation of the CEP of the stabilized

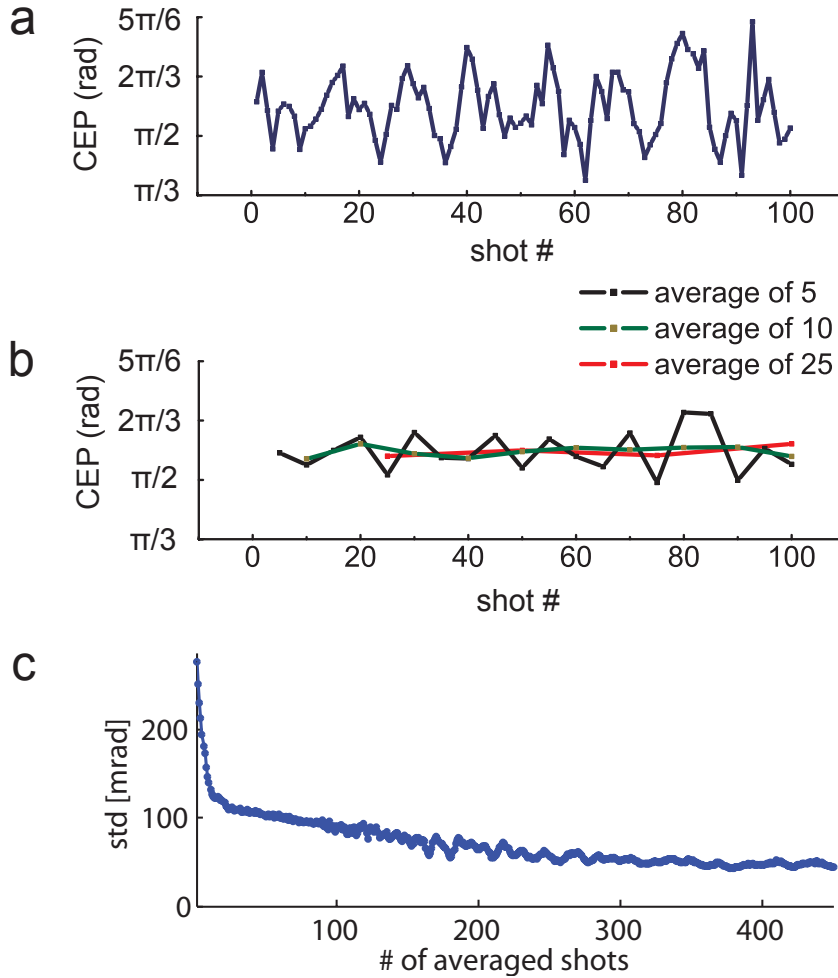


Figure 4.14: a.) Shot-to-shot evolution of the CEP of 100 consecutive phase-stabilized laser shots. b.) Same evolution, but with the CEP values of 5/10/25 shots being averaged. c.) Standard deviation of the shots with averaging over 1 to 450 shots. Concerning c.) one can see that there is a pronounced difference between multi-shot and single-shot operation in terms of the observed standard deviation.

shots was 278 mrad, which is indicated with dashed lines with an arrowhead attached to them. That is more than 25 times worse than our measurement precision at that CEP setting and it is also worse than reported in [71]. We will see that the reason for this seemingly insufficiently low value for practical experiments lies in the fact that our standard deviation (std) was derived from the CEP values of all individual shots, whereas in other measurements the CEP values are averaged over several shots. To visualize the level of phase fluctuation of our system the plot on the right hand side in Fig. 4.13 depicts the corresponding waveforms with CEP values being equal to the mean value, mean value + std and mean value - std. We can state that the phase jitter is low, but by far not negligible, especially for strong-field experiments, such as attosecond pump-probe measurements, where stability is a critical issue.

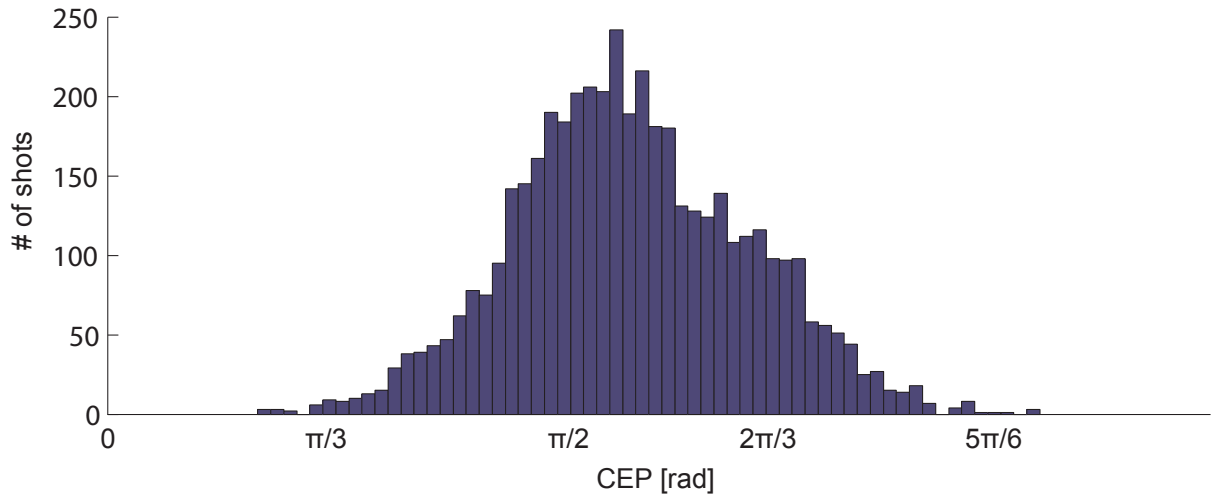


Figure 4.15: Histogram of phase-stabilized pulses. This histogram shows the CEP distribution of 4,500 shots of a phase-stabilized laser. The nominal CEP setting of the phase-stabilization corresponded to the same value as in Fig. 4.13 and Fig. 4.14.

We also investigated the shot-to-shot evolution of the CEP over 100 consecutive stabilized shots, which is shown in Fig. 4.14. Moreover, here we plotted the case when averaging over some shots occurs, which shows what would happen for a multi-shot measurement approaching the single-shot measurement capabilities. This evolution of the phase basically more and more flattens out when the number of shots used for averaging the CEP increases, indicating that the single-shot measurement provides new insight into the CEP evolution of a laser system. In addition, the bottom graph in the group of figures demonstrates it in more detail how dramatically the observed standard deviation changes when the number of pulses that are taken into account for its determination continually decrease. Towards single-shot operation, the standard deviation steeply rises, while for a high number of integrated pulses it reaches a relatively constant value of around 48 mrad. Quite remarkably, this precision value lies very close to the standard deviation for the phase jitter that was published in an attosecond streaking measurement of the shortest attosecond pulse to date [71], which utilized a laser setup that was very similar to the one we used for our measurements.

For phase-stabilized pulses another interesting aspect to look at is the type of distribution for the CEP. To this end, we created a histogram regarding the CEPs for the 4,500 shots that we measured, and this can be seen in Fig. 4.15. It exhibits a close-to Gaussian distribution, as one could expect. The phase-stabilization operated at the same set-value as before in Fig. 4.13 and Fig. 4.14.

Another intriguing question that can arise is the sensitivity of the f-to-2f slow-loop interferometer to the energy fluctuation. This effect has already been studied experimentally [97] using two interferometers, where they created a deliberate energy modulation

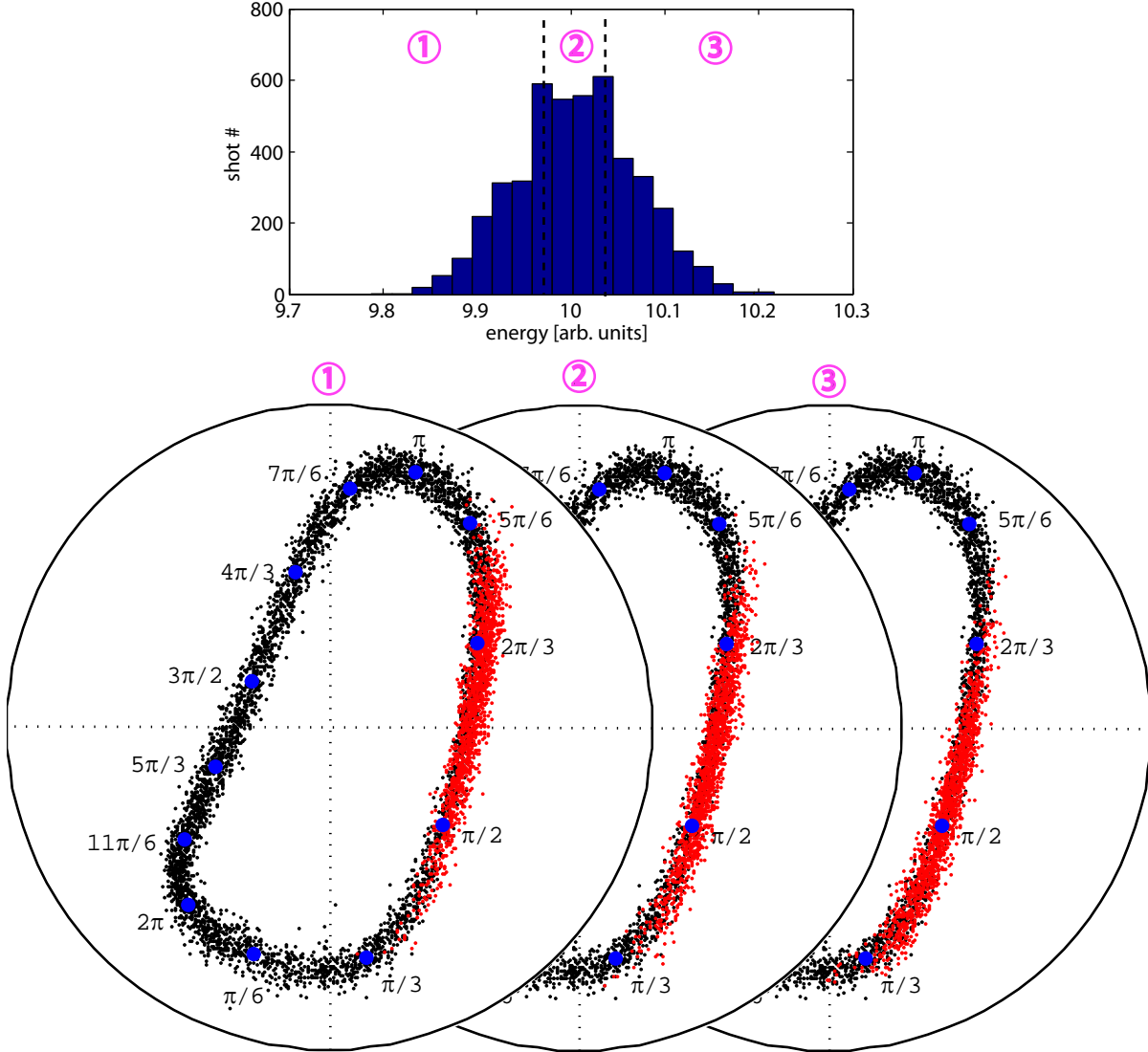


Figure 4.16: Sensitivity of the slow-loop to the energy. The figure on the top is the distribution of phase-stabilized shots based on their energy. The energy fluctuation was 0.6% (standard deviation/mean), which can be mainly attributed to the pump laser’s energy instability. The three plots below the histogram for the energy show the phase-stabilized shots in a parametric representation. These separate graphs depict shots that possess energies, which fall into one of the three energy ranges indicated by numbers 1-3.

only for the in-loop f-to-2f interferometer, while the out-of-loop interferometer measured the change of the phase. The phase-energy coupling coefficient was determined this way, which was equal to 160 mrad/1%. On the other hand using the phase meter measuring such a sensitivity of the slow-loop has not been performed yet. Our measurements shown in Fig. 4.16 constitute the first preliminary results towards such characterization. We plotted here the distribution of the shots in terms of their energy, as well as the parametric representation of phase-stabilized shots with energies belonging to one of the three

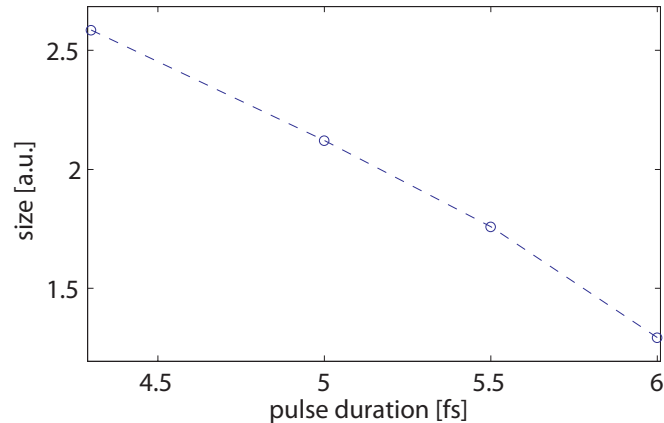


Figure 4.17: Sensitivity of the phase meter to the pulse duration. This property is characterized by the size variation of the parametric plot when the pulse duration is changed. Calculations were performed using a 1D TDSE code for 4 pulse durations, and these have been indicated by dots on the curve.

intervals denoted by the numbers 1-3. The mean CEP value for phase-stabilized shots coming from energy range 1 was 1.919 rad, in case of range 2 it was 1.768 rad, while for range 3 the value was 1.605 rad. Therefore, between the two extreme energy regions the resultant CEP difference was approximately 0.3 rad. This represents an upper limit to the amount of energy sensitivity of the slow-loop. What we have not accounted for here, and this is a subject for further future theoretical and experimental studies, is the sensitivity of the phase meter to the energy change. Only a radial movement was observable so far, measured for the non-phase-stabilized shots, but there can also be a radial shift. As a result, it is not known yet how much of the energy-induced CEP shift can be attributed to the energy sensitivity of the slow-loop and how much the contribution of the phase meter is.

4.7 Dispersion-free pulse duration measurement

Until now we have presented a novel way for the characterization of both non-phase-stabilized and phase-stabilized pulses in terms of their CEP. To fully describe a few-cycle pulse, not only its CEP is of crucial importance, but naturally its pulse duration has to be known, too. In this section of the thesis, we demonstrate in simulations, as well as provide preliminary experimental data, that a phase meter is a more versatile device: it can measure the pulse duration, as well. This further capability and its ability to measure the CEP will make it a multi-meter apparatus in few-cycle optics.

There are several existing techniques for pulse duration measurement. Such methods, referred to with their abbreviations, are FROG (Frequency Resolved Optical Gating)

[100], SPIDER (Spectral Interferometry for Direct Electric Field Reconstruction) [101], second- and third-order autocorrelation (as presented in chapter 3). The former two techniques became dominant in the field, since through using them one can retrieve not only the duration, but also the spectral phase. The latter essentially tells us why the pulse is longer than its transform-limited (TL) duration, and helps us come up with ways to compensate for the nonzero spectral phase to approach the pulse' TL-limit. For the ever shorter pulse durations generated in the laboratories, there is a pressing need for a method that can measure even the ultimate limit embodied by a single-cycle pulse [21, 71]. In all current devices the factors that hinder us in measuring these very short events are essentially the bandwidth-limit of the nonlinear conversion in the crystal, and the dispersion introduced during the splitting of the pulse. The shortest pulse duration that could be measured with these techniques was achieved with an SHG-FROG device, and the pulse length was 4.5 fs [102]. We have to mention here that there exists, in fact already the tool for the characterization of few-cycle, even single-cycle pulses, and it is essentially the streaking measurement [7]. For this a shorter pulse, an attosecond XUV pulse, is used to sample the waveform [8], the shortest pulse in the NIR having a duration of 3.3 fs. This lets one precisely draw the time-evolution of the electrical field; this technique, however needs phase-stabilization, does not work single-shot, and therefore it requires the best possible stability from both the laser and the surrounding environment for a usual measurement time of >10 mins (per waveform characterization).

From the phase-scan of Fig. 4.8, we can already establish that while the pulse duration was varied due to a scan of the CEP over a range of several times 2π , the phase asymmetry was changing, as well. In other words, our phase meter is sensitive to the pulse duration. Most interestingly, as opposed to other conventional methods, which were enlisted above, the physical observable, that is here the phase asymmetry parameter is increasing with a decreasing pulse duration. Our measurement device thus becomes more sensitive in case of a single-cycle pulse. The phase effect ceases to be of appreciable magnitude above around 7 fs, therefore the concept of using stereo-ATI lends itself perfectly to the characterization of very short pulses. To theoretically corroborate these findings, in Fig. 4.17 we show calculations (by G. G. Paulus) of the size of the parametric plots corresponding to different pulse durations. It is already visible here that the size of the ellipse-like curve changes as a function of pulse duration, and there is an inverse relationship between the two, that is a shorter duration will result in an extended size for the curve. They were obtained by solving the 1 dimensional time-dependent Schrödinger equation (1D-TDSE), and although the thus obtained results already show a clear dependency on the pulse duration, in the future more thorough 3D calculations will be carried out.

For the calibration of our measurements, which were presented in the preceding sec-

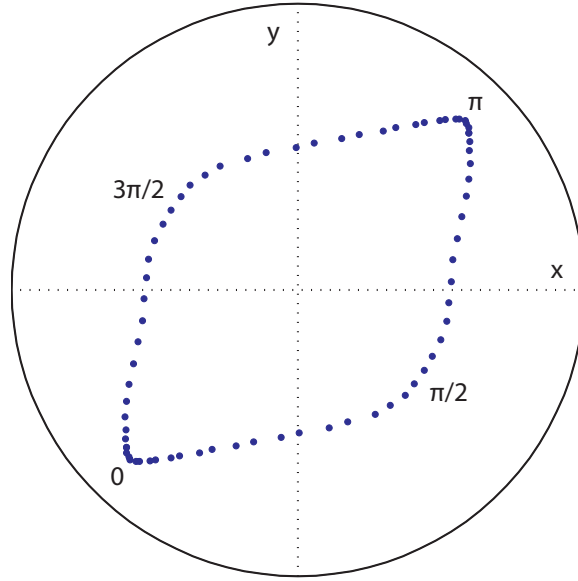


Figure 4.18: Parametric representation of the CEP obtained from theory. Concerning the calculations, 1D-TDSE was solved and from the spectra of the electrons the x any y phase asymmetry parameters were derived for CEP values between 0 and 2π , with a step size of 5 deg or $\pi/36$. It served as our reference plot for the calibration of our measurements.

tions, similar theoretical calculations were needed (for a duration of 4.1 fs with integration as given by our analysis of the experimental data). The curve that was provided by theory dictated the direction of change of the CEP, as well, so it told us if the CEP was increasing in the clock-wise or the counter-clock-wise direction. The orientation and the general shape of the Lissajous-like experimental plot have been relatively well reproduced by theory, as plotted in Fig. 4.18. Understandably, 3D-TDSE calculations could give a better match, and taking into consideration intensity averaging (or volume effect, see 2.3.2) due to the spatial profile of the pulse could also help. Other plots where the effect of no intensity averaging due to our 1D model is observable are in Fig. 2.2. Some dips in the TOF spectra are present, which are washed out in the experimental ones owing to the intensity variation in a real pulse having some spatial profile.

Prof. Chii-Dong Lin and Zhangjin Chen, Kansas State University carried out thorough simulations so that we can gain more insight into our experiments, specifically to find out exactly what CEP values we had along our structure that is represented by all the laser shots on a parametric plot. Their simulations were based on the quantitative rescattering (QRS) theory [103] developed by them, which takes into account 3D effects. Moreover, this method permits the retrieval of not only the CEP, but also the pulse intensity and duration, following a comparison with experimental results. Both the experimentally obtained shots and the theoretically calculated curve in a parametric representation, as

well as the location of 4 CEP values are shown in Fig. 4.19. The match between theory and experiment is excellent. These results led to the determination of the pulse parameters: duration yielded 4.7 fs, while the peak intensity was $1.4 \times 10^{14} \text{ W cm}^{-2}$, assuming a Gaussian temporal and spatial profile. We see that we underestimated before the pulse duration and the intensity. The outcome of our previous analysis not being contradictory to these newest results can be attributed to the following: for a pulse with a Gaussian profile the central peak region contributes only by a small amount to the total ATI spectrum, while the area corresponding to lower intensities is large, and therefore its effect will be more significant.

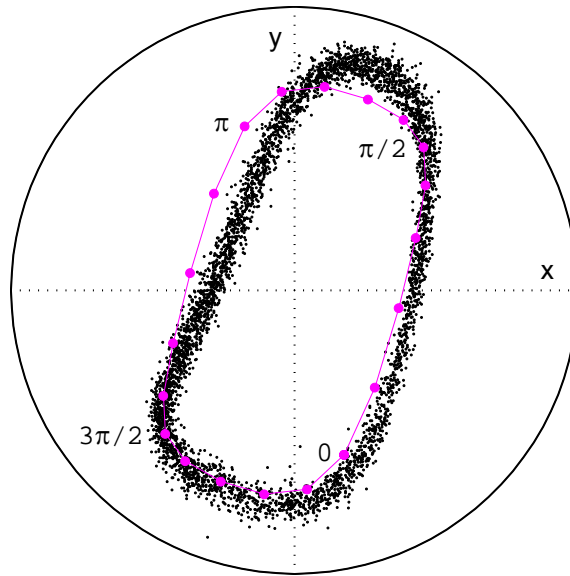


Figure 4.19: Advanced theoretical calculations (purple line and dots), giving a very good match with experimental results (black dots). Quantitative rescattering theory was applied, and 3D volume effects were considered that could allow us to retrieve all the pulse parameters: the CEP, as well as the pulse peak intensity, $1.4 \times 10^{14} \text{ W cm}^{-2}$ and duration, 4.7 fs. The purple theoretical CEP dots have a distance of 0.1 rad, and 4 CEP values have been selected, their labels appearing to the left from the respective CEP location.

Experimentally, pulse duration measurement with the phase meter can be implemented the following way. As a first step, it is important to obtain the averaged TOF spectra of 4500 shots. The result of such an averaging can be seen in Fig. 4.20. The $10U_p$ cut-off has been indicated, too. This cut-off is defined here as the energy where the intensity drops to 90% of the peak TOF intensity. It is a parameter that linearly depends on the peak intensity of the pulse, and throughout the pulse duration measurement it should be kept constant so we can remain in the same operation regime regarding the intensity. As a matter of fact, knowing its absolute position along the energy axis, it allows us to deduce what intensity we have during the measurement. To keep the peak intensity the

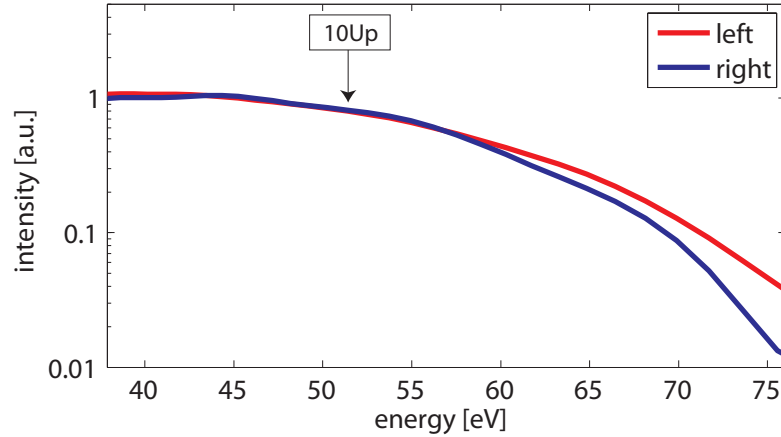


Figure 4.20: Averaged TOF spectrum for each MCPs. The averaging was done for all 4500 shots so that the position of the $10U_p$ cut-off can be determined. The signals from the two MCPs are nearly identical, because before the measurement we adjusted the amplification in each arm accordingly. By keeping the peak intensity of the laser the same, that is the location of the $10U_p$ cut-off, we can always stay in the same regime of operation. This will in turn allow us to use the non-phase-stabilized pulses, together with the calculations to measure the pulse duration of our laser pulse. The position of the cut-off permits the exact determination of the peak intensity, which in our measurement was $8 \times 10^{13} \text{ W cm}^{-2}$.

same, a neutral-density (ND) filter can be applied in reflectance mode. This allows one to avoid dispersion, which otherwise would cause the pulse to get stretched, and to obtain a different CEP, in case the beam propagated through the filter. Actually whenever the pulse duration changes, such an adjustment of the intensity by a movement of the ND filter is necessary, and this has to be done by a simultaneous observation of multi-shot averaged TOF spectra. A subsequent step is then the acquisition of single-shot data, and the drawing of the parametric plot. Finally, a comparison between the theoretically obtained parametric plot and the experimental one will give the pulse duration. Effectively, this last step is based on the fact that the length of the radius of the parametric plot is indicative of the pulse duration.

4.8 Summary

In this chapter we presented a robust single-shot CEP measurement technique, which obviates the need for phase stabilization. The CEP is measured without any ambiguity regarding the phase, which is a consequence of a novel evaluation method of ATI spectra. Our precision can be as high as $\pi/300$ at an optimum measurement point.

The maximum acquisition rate of the apparatus is several times higher than the repetition rate of amplified few-cycle sources available at present, and only a small fraction of

typically delivered pulse energies is necessary for a non-invasive CEP measurement. These unique features of the apparatus make it extremely versatile. As a direct application, the CEP of each laser pulse can be measured with a precision of more than 25 times higher than with state-of-the-art stabilization techniques. High-order harmonic generation, ATI or terahertz emission are just a few of those phenomena that are directly governed by the electromagnetic field and actively studied with few-cycle pulses. With our single-shot measurement technique, experiments with non-phase-stabilized lasers can now be carried out and by simple CEP tagging, we can fully determine the dependence of the physical phenomena on all values of the CEP and with ultra-high precision. The capability of our apparatus is not limited to CEP measurements. Our measurement technique can also be used for pulse duration measurement. The polar angle of a measurement point on the parametric plot gives the CEP and its radius provides a measure of the pulse duration. Unlike conventional pulse duration measurement techniques, this method is dispersion-free and unlimited in bandwidth, and its accuracy is increasing with shorter durations. As the ATI cutoff is a direct measure of the pulse intensity, we will be able to measure the three most important parameters of few-cycle laser pulses with our apparatus in single shot: CEP, pulse duration and intensity.

Chapter 5

HHG with broadband two-color waveforms

5.1 Introduction

High-harmonic generation (HHG) for obtaining isolated attosecond pulses has been carried out so far with near-infrared (NIR) few-cycle pulses with a bandwidth of one octave [21]. Throughout this thesis such NIR pulses are generated, measured, and used to reach such photon energies, with which it is possible to electronically excite atoms and molecules. This high energy radiation in the time-domain can correspond to a duration of as short as 80 as [71], provided appropriate dispersion-compensation as well as filtering in the XUV are realized, as explained in chapter 2. The question remains: what further benefits would NIR pulses with bandwidth spanning more than one octave bring? This chapter introduces the possibility of extending our spectrum further towards lower wavelengths, together with the control of the dispersion and CEP to tailor the pulse shape, i.e. create new waveforms. These pulses will in turn drastically change the generated harmonic structure. This waveform shaping is achieved by efficiently frequency-doubling a part of our NIR spectrum, followed by an overlap in space and time of this newly created component with the original pulse. We have dispersion-compensation over the whole spectrum of the original pulse, and control over the group-delay (GD) of the new frequency components.

In HHG an attosecond pulse train can be naturally produced since during the time evolution of the relatively easily available multi-cycle field attosecond pulses are repetitively produced in every half-cycle [65, 66, 104]. Introducing substantial field variation with the help of a few-cycle pulse, combined with a suitable energy filtering will result in the generation of an isolated attosecond pulse [27]. Another approach to reaching this effect has been the addition of a weak second-harmonic field to the fundamental wave [105, 106].

The consequences of having a new field are far-reaching. We can infer from equations 2.3 in chapter 2 that a small perturbation in the field during the tunnel-ionization step will cause huge changes in the ionization, thus the high-harmonic generation efficiency can be controlled. After the electron is born, it follows a trajectory under the influence of the electrical field. Therefore, the shape of the field not only determines how many electrons are born (ionization), but also how much energy they acquire from the field. Their recombination with the parent ion will create XUV photons, and therefore the energy, the yield and the chirp of the photons will be altered. The parameters that will induce a change in the shape of the electrical field are the polarizations, the frequencies, the relative intensities and the relative phase of the two fields. Conventionally, this method of frequency-doubling a narrow spectrum of a multi-cycle pulse fell into the category of two-color experiments. Here they indeed used two colors, which are harmonics of each other. It has been studied extensively both theoretically [105, 107–117] and experimentally [94, 106, 118–128] since around the time of the first HHG experiments with a single color [48, 65]. At the beginning most of the experiments [129–131] were conducted in the multi-photon ($\gamma > 1$) regime with long pulses (100 ps to 15 ns). Two-color phase-control was carried out in ATI to change the total electron yield [131], relative height of ATI peaks [129], the spectra and angular distribution of photo-electron emission [126, 129, 131, 132]. In HHG with a one-color pulse odd harmonics of the fundamental are produced (as explained in 2.4 of chapter 2). Superposition of two harmonics results in a breaking of the symmetry between consecutive half-cycles, so the field will no longer be equal in magnitude just opposite in sign in consecutive half-cycles. Even harmonics can thus be observed [126], and as a function of time-delay between the two pulses a modulation will appear [128], the same HHG structure appearing after one period of change. The period of this modulation corresponds to π since a time-delay change equal to the period of the second-harmonic will give the same relationship in phase between the two added-up pulses (assuming the second-harmonic is long). A different periodicity is expected in the multiphoton regime [133]. The exploration of this technique followed two directions. One avenue of research was concerned with increasing the yield of the harmonics. Due to the addition of the second-harmonic it became possible to enhance the field in one of the half-cycles, which translated to an increased ionization, higher XUV yield [111, 123, 125, 127]. Perpendicular polarization of the two fields was shown to give conversion efficiencies as high as 10^{-4} [123], albeit only for low-order harmonics [127]. The other direction of investigation, both theoretical [105, 108, 109, 112, 113, 117, 122] and experimental [106], proved that one can get into the isolated attosecond pulse generation regime with multi-cycle driver fields using a weak second-harmonic pulse. The difference in amplitude in the successive half-cycles will create two cut-offs, one lying higher in energy, but of low intensity (upper

cut-off), and another one located in the low energy region, but with high intensity (lower cut-off). The intensity for these cut-offs is a direct consequence of having an enlarged or a suppressed field strength at the time of ionization [105, 113, 120, 121, 124]. Two attosecond pulse trains with different energies and intensities will result, each with a periodicity of a full-cycle [119]. The necessary field variation for generating an isolated pulse in case of HHG with fundamental only, the single pulse condition requiring variations in the peak energies of consecutive half-cycle XUV bursts, is provided by the few-cycle pulse. This stringent requirement on the driver pulse duration is greatly relaxed in a two-color HHG by a factor of two with the second-harmonic added [105], and a factor of 4 when a subharmonic (1600 nm if the fundamental is at 800 nm) is used [112]. By high-pass filtering the HHG radiation in a range, where the harmonic structure disappears and only a continuum exists, it is possible to generate a single attosecond pulse. This relies on the modification of the kinetic energies of the recolliding electrons during their time spent in the continuum. The other mechanism that plays a role, as discussed above is ionization. In consecutive half-cycles the ionization rate will differ, which will lead to a filtered-out XUV spectrum with low yield [105]. However, essentially this ionization gating can also be altered in a beneficial way simply with the help of another time-delay so that the harmonic yield will not suffer [113].

Combining the powerful technique of adding two harmonic pulses together and polarization-gating (PG) that limits the time when effective recombination of the electron can occur is the essence of Double-Optical Gating (DOG) [134]. It is a very interesting method for multi-cycle laser pulses, because it improves on both techniques if they are used alone. Applying only PG (see also section 2.2.2 of chapter 2) requires 5 fs pulses in order to avoid strong ionization to happen for half-cycles other than the one that generates the highest energy HHG radiation. Outside the gate-window (where mainly linear polarization dominates) the circularly-polarized pulses strongly ionize the medium, which lowers the generated HHG intensity for pulses longer than two-cycles. Adding a second-harmonic field to PG can suppress every other half-cycle of a multi-cycle (12 fs long) pulse and the same ionization probability can be thus maintained as when a 5 fs pulse is employed. Moreover, it was experimentally found that the width of the continuum will be larger with DOG than when only the fundamental and its SH are added up [106].

When two-cycle pulses are available, it was shown in theory [135] that adding an SH field can further broaden the width of the already present HHG continuum. This broadening will happen for some specific CEP and time-delays between the two harmonic laser pulses. We will illustrate the mechanisms that play a role in the next section through simulations by assuming a 5 fs fundamental pulse. Experimentally such broadening was shown only for relatively long pulses of 7 fs [118], with only the fast-loop running for the

phase-stabilization, so the CEP could not be controlled and maintained for longer periods of time.

Below in section 5.4 we will demonstrate waveform-synthesis and its implications for HHG that was achieved by using our unique fundamental pulse of a near single-cycle duration combined with a second-harmonic pulse, together with control over the waveform. For some CEP values and time-delays between the fundamental and the SH our detailed analysis that we reached by performing scans over these two parameters will reveal new HHG features that will be discussed in this chapter. In our experiments as a first step we carried out HHG with fundamental only, which is a well-characterized regime, and in a controlled way (by keeping the CEP-stabilization in operation) we then switched to HHG with our added-up pulses. Our photon energies in our work lie between 70-150 eV, as opposed to earlier investigations that were conducted below this energy range.

5.2 Control of electron trajectories

Two-color-based waveform synthesis opens up the possibility of controlling a number of parameters of our generated attosecond pulses. In this section we will look at the underlying physics in more detail from a theoretical point of view. Through some simplified cases we can cast light onto the basic mechanisms that play a role in such an experiment. In our experiments, as it will be discussed, two effects will always be present: due to the addition of a second-harmonic field there will be a change of ionization and a larger variation of the energy peaks of the XUV bursts in successive half-cycles as compared to the HHG with the fundamental only. The two are intertwined, but in theory we can see their individual contributions to the observed measurement.

The goal of our theoretical analysis here is to show that with the addition of an SH field we can achieve broadening of the continuum part of HHG, which is a prerequisite for shorter isolated attosecond pulse generation. The continuum is set by the difference between the XUV burst with the highest energy and the next highest one in a neighboring half-cycle. Constructive and destructive interference can occur on a sub-cycle time-scale by superimposing an SH field onto the fundamental, and depending on the time-delay we can expect to see different total electric fields. As a result we analyzed the effect of a SH field by assuming different time-delays, pulse durations and relative amplitudes for the respective fields. To create a fair basis of comparison for the different cases (fundamental only, added-up waves for various time-delays) we kept the cut-off energy at a certain value, which was 100 eV. Naturally, through such waveform-synthesis the waveform can get distorted in such a way that the cut-off will shift to higher energies [112]. With a higher cut-off, however, we will automatically get a broadening of the continuum, and

since the same end-result can be achieved by simply cranking up the intensity of the fundamental only, without having the SH field, we avoided this situation by adjusting the peak of the superimposed electric field. We can easily enlighten this the following way. As we know, the three-step model [42] for obtaining the cut-off energy of a HHG radiation can also be applied for few-cycle pulses. For short pulses, for the electric field in the cut-off law formula 2.15, where the electric field dependence is through equation 2.2, the peak electric field in each half-cycle has to be substituted and thus one can derive the half-cycle cut-off energies. If we have a E_{n+1}/E_n ratio between the highest peak (E_n) and the next highest peak (E_{n+1}) in the next half-cycle, the width of the continuum will be proportional to $(1 - E_{n+1}/E_n)^2 E_n^2$. By increasing the intensity of the fundamental only, we see that the continuum will broaden accordingly, with a quadratic dependence on the electric field strength. In a similar manner, going up in cut-off energy and as a consequence shortening the attosecond pulse duration is the goal of using a higher driving wavelength for the laser [60]. This can also be readily seen from the three-step model of HHG, which predicts a cut-off energy that scales with the driver wavelength squared.

The simulation was performed by solving the trajectory equation 2.10 numerically, which code was developed by the author of this dissertation. The vector-potential term was obtained from the sum of two fields, the fundamental (at 780 nm) and its second-harmonic (at 780/2=390 nm). Thus the total electric field was:

$$E_{total}(t) = E_1 e^{-2\ln 2 t^2 / \tau_\omega^2} \cos(\omega t + \phi_0) + \eta E_1 e^{-2\ln 2 t^2 / \tau_{2\omega}^2} \cos(2\omega t + \Delta t), \quad (5.1)$$

where E_1 is the peak electric field of the fundamental, τ is the FWHM pulse duration, ϕ_0 is the CEP of the fundamental, η is the amplitude ratio between the two harmonic laser fields and Δt is the time-delay between the two pulses. The result of our calculations can be seen in Fig. 5.1, where the alignments of the fields have been depicted, as well as the total E-field and the XUV radiation's energy that is created, and the latter is shown here as a function of the birth time of the electrons that recombine later with the parent ion. The pulse duration of the fundamental was 5 fs, the CEP being equal to 0, the peak intensity of the fundamental $4.1 \times 10^{14} \text{ W cm}^{-2}$, while the second-harmonic electric field was 5 times lower than that of the fundamental, the pulse duration of the SH being also 5 fs. We distinguish two pure cases in our calculation results: (i) one in which a significant change of the peak E-field in each half-cycle exists, which we call Amplitude Modulation or AM ($\Delta t = 0$), and (ii) another where the effective wavelength varies on a sub-cycle time-scale, and it is designated here as Frequency Modulation or FM ($\Delta t = 0.37\text{fs}$). By observing the last plot in the figure we can state that in both cases a broadening of the continuum results. In comparison to HHG with fundamental only, during AM, this bandwidth increase amounts approximately to 8 eV, while for FM it is

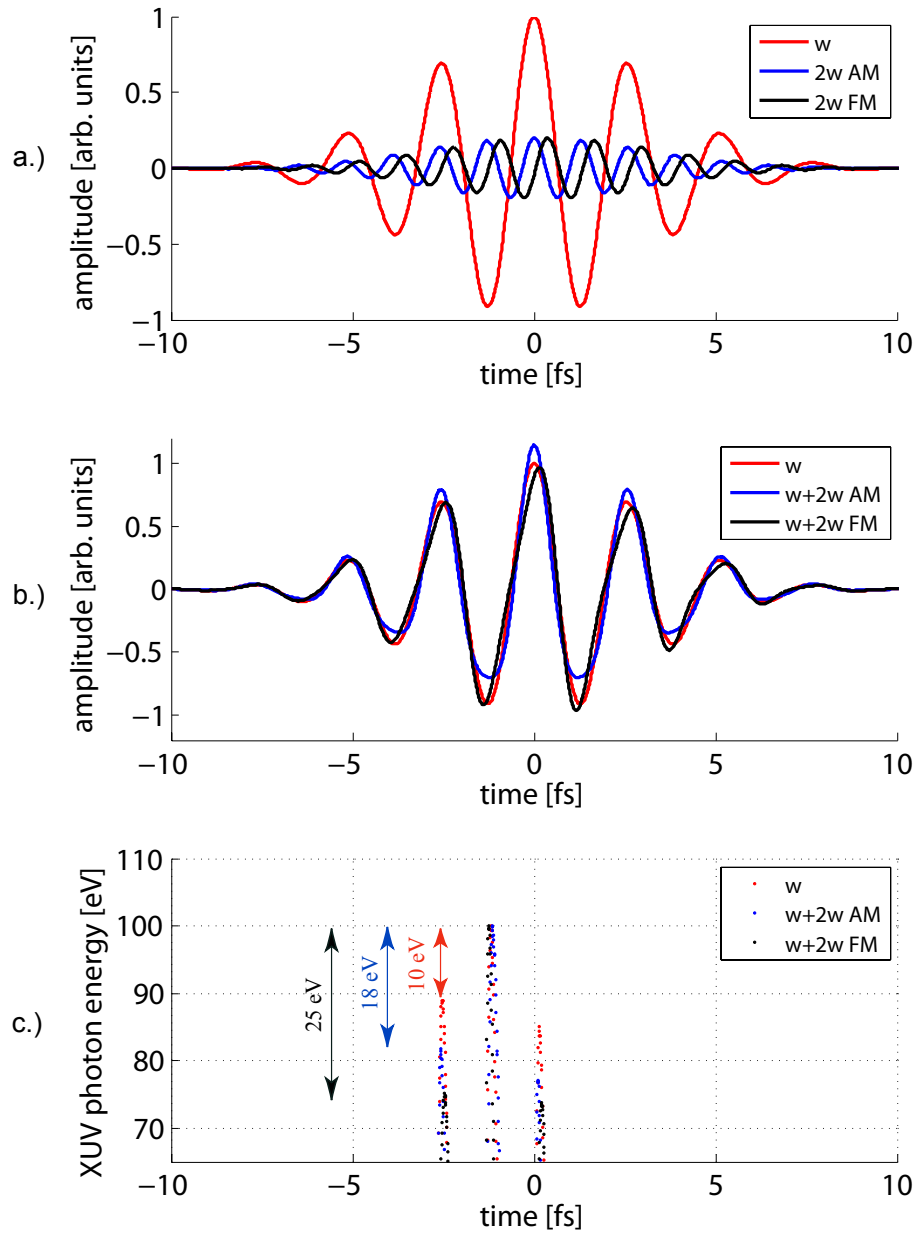


Figure 5.1: a.): electric fields of a 5 fs fundamental and a 5 fs second-harmonic field for two time-delay settings. The intensity ratio between the harmonic fields was 4%. AM stands for amplitude-, FM for frequency-modulation. b.): superimposed fields for AM and FM cases. During AM large variations exist from one half-cycle to the next, while for FM the wavelength changes on a similar time-scale. c.): the three most energetic XUV bursts due to recollisions of the electrons in each half-cycle, plotted as a function of birth time for the electrons. They were obtained through classical trajectory calculations.

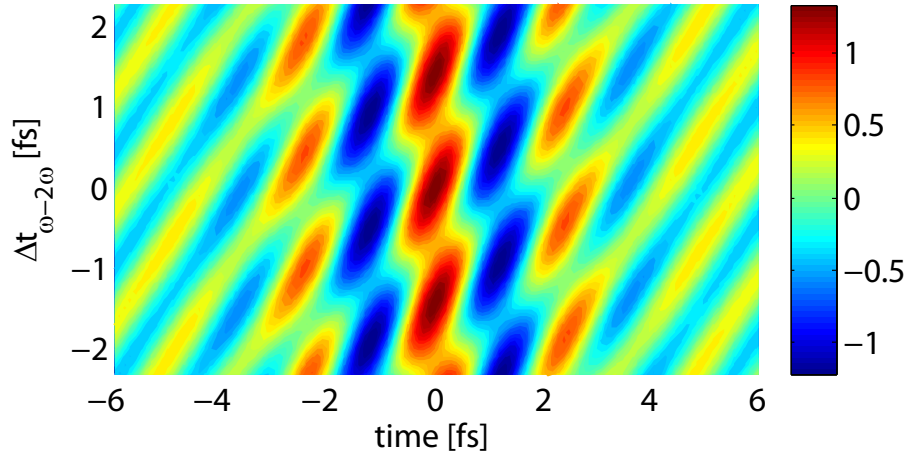


Figure 5.2: Time-delay scan for the generated waveform. The electrical field of a waveform has been plotted that is a superposition of a fundamental at 760 nm and an SH at 430 nm. Time-delay of the y axis indicates that a scan of this parameter is performed, identically as how it is done in the HHG experiment that is to be presented later. A periodicity of 1.4 fs is observable.

about 15 eV. Another important aspect that favors the FM case is the HHG yield. The photon number or the yield is connected to the ionization, and for FM this value is as high as for HHG with the fundamental only (since the electric field peaks for the two cases are nearly the same). Therefore in this case there is no trade-off between the bandwidth increase and the XUV photon flux, in strong contrast to AM, where at the birth time for the electrons that will recollide with the highest energy, the electric field will get suppressed, thus the ionization will lower considerably. These conditions are conducive to the generation of short attosecond pulses with a low intensity. FM will allow one to keep the XUV yield high, and at the same time the continuum will widen. On the other hand, for AM if we had not rescaled the peak intensity of the total field to keep the cut-off at 100 eV, because of the increased peak intensity in one half-cycle the cut-off would be pushed out to high energies, albeit with low associated XUV intensity. We will show such an experimental case later. Experimentally, by changing the time-delay, we can switch between the two cases, with a mixture existing for the intermediate time-delays. Since we worked with a detuned second-harmonic (so we could maximize the ratio η), which caused a small variation of the alignment of the fields in consecutive half-cycles, the total measured spectrum was the result of a mixture of the two cases.

We were furthermore interested in learning more about the periodicity of HHG that we could expect. To this end, we added up two fields with central wavelengths of 760 nm and 430 nm, in accordance with the central wavelengths of the harmonic fields shown in Fig. 5.3, and varied their time-separation, i.e. their time-delay (Δt). The resultant waveform for CEP=0 case, assuming 3.3 fs fundamental and from an experimental point

of view a more realistic SH pulse of 30 fs is shown in Fig. 5.2. The SH pulse duration did not play a role regarding the outcome of HHG, because the effects occurred on a cycle and sub-cycle time-scale. We can see that the periodicity in Fig. 5.2 is 1.4 fs, which means that after such a time-delay we will measure the same HHG spectrum. Essentially, this information will allow us to calibrate our HHG measurements (convert from angle to time), where the time-delay is being introduced by the angular-tuning of the time-plate (a birefringent crystal).

5.3 Analysis of the collinear setup

High-harmonic generation (HHG) with two-color pulses can be realized mainly according to two schemes. One setup splits the pulse into two, sends each of the resultant pulse replicas into the two arms of a dichroic interferometer [119, 136], where the two colors are manipulated in time, followed by a recombination of the two pulses and eventually HHG by the two-color light pulse. Manipulations that become necessary are the second-harmonic generation in a nonlinear crystal taking place either before entering the interferometer or in one of the two arms of it; time-delaying ω with respect to 2ω ; and rotating the polarization of the fundamental by 90° so that the two pulses' polarization will lie in the same plane (if the goal is to work with linear polarizations). The drawback of such a separation of the pulses apparently is the high sensitivity of the setup to the environmental perturbations of mechanical origin. In order to overcome such an obstacle when aiming to work with few-cycle or even single-cycle pulses, we chose a collinear setup, to some extent similarly to the implementation in [106, 137]. Here all optical components, that is the second-harmonic crystal, the birefringent crystal that acts as a time-plate, and the waveplate are placed one after the other. Now mechanical vibration will affect both beams equally, and this provides a robustness to this setup. Implementing the two-color waveform-synthesis for near single-cycle pulses was not a trivial task. Naturally, all-reflective optics had to be used, and when we had to go through some material, the thinnest possible components were employed. The high peak intensity of our short pulse meant that we had to work most of the time close to the damage threshold of our optics elements. The major innovations in our realization was the application of the thinnest possible optical components, housing the whole setup in a vacuum chamber to minimize again dispersion, which required that all the adjustments, optimizations had to be carried out by using motorized vacuum-compatible components. Moreover, we had to find the best possible silver mirrors that still reflect in the long-wavelength UV and with low GDD (Type II enhanced silver mirrors from Femtolasers). At the same time, these steps that became necessary to preserve the short pulse duration, made everything more challenging

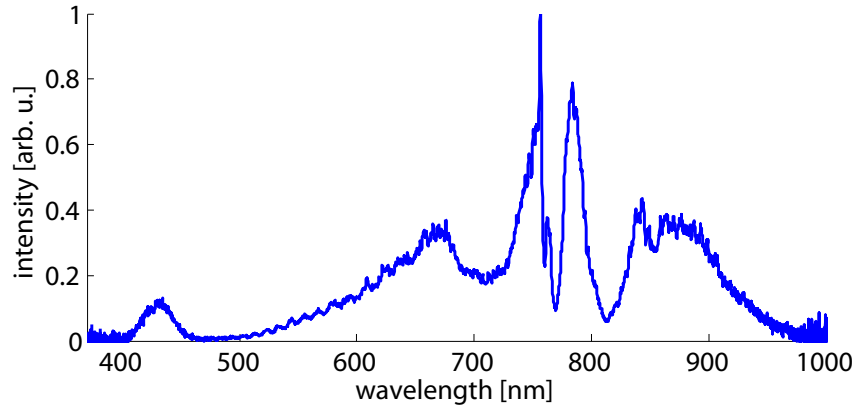


Figure 5.3: Spectrum created by our setup based on generating a detuned second-harmonic wave. This combined spectrum was used afterwards for HHG.

to work with. However, as we will see these measures allowed us to access a region of HHG that was not within reach before.

The rationale behind using the above optical components was the following. Concerning the second-harmonic generation (SHG), we had to find an efficient way to further broaden our spectrum, to a bandwidth extending to more than one octave. The spectrum that we could achieve has been plotted in Fig. 5.3. SHG in our case was realized in a BBO crystal operating with Type I phase-matching (PM). Due to this specific PM geometry, the polarizations of the fundamental wave and the newly generated wave were orthogonal to each other. The orthogonality is not a bad feature when it comes to time-delaying pulses. Birefringent crystals are anisotropic materials which exhibit two refractive indices, called ordinary (n_o) and extraordinary (n_e). They show a special property, which is the angle-dependent propagation time for one of the two waves that form the normal modes of the anisotropic medium. What is most useful about it is that essentially the extraordinary blue pulse can propagate faster than the ordinary fundamental pulse and this propagation time through the crystal can be simply adjusted by rotating the crystal. If we intend to do HHG for linearly polarized pulses having the same polarizations, a restoration of the polarizations after the time-plate is necessary. This can be achieved by using a $\lambda/2$ waveplate. Basically, it has the task of rotating the polarization of the fundamental by 90° . Each of the components will be analyzed more in detail below.

The laser pulse that we used for our experiments was generated by the Ti:Sa laser system that was thoroughly described in chapter 3 of this thesis. For the first time in attosecond experiments, we had our laser in a clean-room environment and the experiment took place on another floor, at a distance of approximately 15 meters from the laser source, the two being connected by a vacuum beamline. A sketch of the beamline, the HHG chamber, the chamber used for the diagnostics can be seen Fig. 5.4. During the experiment

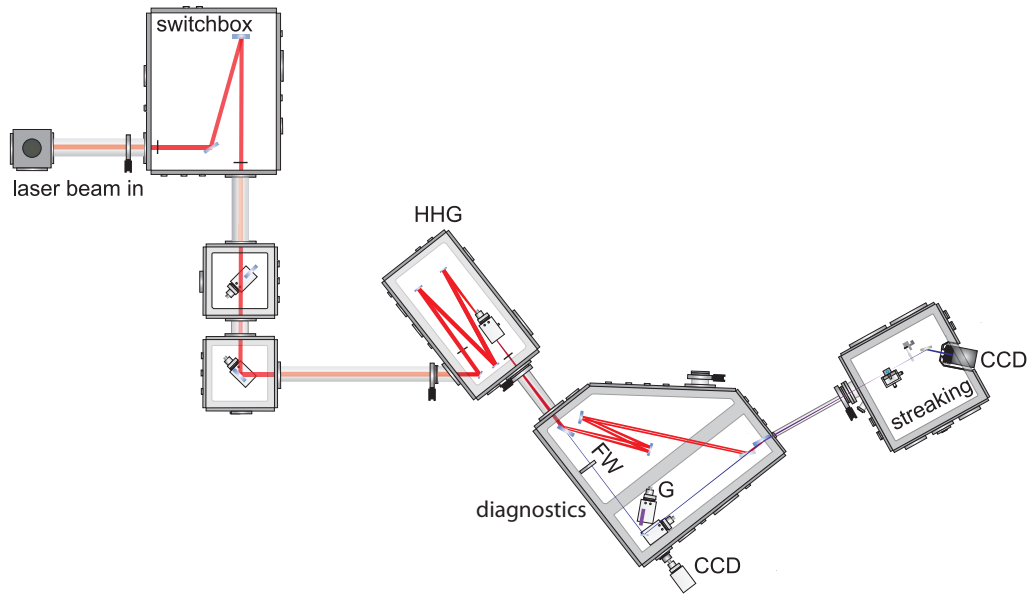


Figure 5.4: Our attosecond vacuum beamline that we used during HHG experiments. The beam from our Ti:Sa laser system entered the beamline from the left and propagated through vacuum tubes, the steering of the beam done by reflections off some silver mirrors. In the sketch FW: filter wheel that we used for holding our various filters for blocking the laser light (Zr) and for the calibration (Al, Si); G: grazing-incidence grating. The HHG chamber in the illustration contains only components corresponding to a normal HHG setup. The one we had in reality can be seen in Fig. 5.5. In the future streaking of the waveform will be carried out in the streaking chamber, as discussed in the 'Conclusions and outlook'.

the chirped-mirror (CM) compressor (not shown in the figure), used for the temporal compression of the pulses to obtain their near-transform-limited duration, was installed in a vacuum chamber. This chamber was a switchbox that served as the location where a rerouting of the beam could happen, so that it was possible to switch to other experiments using the same laser. The advantage of keeping the CM compressor in vacuum was that self-phase modulation (SPM) in the entrance window of the beamline (fused silica, $500 \mu\text{m}$ thick) could be thus avoided. SPM is a peak-intensity dependant process, as well as self-focusing, and these two effects can distort the beam temporally and spatially, respectively. By keeping the pulse duration longer than its transform-limited value, we were able to lower the peak intensity in the window below the level where these detrimental nonlinear effects occur. Another important factor in our experiment is the ability to change the pulse duration so that the pulse becomes perfectly compressed at the place where HHG takes place. To this end, a pair of wedges was placed after the hollow-core fiber, which permitted a continuous tuning of the pulse duration.

Our experimental setup that we used to modify the time-evolution of our driver laser pulse on a sub-femtosecond time-scale can be seen in Fig. 5.5. In this picture the HHG

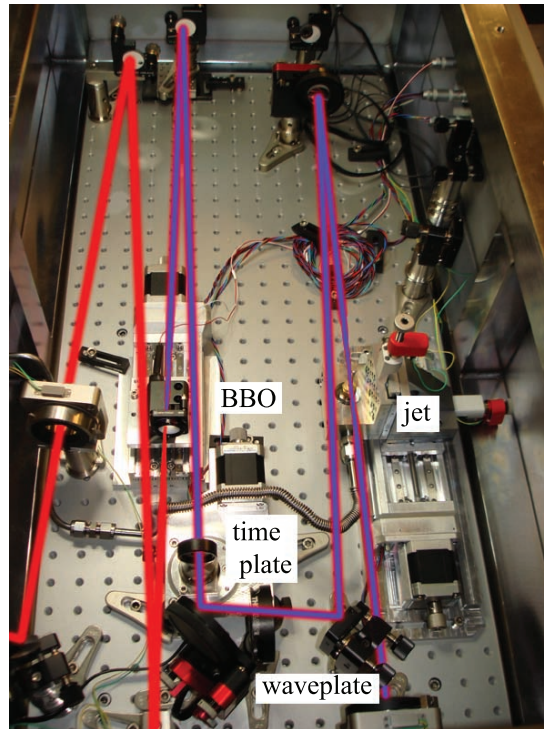


Figure 5.5: Experimental setup for broadband two-color waveform synthesis, housed in a vacuum-chamber. Our scheme was based on a collinear arrangement of the optical components, these elements being denoted in the picture as BBO, time-plate and waveplate. Red line indicates fundamental pulse, and blue the detuned second-harmonic wave. The near-single-cycle laser pulse entered the setup from the left in the picture, and went out of the chamber in the bottom right corner to another chamber, where the HHG diagnostics was situated (shown in Fig. 5.4).

part (Ne gas jet) of the experiment is shown, too, except for the HHG diagnostics, which was built up in another vacuum chamber (see Fig. 5.4). The fundamental beam entered the HHG chamber, which housed our broadband two-color waveform synthesis setup, and after two reflections on flat protected silver mirrors (P01 from Thorlabs and Type II from Femtolasers) the beam was focused by a concave mirror with a focal length of 37.5 cm. SHG took place in a BBO crystal and this nonlinear crystal was placed after the focus of the beam. It was necessary to re-collimate the beam afterwards, which was done by another concave mirror of the same focal length as the one used for focusing it. Whenever a concave mirror is utilized, and a beam with non-perpendicular incidence hits this focusing mirror, astigmatism can occur. Astigmatism, when the beam has different focusability in the two perpendicular planes, is a harmful phenomenon, because the resultant non-ideal beamsizes severely influences the highly nonlinear HHG process. To avoid it, or at least to minimize its presence, a carefully chosen angle of incidence (as small as possible) on the mirror is a must. After re-collimation, the two beams of different wavelengths went through two more materials, first the time-plate, followed by the waveplate. Apparently,

pre-compensation of the dispersion-induced pulse-broadening effect due to these materials was unavoidable, and this was carried out by a movement of the wedges by an appropriate amount (by taking glass out). In fact, such a pre-chirping of the fundamental not only ensures that our originally available pulse will reach the HHG target compressed, but it influences the second-harmonic pulse duration, too. What is more, this effect is beneficial, because there is a transfer of the pre-chirp in the SHG crystal from the fundamental to the SH pulse [138]. These can be written as $\text{GDD}_{SH}=1/2 \text{GDD}_{FUND}$ and $\text{TOD}_{SH}=1/4 \text{TOD}_{FUND}$ and we can see it that it helps in our effort to keep the SH pulse relatively short.

Another aspect to consider during a feasibility study is the effect of two colors on the focused beamsizes. In this respect, a strong fundamental and a weak second-harmonic pulse did not bring up serious issues, in contrast to the problem that one would have to face when dealing with a fundamental and its subharmonic. In particular, the diameter of the focused spot ($1/e^2$ size, so the diameter where the on-axis peak intensity drops by this factor) of a Gaussian beam is [139]:

$$2W_0 \approx \frac{4}{\pi} \lambda F_{\#} \quad (5.2)$$

with $F_{\#} = \frac{f}{D}$. Here $2W_0$ is the diameter of the focused beam, $F_{\#}$ is the F-number of the lens (here spherical concave mirror), f the focal length, D being the beamsize on the mirror. We see in this equation that there is a wavelength-dependence of the focal spot size, and it means that for a second-harmonic we can expect to have half the focal size of the fundamental. The two laser beams that are harmonics of each other will thus partially overlap, and due to the size difference, the effective intensity ratio will increase. This seems like a positive effect at first: the interaction, the effect we can expect from the two waves should be larger during the observation of HHG. On the other hand, only the middle circular spatial part of the total beam will "contain" the two-color effect, while to the outer rim of the beam only the fundamental will contribute. Such a situation, the intensity ratio between the two varying would have very likely fatal consequences for an experiment that was proposed in theory for a fundamental and its sub-harmonic [112], as now this ratio will take on a smaller value. If the subharmonic generation has low efficiency, then together with this focusability issue for the two disparate wavelengths, one might not see any effect. For us, however, this did not constitute a problem, also because of another effect that compensated for the reduced size of the second-harmonic. Namely, we will see in equation 5.4 that the SH intensity depends quadratically on the fundamental's intensity, and it means that the SH beam that reflects on the focusing mirror before the HHG target will be smaller than that of the fundamental. According

to the definition of the F-number the parameter D will change this way ($D_{2\omega}=D_{\omega}/\sqrt{2}$) and as a result, based on equation 5.2, the focused beamsizes will be enlarged. All in all, we will get a very good spatial overlap in our experiment. For the sub-harmonic case, however, this effect will no longer be a compensating effect: on the contrary, it will make the situation even worse, as it will create an even larger sub-harmonic beamsizes.

5.3.1 Second-harmonic generation (SHG) crystal

Second-harmonic generation (SHG) was utilized to extend the bandwidth of our laser pulse to more than one octave. There are a number of ways to generate second-harmonic in a nonlinear crystal. The concept of phase-matching has to be explained briefly here. When a wave due to its high intensity generates other frequency components through the nonlinear polarization (in a medium with no inversion-symmetry), efficient build-up of the harmonic wave can happen only if constructive interference occurs for the generated wave along its propagation. So that this situation holds, the wavenumbers of the interacting waves have to satisfy the equation $\vec{k}_3 = \vec{k}_1 + \vec{k}_2$, where the index 3 denotes the newly born wave, while 1 and 2 are the signal and idler waves. The methods that come into considerations for SHG are Type I, Type II phase-matching in some common crystals, such as BBO, KDP, LBO or quasi-phase-matching (QPM) in periodically-poled (PP) crystals, for example in PPKTP, PPLN (LN means Lithium-Niobate) or PPLT (LT stands for Lithium Tantalate). Regarding the crystals with periodic-poling a domain inversion is built into them, which means that the sign of the nonlinear coefficient is intentionally reversed. This reversal happens after the coherence length, the distance where the fundamental field and the newly generated second-harmonic field become phase-shifted by π with respect to each other [4]. After such a distance the nonlinear conversion efficiency would drop normally, but periodically poled crystals overcome this limitation, thus permitting an extended length over which conversion can take place. It is basically a fundamentally different approach to normal phase-matching in a birefringent crystal, whereby the phase-velocities of the original and the harmonic waves can be matched due to the crystal anisotropy. For our purposes, that is for HHG done both beams (that are harmonics of each other), it would be an ideal candidate for the realization of SHG. One very exciting possibility is the generation of SH pulses that are pre-chirped, which would enable us to have compressed SH pulses on target. This can be achieved via an engineering of the poling period in the crystal [140, 141]. However, the major obstacle for applying PP crystals for our experiment, is that for such a crystal, all waves are polarized in the same plane (Type 0 phase-matching), and as a result, there is no way to compensate afterwards for the time-delay between the two pulses using the birefringency of a timeplate (see next section). They will inevitably slip away from each other, and there will be no modification

of the original waveform due to the addition of the SH.

Other SHG techniques are based on using bulk birefringent crystals. Type II PM can be realized in four different configurations (e and o being the abbreviations for extraordinary and ordinary-waves): eo-e, oe-e, eo-o, oe-o, where the first two are the polarizations of the fundamental wave, and the last letter is the polarization of the second-harmonic. As we can see, the fundamental will be split into two different waves, e- and o-wave. If we want to use again a birefringent crystal as timeplate, it means that only half of the power of the fundamental will be available, since the fundamental and the second-harmonic have to be perpendicular to each other, one being an e- the other an o-wave. Moreover, Type II PM gives a small phase-matching bandwidth, the bandwidth that limits the second-harmonic pulse duration.

Type I PM, however proves to be suitable for realizing our goals. This PM deals with the fundamental being an o-wave, the second-harmonic an e-wave (oo-e interaction). The phase-mismatch for the different frequencies that make up the pulses can be written as:

$$\Delta k(\omega) = k_{2\omega} - 2k_{\omega} = \frac{n_{2\omega}2\omega}{c} - \frac{2n_{\omega}\omega}{c} \quad (5.3)$$

For perfect phase-matching to occur, based on the above equation, $n_{2\omega}=n_{\omega}$ has to be fulfilled, and this can only happen if the second-harmonic is an e-wave (for negative uniaxial crystals for which $n_e < n_o$). Using equation 5.3 and equation 5.8, it is possible to derive the phase-matching angle, the angle between the k-vector of the fundamental wave and the optic axis of the crystal. For frequency-doubling with BBO it is 29° . Now the phase-mismatch factor that we obtained above directly influences the phase-matching bandwidth, which tells us the width of the spectrum we can approximately phase-match. To derive this important factor, let us first examine the SH intensity after the crystal, which is proportional to:

$$I_{\lambda/2} \propto (I_{\lambda} L d / \lambda)^2 \text{sinc}^2(\Delta k L / 2) \quad (5.4)$$

In the above equation, L is the crystal length, λ is the wavelength of the fundamental, d is the nonlinear coefficient, I is the intensity and $\text{sinc}(x)$ is 1 at $x=0$, and $\sin(x)/x$ elsewhere. It can be inferred from this equation that because the signal strength at the output depends quadratically on the crystal length, a longer crystal should be chosen; on the other hand, the phase-matching bandwidth will suffer, which will narrow and this will result in a longer pulse. The phase-matching bandwidth is the full-width at half maximum (FWHM) of the sinc curve, which function drops to half of its maximum for $\Delta k L / 2 = \pm 1.39$. The equation for the phase-mismatch, equation 5.3 can also be simplified. When we introduce a variation of $\delta\lambda$ for the fundamental, the second-harmonic's wavelength will change by

$\delta\lambda/2$. To first order with respect to $\delta\lambda$ equation 5.3 now reads as (expressed as dependent on wavelength):

$$\Delta k(\lambda) = \frac{4\pi\delta\lambda}{\lambda_0} \left[n'(\lambda_0) - \frac{1}{2}n'(\lambda_0/2) \right] \quad (5.5)$$

Above, λ_0 denotes the central wavelength of the fundamental, and "′" means first derivative with respect to wavelength. The phase-matching bandwidth can be obtained by combining this equation with the equation that defines where the sinc function will decrease by a factor of 2 and it can be written as:

$$\Delta\lambda = \frac{0.44\lambda_0/L}{|n'(\lambda_0) - \frac{1}{2}n'(\lambda_0/2)|} \quad (5.6)$$

This bandwidth in case of a 100 μm thick BBO for $\lambda_0=760$ nm is 38 nm, which means we only convert this small portion of our fundamental, while for a ten times thinner crystal we could phase-match virtually the whole bandwidth. Experimentally, we have found that our 100 μm BBO (from EKSPLA) gave the best conversion efficiency, and therefore this turned out to be our chosen crystal thickness afterwards. Another advantage of using it is that such thicknesses are available without a substrate (such as UV fused silica) holder, which means no extra dispersion pre-compensation measures have to be taken beyond what needs to be done by negatively pre-chirping the pulse due to the BBO itself (which introduces $\text{GDD}_{FUND}=8$ fs² and $\text{GDD}_{SH}=17$ fs²). From equation 5.4 we can see that the SH intensity depends quadratically on the peak intensity of the incoming wave, and if pre-chirping was necessary, it would entail a considerable drop in the peak intensity. To counteract such a change, we focused the fundamental light into the crystal. Focusing and recollimating the beam was done by two concave mirrors of the same focal lengths. Another possibility of changing the beam-size would involve a telescope made up of a concave and a convex spherical mirrors. However, this option would take away the flexibility that we have with the the normal focusing-recollimating geometry, which is that varying the intensity of the beam can be realized with the movement of the BBO along the beam direction. For the telescope a complete change of all focusing mirrors would be necessary (including the one before the HHG target). Another major issue that blocks this idea is that on the second mirror of the telescope the intensity would be over the damage threshold of the mirror. In the end our conversion efficiencies of SHG reached about 6-7% when aluminum mirrors were installed after the BBO, while the conversion was lower, about 4% with silver mirrors in the beampath. We see that aluminum mirrors are enticing components to be used, however, they show high reflectance at the cost of a significantly lower reflectance for the fundamental at around 800 nm. Therefore, we kept the silver mirrors in our setup. Angular tuning of the BBO to find the correct phase-

matching angle was carried out in vacuum with the help of motorized rotation mounts, and the total beam was picked up, then sent out to another chamber, where the power, as well as the spectral measurements for the laser beams happened (same chamber as where the HHG diagnostics was set up). During our experiments we utilized both anti-reflection-coated (AR-coated) and only protective-coated (P-coated) BBO crystals, and the reflection per surface was below 2% and around 3%, respectively. The SH spectrum, where the maximum conversion was achieved, was detuned from being an exact second-harmonic of the center wavelength of the fundamental (760 nm \rightarrow 380 nm), the reason being the rapidly falling reflectance of silver in the UV towards decreasing wavelengths. The total spectrum that was realized with our setup has been plotted in Fig. 5.3. The detuned nature of the second-harmonic, fortunately did not affect severely the success of our HHG experiment, as we will see it later. Our fundamental was a near single-cycle pulse, so for the high energy XUV spectrum only one or two cycles contributed. The detuned wavelength of the SH within such a short time interval of 3 femtoseconds therefore did not constitute a big difference from the point of view of the overlap between the two laser pulses.

5.3.2 Timeplate

In order to reach the strongest effect from the 2ω field, it is essential to provide a means for overlapping both beams in space and time. The time-overlap was possible through the usage of a birefringent crystal. Normally, the dispersion of media in the visible and near-infrared is such that long wavelengths propagate faster than the short ones. This is the case, because a resonance of most materials exists in the blue, and towards higher wavelengths, the refractive index is decreasing with wavelength. As we have seen it in chapter 3, the group-velocity (v_g) describes the speed of propagation of the pulse, more exactly its envelope. The group-velocity is directly linked to the way the refractive index changes as a function of wavelength, because:

$$v_g = (\partial k / \partial \omega)^{-1} = c / [n(\omega) + \omega \partial n(\omega) / \partial \omega] \quad (5.7)$$

Here the angular frequency has to be evaluated for the center frequency of the pulse. Equation 5.7 explains why the group-velocity decreases for larger frequencies (ω) when the refractive index ($n(\omega)$) shows a monotonously decreasing dependence on wavelength (i.e. increasing dependence with respect to frequency). In our setup as mentioned above, we used an SHG crystal, a time-plate (represented by a birefringent crystal) and a waveplate. The time-delays that were introduced by the SHG-BBO crystal and the waveplate were positive (defined as $\Delta t = t_{\text{SH}} - t_{\text{FUND}}$, where t was the travel time of the respective beam

through the crystal), expressed quantitatively they were 12.5 fs and 6 fs, respectively. A time-plate, which was realized by a birefringent crystal made out of α -BBO (a linear crystal with the same optical properties as that of β -BBO, except it is not nonlinear), provided a time-delay that was opposite to that of the positive time-delay as given by the SHG-BBO and the waveplate. The choices of suitable materials that can act as time-plates, thus ones that exhibit a negative time-delay for the propagation of the fundamental and the second-harmonic wave are listed in Table 5.1. The values that appear in the table

	α -BBO	calcite
Δt @ $\theta = 50^\circ, +3^\circ$ [fs]	-9.6, -12.3	-21.6,-25.2
GDD @ 760 nm [fs ²]	8.1	8.3
GDD @ 430 nm [fs ²]	15.2	12.3
R @ 760 nm [%]	6.2	6.0

Table 5.1: Properties of potential materials to be used as time-plates. Here Δt is the time-delay between the second-harmonic (SH) and fundamental pulses, negative value meaning faster SH pulse; GDD denotes group-delay dispersion; and R is the reflection coefficient per surface for the intensity in case of normal incidence for the fundamental wave. The numbers have been given for a crystal thickness of 100 μm .

have been calculated for a crystal thickness (L) of 100 μm . The group-delay dispersion (GDD) for the waves has also been given in the table, which is the second derivative of the spectral-phase and this parameter is connected with the dispersive spreading of the pulse. The group-velocities for the ordinary (fundamental pulse) and extraordinary (second-harmonic) waves were obtained by using the corresponding Sellmeier-equations that characterize the dispersion of the refractive indices n_o and n_e . The extraordinary wave has a refractive index that is dependent on both of these principal indices and it can be written as [139]:

$$1/n_{\text{eff}}^2(\theta) = \sin^2(\theta)/n_e^2 + \cos^2(\theta)/n_o^2, \quad (5.8)$$

where θ is the angle between the k-vector of the propagating mode and the optic axis of the crystal. In the table one can find also the effect of a crystal rotation (an angular change of $+3^\circ$) on the change of the time-delay. We can see that we are capable of minute time-delay tunings with the help of varying the crystal angle. The waves as they enter the time-plate and the orientation of the crystal (cut-angle, $\theta = 50^\circ$; crystal thickness, $L = 150 \mu\text{m}$) are shown in Fig. 5.6. For our experiment, the selected material was α -BBO (from Newlight Photonics, Toronto). Even though calcite has better time-delay properties (per unit length), experimentally our XUV yield with α -BBO proved to be by a factor of 3 larger (with no phase-stabilization running) than when we used calcite. These materials have similar theoretical Fresnel-reflections for the incoming fundamental wave (as shown

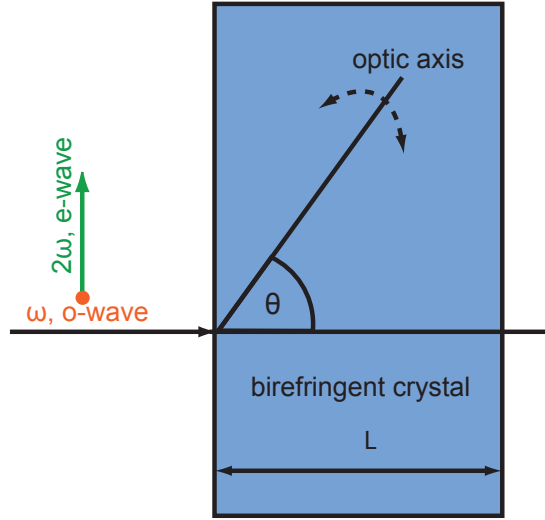


Figure 5.6: Time-plate for time-delaying two pulses of different wavelengths. To make the blue pulse catch up with the fundamental pulse, we exploited the birefringence of a crystal. In this sketch the incoming waves' polarizations (orthogonal to each other) and the crystal orientation are shown. The dashed curve with two arrowheads indicates the rotation possibility of the crystal, which results in a variable time-delay.

in the table), and therefore what could be the cause for a lowered transmitted laser beam energy, by implication a smaller XUV photon flux in case of calcite, is perhaps the inferior manufactured quality of the crystal.

5.3.3 Waveplate

Since Type I SHG was utilized in our setup and our goal was to carry out HHG with parallelly polarized fundamental and second-harmonic pulses, a half-wave ($\lambda/2$) waveplate had to be employed. Our waveplate was a true-zero one, its thickness set such that it behaved as a half-wave plate for our fundamental pulse in a very broad bandwidth, while it was a full-waveplate for the second-harmonic around 400 nm. A reasonable question could be: why was it necessary to rotate the fundamental in the first place and not the second-harmonic? Perhaps the bandwidth of "perfect" rotation could be thus kept broad, broader than with our chosen method. However, by simple maths, it turns out that if we do so, for the fundamental wave we will actually obtain the performance of a quarter-wave plate. This would entail that the linear polarization of the fundamental would be converted to circular; which is obviously not our intention.

A waveplate can be created from any birefringent material. By making sure that the optic axis is parallel with both the entrance and the exit surfaces of the crystal, the incoming frequency components of a pulse will be split into two waves propagating with different velocities. These orthogonal linearly polarized components are the extraordinary

(e-wave) and ordinary wave (o-wave), which can be characterized by their two indices of refraction n_e and n_o (for uniaxial crystals, materials having one optic axis). Because they influence the propagation speeds, depending on which one is smaller, one wave will go through the crystal slower than the other. The axis along which the faster moving wave is polarized is called the fast axis, while in the orthogonal direction lies the slow axis. There exists a phase difference between them, and it is called retardance Δ . When they emerge from the crystal, the resultant vector, the polarization state of the light, will be a superposition of these two components. For a half-waveplate the retardance is π , and it can be expressed using the wavenumber evaluated for the e-wave and o-wave, as well as waveplate thickness L :

$$\frac{2\pi}{\lambda}L|n_e - n_o| = \pi \quad (5.9)$$

We used crystal quartz in our experiments, because it is a strong material, and thus it lends itself to the fabrication of low-order, eventually even zero-order waveplates. From equation 5.9 the necessary crystal thickness can be obtained, which is $42 \mu\text{m}$.

Beyond this, through further theoretical calculations we simulated to which extent such a thin waveplate rotates the fundamental wave's frequency components, and how well it leaves the polarization of the second-harmonic's spectral components unchanged (more correctly said, it should rotate the latter by 180°). If the fast axis is along the x axis, while the slow axis is parallel to the y axis in a cartesian coordinate system the phase-delays can be written as:

$$\varphi_y = \frac{2\pi}{\lambda}Ln_e \quad (5.10)$$

$$\varphi_x = \frac{2\pi}{\lambda}Ln_o \quad (5.11)$$

Using the Jones-matrix formalism [142], we can assess what the outgoing wave's two vector components will be. It is possible to see how much cutting on the tails of the spectrum would occur if we had a polarizer after the waveplate, oriented at -45° , with the incoming wave's linear polarization being at an angle of 45° (the angles in both cases measured with respect to the x axis). In other words, the bandwidth reduction can be estimated this way. This step is justified, since we use a pellicle afterwards (at Brewster's angle for the polarization we want to keep)) to clean the polarization, to retain only the component that is along the direction at -45° . The resultant wave's E_x and E_y components can be expressed with Jones matrices as:

$$\begin{bmatrix} E_x \\ E_y \end{bmatrix} = \begin{bmatrix} 1/2 & -1/2 \\ -1/2 & 1/2 \end{bmatrix} \begin{bmatrix} e^{j\varphi_x} & 0 \\ 0 & e^{j\varphi_y} \end{bmatrix} \begin{bmatrix} E_{in}/\sqrt{2} \\ E_{in}/\sqrt{2} \end{bmatrix} \quad (5.12)$$

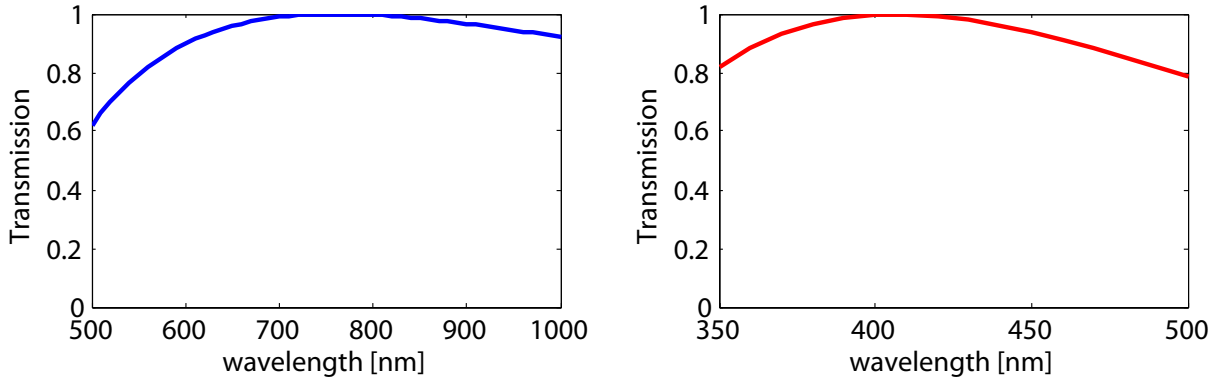


Figure 5.7: Theoretical amplitude transmission of our $\lambda/2$ waveplate as measured after a perfect polarizer. The thickness of the true zero-order waveplate was $42 \mu\text{m}$, therefore it rotated the polarization of the fundamental by 90° , and that of the second-harmonic by 180° . The rotation was not perfect for all wavelengths, and it caused a bandwidth reduction for our pulses, as determined by these transmission curves.

In the above equation the first matrix after the equal sign is the polarizer's Jones-matrix, the second corresponds to that of the waveplate, while the third is the incoming wave's vector components, with E_{in} being the magnitude of the vector. If we take E_{in} equal to 1, the outgoing wave's magnitude, and therefore the transmission of the combination of a waveplate and a polarizer as a function wavelength will be simply $\sqrt{E_x^2 + E_y^2}$. The transmission function that we calculated this way can be seen in Fig. 5.7. We can confirm that the bandwidth in which satisfactory rotation is realized is large enough to preserve the spectrum of a near-one-octave fundamental pulse, and that of the second-harmonic, as well. The power that is not transmitted through this system naturally goes somewhere, and for a waveplate it is the perpendicular polarization component that gains some intensity. Our pellicles that serve as our polarizers, introducing no extra dispersion due to their almost negligible thickness of below one μm , simply cannot totally extinguish this detrimental polarization component, and thus some low amount of elliptical polarization will remain.

Apart from the above characterization of the waveplate, we can learn more about this element's effect on our pulse. By taking the first derivative of the phase from equation 5.12 with respect to the angular frequency we can calculate the propagation times for both the fundamental and the second-harmonic pulses. From this one can deduce the time-delay, which is positive, and this number was mentioned in section 5.3.2 above. If the second derivative is calculated, we can obtain the respective pulses' GDD values. The GDD for the fundamental at 760 nm is 1.9 fs^2 , and for the second-harmonic at 430 nm it is 4.3 fs^2 .

5.3.4 Pellicles

The HHG process is intrinsically very sensitive to the polarization of the driver field. Unless we intentionally control the polarization of the wave [72, 73] by introducing an elliptical polarization to it (the time evolution of the polarization being elliptical-linear-elliptical), it can severely harm HHG. The reason for this is that due to some orthogonal component of the field, the electron during its acceleration along its trajectory, can get deflected by the field in such a manner that eventually it will never return to the parent ion; thus no XUV photon will be generated. A clean linear polarization is therefore an essential prerequisite for a high XUV yield. To eliminate the undesired electric field component of the wave, so as to reach a high linearity for the polarization, it has become a common technique to employ pellicles before reaching the gas target. In our case it is even more imperative to use them, since the waveplate as described in the previous section will introduce some ellipticity to the beam. Pellicles are very thin materials that work on the principles of a Fabry-Perot etalon, so they exploit interference, constructive and destructive, for the polarization component that gets multiply reflected on the surfaces. Any wave can be decomposed into s and p wave, which will exhibit different transmission properties (due to Fresnel reflection) when propagating through a material. By placing a pellicle, made out of nitro cellulose ($n=1.5$) at Brewster's angle for the p-wave, it is possible to obtain perfect transmission for this polarization component, while for the s-wave interference will occur, which will result in a modulated transmission function. The pellicles that we used have a thickness below $1 \mu\text{m}$, which means that our pulse duration will remain virtually the same after propagating through them, and this feature makes them ideal for use with few-cycle pulses. The transmission function of a Fabry-Perot interferometer can be written as:

$$T_{\text{total}} = \frac{T^2}{1 - 2R \cos(\delta) + R^2}, \quad (5.13)$$

where T and R are the transmission and reflection values (intensity) of a single pellicle for an s-wave with an angle of incidence of 56° , while δ can be expressed as:

$$\delta = 2 \frac{2\pi n(\lambda)}{\lambda} L \cos(\theta) \quad (5.14)$$

Here L denotes the thickness of the material, and θ is the angle of refraction, which in our case is equal to 33.5° . The calculated transmission function for s-polarization for a pair of pellicles with different thicknesses can be seen in Fig. 5.8. This curve shows an optimized case, where our optimization goal was set such that evidently the best transmission for a pair has the most flat behavior in a wide wavelength range, in the

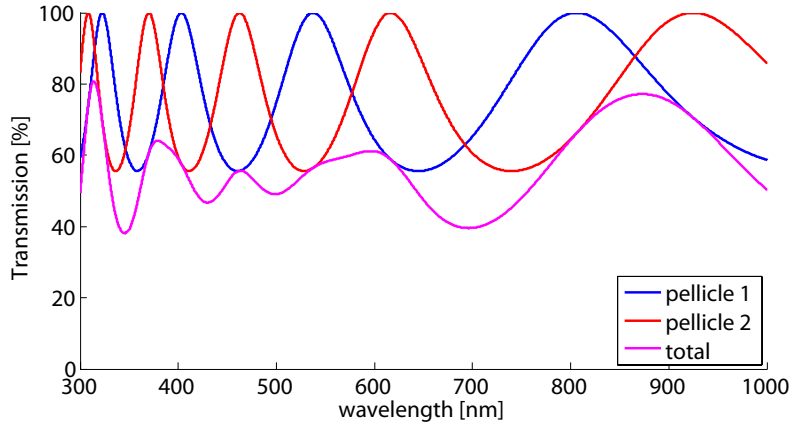


Figure 5.8: Theoretical transmission of a pair of pellicles for s-polarization with optimized thicknesses, placed at Brewster’s angle. Pellicle 1 had a thickness of $0.64 \mu\text{m}$, while pellicle 2 was $0.74 \mu\text{m}$ thick, and the transmission curve for each of them has been plotted, as well their total transmission, which shows a relatively flat performance over the wavelength range of interest for us.

interval where our driver laser’s spectrum is situated (400–1000 nm). This scenario gives the most cancelation for the unwanted polarization component. As we can see it, on average the transmission can be reduced to $\approx 55\%$ for one pair. In our setup it was critical to use them (manufactured by National Photocolor), as we had to work with a waveplate in the beampath to set the fundamental and the second-harmonic waves’ components to be parallel to each other. The waveplate cannot rotate all wavelengths by the prescribed amount, and thus a degradation of the polarization cleanness of the laser beam happens. Our pellicles helped us to overcome this issue in a bandwidth of more than one octave.

5.4 Experimental results and theoretical analysis

We performed our experiments with the setup as described in section 5.3 and the HHG conditions as given in section 2.4.2. Before the measurements took place, we carefully calibrated our spectra by moving Si and Al filters into the beam, enabled by the filters’ transmission showing a clear absorption edge (as explained in Appendix A). To improve our spectral resolution we inserted a slit into the beampath after the harmonic generation, selecting the central portion of our harmonic beam. First, we carried out HHG spectral characterization with the near-single-cycle fundamental pulse only, the results of which have been discussed in section 2.4.3. Following this, by keeping the same phase-stabilization in operation and taking into account the CEP-slippage introduced during the switch-on step of the SH (see section 5.4.1), we changed to HHG with our new combined waveform. The fundamental’s spectrum for $\text{CEP}=90^\circ$ before this step was recorded and it can be seen in Fig. 5.13. With our superimposed wave we carried out a detailed inves-

tigation on the parameter dependence of HHG regarding the fundamental's CEP value and the time-delay between the two laser pulses. Some important so-called "time-scans" will be shown in section 5.4.2. During our experimental work we arrived at a number of observations that will be listed below. The most outstanding result, we believe, is that we managed bring into HHG both broad and fine tunability of the continuum. In our presentation of our experimental results we will furthermore give a comparison of best HHG continuum obtained with fundamental only and with the SH added; discuss the interference fringes that we saw in connection with the emergence of two or three pulses; we will show evidences of a quantum path interference of long- and short-trajectories. Time-frequency analysis and trajectory calculations (by Ya Cheng's group) will support our findings.

5.4.1 CEP slippage due to the SHG crystal

Technically, in our experiments we strived to avoid the introduction of additional dispersion between HHG with fundamental only and HHG with our new waveform. We wanted to keep the same pulse duration and the same CEP for the fundamental in both experiments. It turned out that while maintaining the near single-cycle pulse duration was possible, the CEP could not be preserved. In chapter 2 section 2.4.2 we presented our spectral measurements for HHG with fundamental only, where we briefly mentioned that switching between the experiments (HHG with fundamental only and later with the SH added to it) was done by a rotation of the BBO in a plane that is perpendicular to the propagation direction of the beam by 90° . It let us introduce or "take out" the second-harmonic by turning on or off the nonlinear coefficient of the crystal. Evidently the thickness of the SHG crystal between the two cases did not change, so the pulse duration was not altered. On the other hand, when the SHG crystal behaved as a nonlinear crystal, the SH and the fundamental was an e-wave and an o-wave, respectively, and when it was set so that it acted like a normal linear crystal (no SH) the two normal modes were swapped, which means the SH became an o-, the fundamental turned into an e-wave. For the two kinds of waves, there are two different propagation properties, and effectively it induced a CEP change for the fundamental. This variation can be expressed as:

$$2\pi L \left[\frac{dn_o}{d\lambda} - \frac{dn_{eff}(\theta)}{d\lambda} \right] = 1.23 \text{ rad}, \quad (5.15)$$

where L is the crystal thickness ($100 \mu\text{m}$), and the derivatives have been evaluated for the fundamental's center wavelength. After introducing the SH wave, we subtracted the above amount of CEP slippage, so that we could keep track of the actual value of the CEP of the fundamental during our experiment.

5.4.2 Time-scans

To find the waveform that gives the broadest bandwidth and the best tunability of the central energy of the XUV pulse we changed both the fundamental's CEP and the time-delay between the fundamental and its SH. We obtained thus a 2D map of the HHG spectra. We selected 3 CEP settings and the associated time-scans are shown in Fig. 5.9. For clarification, our CCD camera had a silicon nitride chip, and due to silicon's absorption edge at 100 eV we have a line at this energy value in all of our time-scans. The 2D plot in false-color representation on the top was the first time-scan that we acquired following our switching from HHG with fundamental only to HHG with our two-color waveform. For each time-scan we furthermore did a theoretical comparison and these are shown below each experimental scan. The theoretical spectra were calculated by Fourier-transforming the time-dependent dipole moment of the single-atom response. In the simulation the peak intensity for the fundamental was $4.7 \times 10^{13} \text{ W cm}^{-2}$, SH and fundamental pulse durations being 15 fs and 3.3 fs, respectively, their amplitude ratio being 1:6 (i.e. less than 3% SH intensity). From the match between theory and experiment, which we can deem to be fairly good, we were able to extract what CEP we had in our experiments. According to this analysis, for the top figure the CEP was determined to be 50° , for the middle it was 190° and for the one at the bottom it was 230° . The top and the bottom ones have a CEP difference of 180° , which manifests itself in a shift of the 2D pattern by a quarter of a period of the fundamental laser cycle. This symmetry concerning this shift becomes trivial if one depicts the fundamental and the SH wave, because to get exactly the same alignment of the two waves, more exactly the original waveform mirrored onto the time-axis we have to create both a time- and CEP shift with the above values. Similarly to how the HHG spectrum is not sensitive to a pulse shape change from cosine to anti-cosine (again mirroring the original pulse shape onto the time-axis) when one uses only the fundamental pulse, we obtain the same spectrum also in our case when applying two-color waveform-synthesized pulses after a change of both the time-delay and CEP (unlike in ATI as discussed in chapter 2). As a matter of fact, this feature that we have to change both the CEP and the time-delay to get the same HHG spectra contrasts with HHG done with fundamental only, and gives a solid proof that the SH is present. For HHG with fundamental only merely a change of the CEP equal to 180° is enough to generate the same HHG spectrum as can be seen in Fig. 2.5.

The middle time-scan will be a significant one for our further analysis, and we will use this time-scan in the next two sections. Unfortunately, in the experimental scan for this CEP as compared to the theoretical one, the pattern is time-shifted. We believe it has to do with the spatial filtering that we implemented with the insertion of a slit, which we used to improve our spectral resolution, as mentioned above. In another measurement

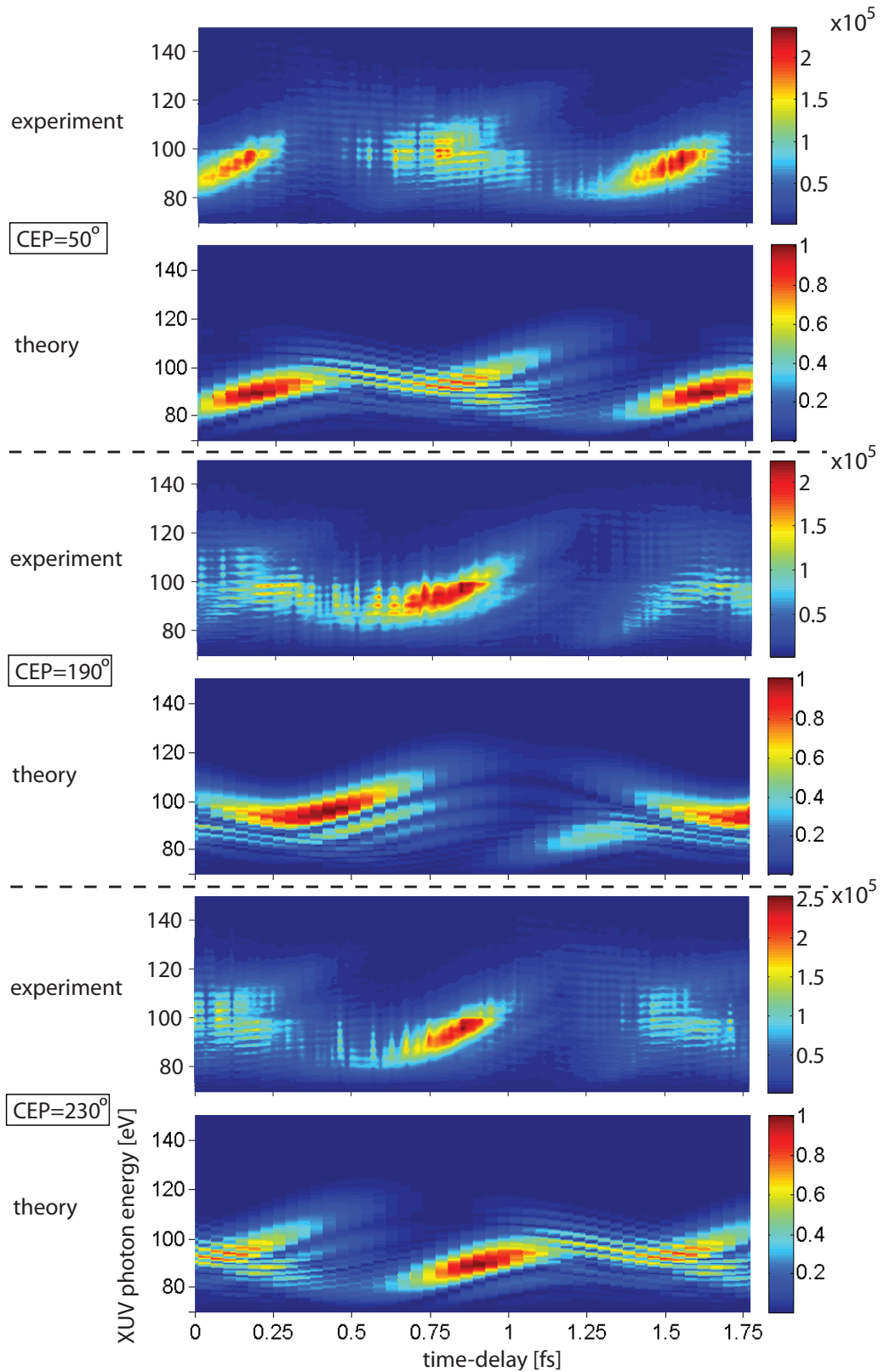


Figure 5.9: Time-scans for different CEP settings. The time-delay between the fundamental and the SH was varied in steps of 12 as, and in our experiment we changed the CEP in steps of $\approx \pi/4$. Three CEP settings have been selected for viewing purposes, and the corresponding single-atom calculations are shown below each of them.

campaign when we had no slit, the time-scan pattern moved as expected from theory; there, however, the spectral resolution was not sufficient.

5.4.3 Broadly and finely tunable continuum source in the XUV

Variation of the time-delay between the two pulses serves as a knob to introduce tunability into the HHG process. If we look at the middle plot of Fig. 5.9, as well as all the other plots (top and bottom plots) we can see that the high intensity portion shows no spectral modulation, which means the spectrum forms a pure a continuum. Such a continuum, with a steep fall-off of the cut-off part has been plotted in Fig. 5.10 for a specific time-

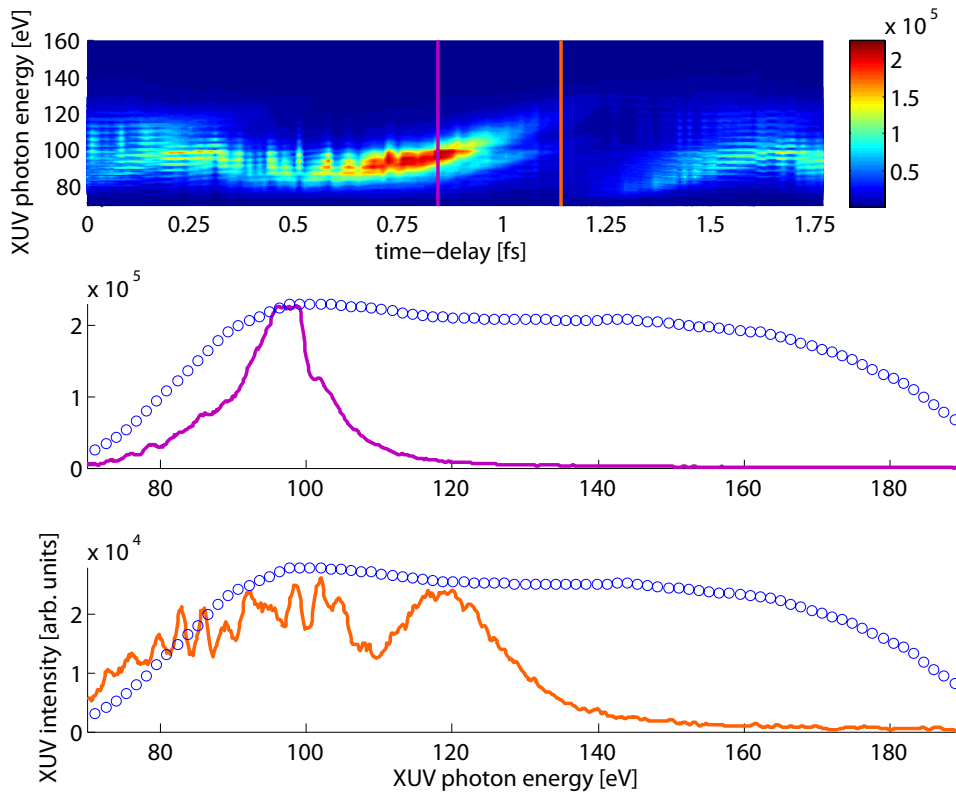


Figure 5.10: Broad tunability of the XUV continuum. Upper plot: for a specific CEP (190°) a time-scan is shown, where the time-delay between the fundamental and the SH is varied. At certain time-delays, indicated by the magenta and orange lines, two continua with different central energies and intensities emerged. One is a low energy, high intensity continuum (middle plot), while the other lies higher in energy, but has a low XUV yield associated with it. All measurements were conducted after the Zr filter, which has a transmission function as shown by the blue dots. For time-delays below ≈ 0.5 fs strong spectral modulation appears, which proves that we had sufficient spectral resolution. For those time-delays we no longer generate only one XUV attosecond pulse. The time-delay is only a relative value as we did not know exactly the time-separation of the peaks of the two pulses' envelopes.

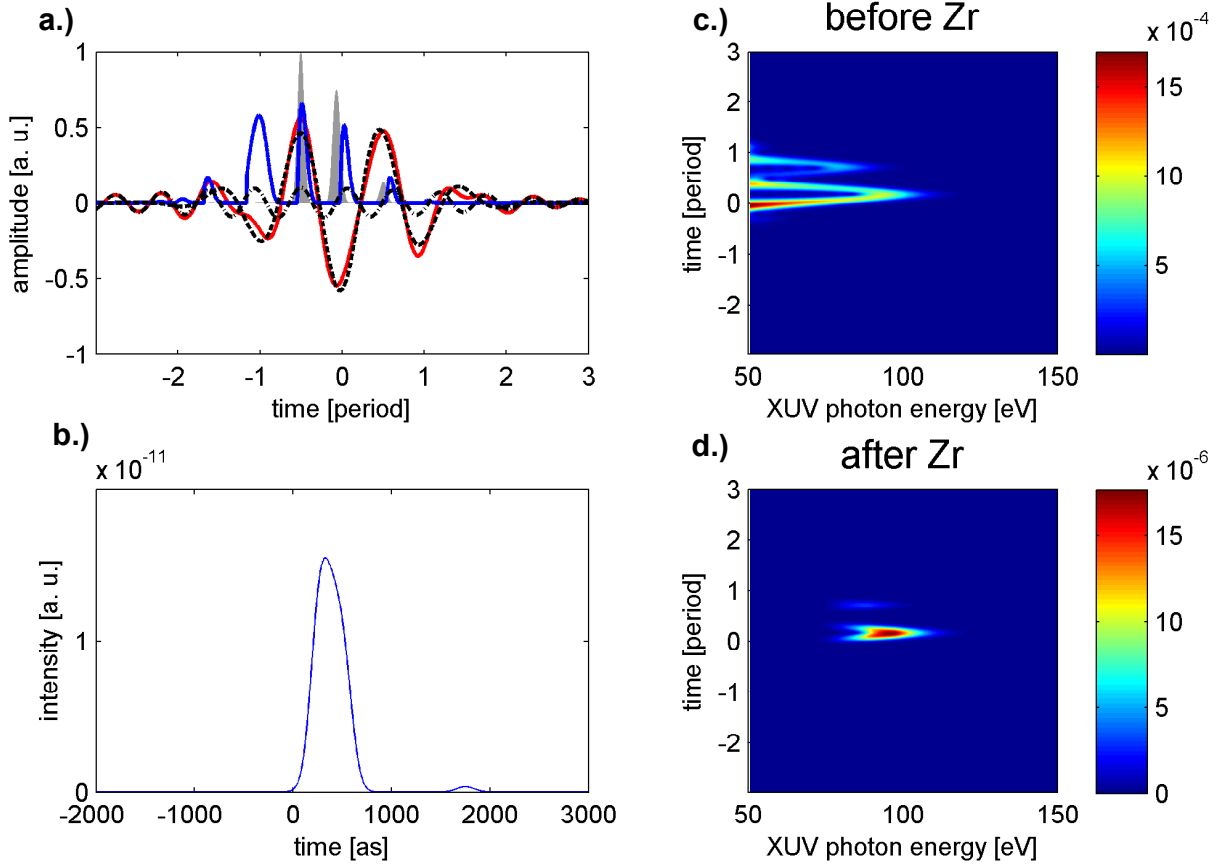


Figure 5.11: Time-frequency analysis. The time-delay between the fundamental and the SH here was 0.32 fs for a CEP=190°. The time-scan for this CEP is shown in Fig. 5.9. In a.) the waveform (red curve) is depicted, which is generated by the addition of a fundamental and an SH pulse (both shown as dashed curves). Ionization-rates using the ADK-rates are shown in grey, while blue indicates the emitted XUV radiation as a function of birth time. The purple and green filled circles highlight the half-cycle where the most energetic electrons are launched, and where they are subsequently accelerated, respectively. b.) Attosecond XUV time structure that was obtained by taking the inverse-Fourier-transform of the spectrum measured after the Zr filter. No dispersion compensation has been done. c.) and d.) show the time-frequency analysis before and after the Zr, respectively. This time-delay of 0.32 fs between the two harmonic laser pulses constitutes the start of the broad tunability-range.

delay, which is highlighted by a purple line in the scan. By changing the time-delay from this value we can see that the central energy of the continuum starts to increase. The fine tunability range is ≈ 10 eV, the interval in which we can maintain relatively the same XUV intensity. Surprisingly, almost no spectral modulation is present, which means that the attosecond pulse purity is very high (this term has been defined in section 2.4.3 of chapter 2), even higher than when we generated HHG with only the fundamental. If we vary Δt even further we get more tunability in a broader range. The end of this broad range in the scan has been indicated by the orange line, and this is the time-delay value

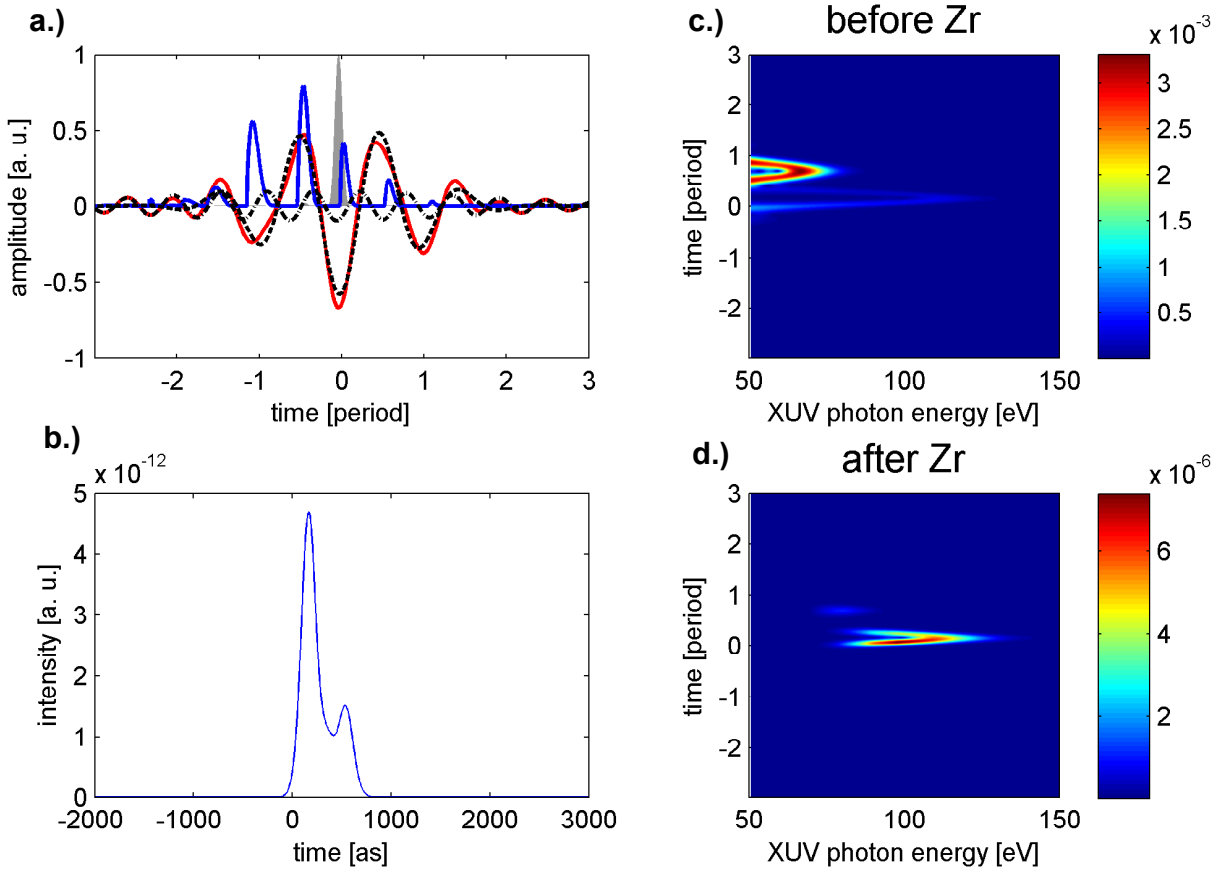


Figure 5.12: Time-frequency analysis. The time-delay between the fundamental and the SH here was 0.72 fs for a CEP=190°. The time-scan for this CEP is shown in Fig. 5.9. The color-coding and what a.), b.), c.) and d.) depict are the same as in Fig. 5.11.

where the spectral intensity of the continuum drops by a factor of ≈ 10 and where some small amount of spectral modulation in the low energies starts to appear (but not a higher amount than in the case that we claimed to be a continuum for HHG with fundamental only). The width of our broad tunability range is about 23 eV as can be seen directly from the plots. The cut-offs of the two spectral plots, which determine the width of the tunable range, were defined here as the energy where the spectral intensity reduces by 10% compared to the maximum. From looking at the spectrum with the high cut-off energy (orange line) it becomes also apparent that we have a dip in the spectrum at ≈ 110 eV. We will provide evidences that it is indicative of a slow modulation that can come only from an interference of short- and long-trajectories that are inside one half-cycle of the fundamental. Therefore, we can state that we have effectively switched off all the contributions of half-cycles other than the main one that creates our "quasi-continuum". To underscore this assertion and to get an understanding into why the cut-off shifts to higher energies, we performed further calculations based on [143]: Fig. 5.11 and 5.12 show

time-frequency analysis of the HHG process for two time-delays and one CEP-setting. The time-frequency plots were obtained by taking the Fourier-transform of the time-dependent atomic dipole using a Gaussian time-window, and then scanning this window with respect to time, similarly to [89]. The harmonic laser pulses, their superposition, the ionization rates and the recollision energies are depicted in a.), the time-frequency analysis in c.) and d.), and the time structure of the pulses appears in b.) (without dispersion compensation). The half-cycle (its peak highlighted by purple filled circle) that launches the electron that is accelerated to the highest kinetic energies in the subsequent half-cycle (highlighted by green filled circle) will give the maximum cut-off among all half-cycles. We see that when we increase Δt from 0.32 fs (Fig. 5.11) to 0.72 fs (Fig. 5.12) we see the effect of amplitude modulation, which was mentioned in section 5.2. This means now that the shift of the highest cut-off will happen because the accelerating half-cycle (highlighted by green filled circle) will increase going from 0.32 fs to 0.72 fs in time-delay. At the same time, this XUV burst will lose in intensity, because the launching half-cycle will become more and more suppressed, which will directly affect the ionization rate. These two effects explain why we have a gradual shift of the cut-off towards higher energies in the experiment at the expense of losing slowly the XUV intensity. In Fig. 5.11 two pulses result in the time domain, while interestingly in Fig. 5.11 a finer time structure is visible, which means that the pulse broke up into two. From the time-frequency analysis we see that two pulses emerge because of the two arms, the short- and long-trajectories of the highest energy XUV burst. Clearly, for this figure, some amount of trajectory selection happens, as well, in particular the short-trajectories are excited more. This will be discussed more in the last section.

For HHG with fundamental only the fine tunability range, as defined above, and achieved by changing the CEP, is almost non-existent. Regarding the availability of a broad tunability, it is ≈ 10 eV, that is when we still have a clear continuum, and only a small spectral modulation (relatively good single attosecond pulse purity).

Tunability for a two-color pulse was predicted and experimentally verified by Mansten et al [120]. However, in their case since they used a long fundamental pulse, they did not need phase-stabilization, and therefore they generated an attosecond pulse train. They demonstrated a tunability of the harmonic structure and not the continuum. Moreover, they had to create a 15% intensity ratio to get a tunability of 7 eV, while ours requires merely 2.7% and we reach a shift of more than 20 eV.

5.4.4 Comparison of isolated attosecond pulse purities

By recording an immense amount of spectra, we could select the best possible ones and make a comparison regarding the purity of isolated attosecond pulse generation with the

fundamental only and with SH added. Satellite pulses that emerge on the two sides of the main pulse are not desired in a pump-probe experiment. Waveform-synthesis helps to improve this purity parameter. The most pure attosecond pulse generation requires that the least amount of spectral modulation is present. It means that in the spectral domain only one half-cycle of the laser pulse contributes to the HHG in a certain energy range, where there is no modulation. The conditions in our comparison were identical (only the CEP and time-delay parameters were altered), therefore a relative change in terms of the modulation depth allowed us to draw reasonable conclusions. Fig. 5.13 shows two spectra, where the modulation depths for the respective cases were minimal. Interestingly, the most pure attosecond pulses are generated with the same intensities (no re-scaling was done) for both with fundamental only and with the SH added, and moreover their cut-offs are also very similar. However, a dramatic improvement is reached with our two-color synthesized waveform.

Attosecond streaking would be needed to gain quantitative insight into the level of isolated attosecond pulse generation [71]. Therefore, it would be very interesting to carry out streaking measurements. We can only surmise now that based on our results' similarity to those in [71] (see section 2.4.3 in chapter 2) and because we can see an apparent improvement with our two-color waveform, our satellite pulses had a relative intensity that was below 8% of the main pulse.

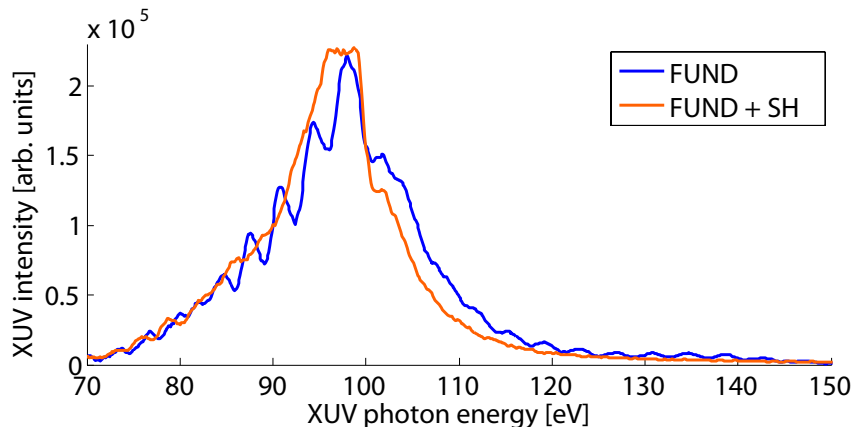


Figure 5.13: Comparison of HHG obtained by using the fundamental only and when the SH was added in terms of isolated attosecond pulse purity. For the case with the new waveform the spectral modulation significantly reduced, which means that less intense satellite pulses were generated. No scaling regarding the intensities was applied. The fundamental had a CEP=90°, and when the SH was added with a time-delay as shown by the purple line in Fig. 5.10 the CEP of the fundamental was adjusted to 190°.

Interference of 2 and 3 pulses

Experimentally, not all CEP and time-delay values lead to a quasi-continuum (no fast modulation observable spectrally). When a relatively long laser pulse generates harmonics, odd harmonics emerge. For short pulses, a symmetry breaking occurs, for example for a cosine-shaped pulse there is a half-cycle that stands out among all the others, and the harmonic structure will contain not only odd harmonics, and moreover they no longer stay fixed, but their position will be dependant on the CEP. It was found that they move because the relative dipole phase of the electrons that are traveling in the continuum in

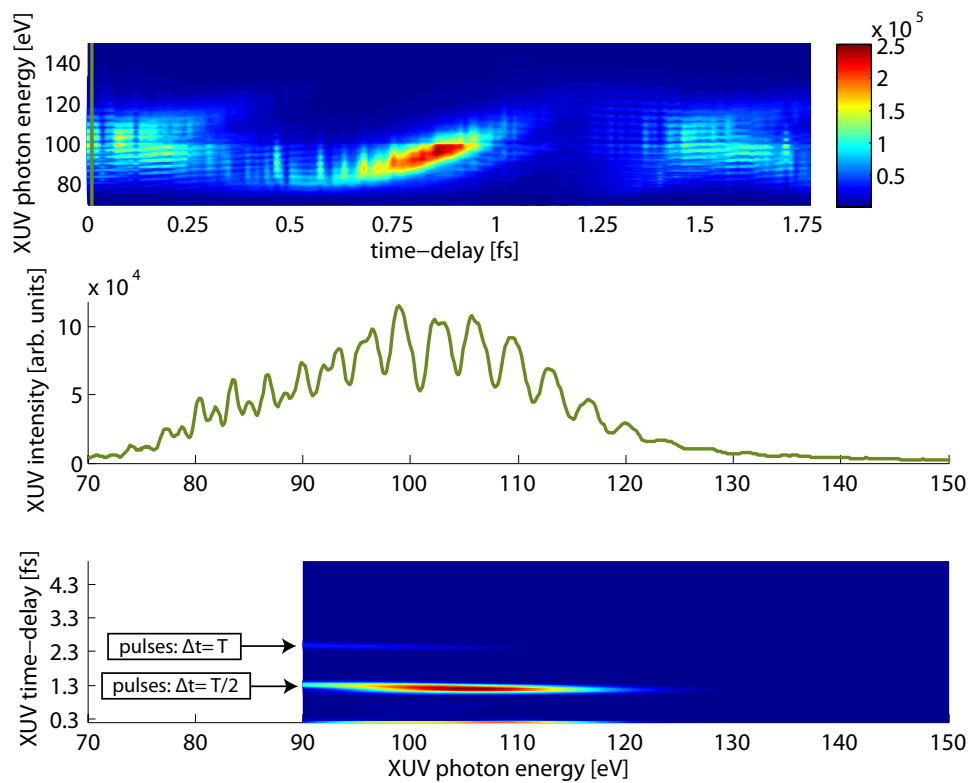


Figure 5.14: Interference of 2 or 3 pulses in different energy ranges. The CEP of the fundamental was 230° , so the time-scan is the same as the last plot in Fig. 5.9. The 'harmonic' structure is a result of the interference between pulses. A separation of two laser photon energies means that 2 XUV pulses interfere which are half-cycle away in time ($\Delta t=T/2$), while when more peaks appear with a distance of one laser photon energy, we have 3 pulses interfering. In the latter case the two outer pulses are one full cycle away from each other ($\Delta t=T$), which causes the dense peaks (with a distance of one photon energy). Our Fourier-analysis that supports this interpretation is shown in the bottom plot. Here the measured spectrum was inverse-Fourier-transformed by moving a Gaussian filter (BW=20 eV) across the spectrum to find out what temporal structure can cause such a spectral modulation.

consecutive half-cycles will change as a function of CEP. An alternative picture behind this observation exists that says that the central wavelength of the laser pulse will vary when the pulse duration approaches the single-cycle duration, which again causes a shift of the 'harmonic' structure [16]. This was realized first in numerical simulations [144] and later it was seen also in experiments [27]. Hence, the term 'harmonics' is no longer appropriate; however, we will still keep this convention to refer to the peaks this way. Another interesting effect is that the number of additional peaks is a result of multiple attosecond pulses interfering. Recently, a description of this spectral signature appearing in different energy bands was given in [145]. In our experiment, as opposed to the long pulses used in [145], we had maximum 3 pulses interfering, and this happened when the energy separation between the peaks was one laser photon energy. The more commonly occurring case of a separation of two laser photon energies is a characteristics of two pulses interfering. A spectrum where both kinds of interferences are visible is shown in Fig. 5.14.

We inverse-Fourier-transformed this spectrum to obtain information on the pulse separations, which result is also shown in the figure. When we created a time-delay these peaks that form fringes moved in energy, again demonstrating that they are not fixed at some integer multiple of the laser frequency. We noted above in section 5.4.3 that the cut-off shifts in energy because the half-cycle that creates that XUV burst increases or decreases in magnitude. It affects the fringes, as well. In chapter 2 section 2.4.1 we discussed how the dipole phase differs for short- and long-trajectories. Here in this context, the relative dipole phase of the pulses that interfere varies due to the intensity and spectral region dependence of the phase. In [145] a movement of the fringes was observed, but that happened due to the change of the CEP. Knowing the energy separation of the fringes thus allows us to constantly monitor the number of pulses that are generated.

5.4.5 Quantum path interference within a half-cycle

In section 5.4.3 we have briefly stated that the indentation in our spectrum can be explained by considering the interference of quantum paths inside one half-cycle. These are the short- and long-trajectories that were discussed in chapter 2. In Fig. 5.15 we show a spectrum where this dip is most pronounced, along with a Fourier-analysis of this spectrum that extracts the time separation between the attosecond pulses. We see that a separation of ≈ 300 as results and this value is comparable to the mean time-delay between the short- and long-path photon emissions. We presented in Fig. 2.6 of chapter 2 single-atom simulations that take into account both quantum paths and a similar slow modulation was observable there. However, experimentally with only the fundamental used we did not detect any sign of a slow modulation (Fig. 2.5), because of multiple reasons as described in chapter 2. During HHG with our synthesized waveform we had

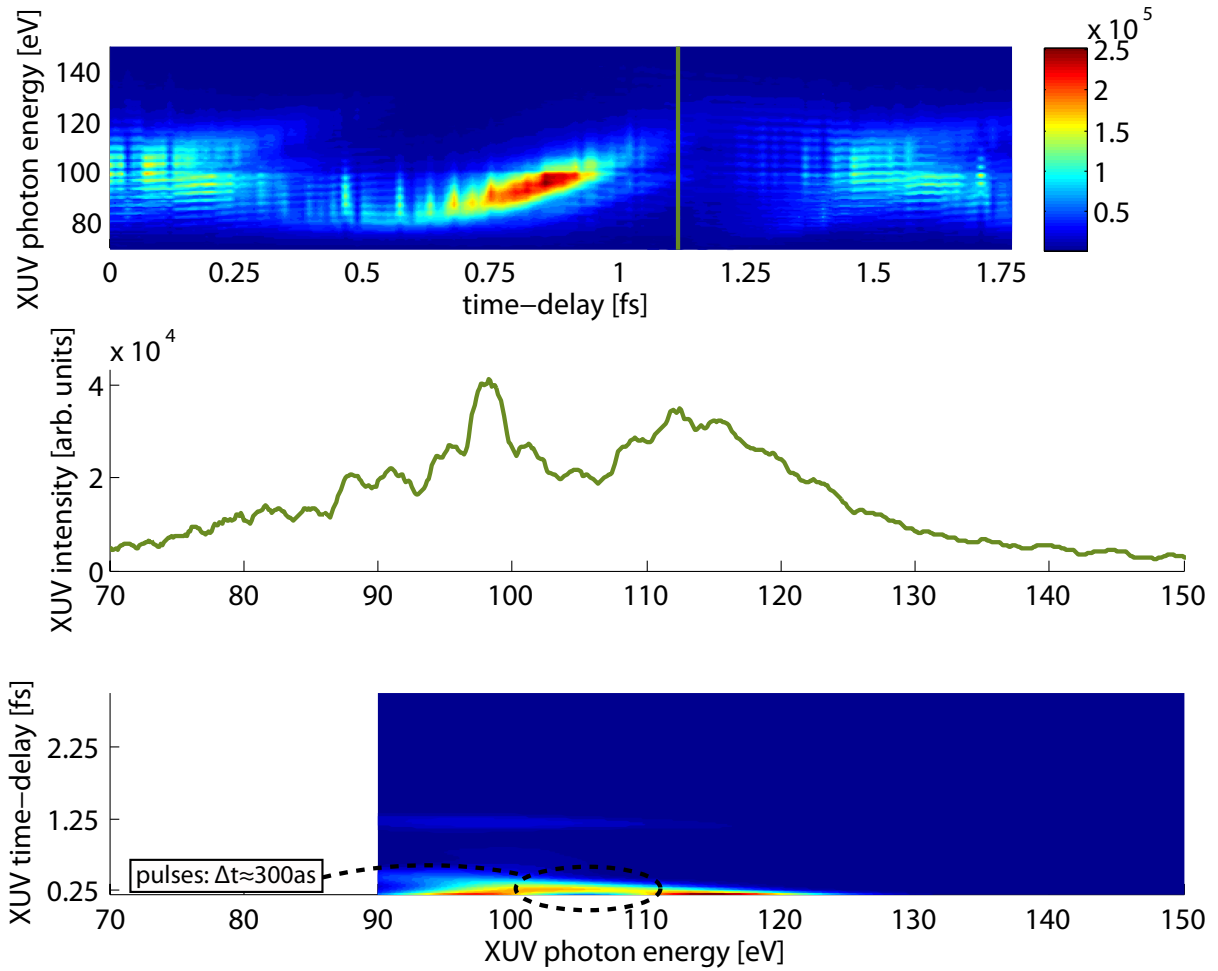


Figure 5.15: Quantum path interference inside one half-cycle of the laser pulse. The slow modulation in the frequency domain translates to a time separation of 300 as of the XUV pulses that have been created in the long and short arms of the XUV burst. Almost no fast modulation is visible, which means that we have switched off the contribution of all but one half-cycle to the XUV HHG spectrum. The CEP of the fundamental was 230° , the same as in Fig. 5.14.

a slow modulation both in the experimental and theoretical time-scans. The theoretical calculations of Fig. 5.9 reproduce remarkably well the peaks of the slow modulation in the spectrum that go parallelly to one another as a change of the time-delay. They shift again, similarly to the explanation in 5.4.4, because the dipole-phase of the two trajectories have a relative difference, which relative value changes when (now) the the time-delay is varied. Another point that supports this interpretation is that we have almost no fast modulation present both experimentally and theoretically in this energy region, which would otherwise indicate that the peaks are the result of some laser half-cycles. We saw in section 5.4.4 that such case would create a fast modulation. A perfect example for the latter to occur is the spectrum for a CEP= 135° in Fig. 2.7 of chapter 2.

Our experimental measurements are the first that show an interference in the plateau region that can be attributed to two quantum paths that are within a half-cycle of the laser pulse. It is present in all time-scans, though to different degrees. It is most discernible in the middle plot of Fig. 5.9. Its emergence is dependent on the time-delay for each CEP setting, therefore it is waveform-sensitive. Since the slow modulation is non-existent for HHG with the fundamental only, we believe, it is the addition of the SH that creates favorable conditions for its appearance. Long-trajectories are usually not excited efficiently when the HHG target is placed after the laser focus, therefore there must have been some level of quantum-path selection. Such selection either transfers more energy into long-trajectories, or for some waveforms these paths will be less affected by the intensity changes in a laser pulse that does not any more wash out their contributions. The mechanism connected to the long-trajectories' high sensitivity to intensity variations in a normal scenario with fundamental only was further discussed in chapter 2 of the thesis. Trajectory selection with the SH for a proper time-delay was shown to be viable in theory [116]. Short-trajectory's associated electrons are born close to the the peak of the laser, after a phase of $\approx 18^\circ$ (as discussed in 2.4), while the long-trajectory's are liberated before this phase value. By adding an SH to the fundamental with this SH wave's peak adding constructively with the fundamental and the two peaks being within a ≈ 100 as interval, we can change the ionization instant so that we excite mainly short- or long-trajectories. In simulations the maximum ratio between exciting one path or the other was about 1:1.5 in XUV intensity, a demonstrative example being Fig. 5.12. There, short-trajectory selection was realized. This might still not explain the appearance of the long-trajectories for some time-delay and CEP value. More advanced analysis, including using a 3D propagation model is currently on the way to find out the physical reasons for the emergence of the long-trajectories with the broadband two-color pulses.

5.5 Summary

In this chapter we have presented a scheme for the efficient extension of a near-one-octave bandwidth towards low wavelengths by frequency-converting a portion of the fundamental. To show the modification of the waveform we showed our new pulse's effect on HHG. Sub-fs tailoring of the wave allows us to enhance or suppress some chosen half-cycles that directly influence the XUV half-cycle cut-off energies.

Our two-color-based waveform-synthesis introduced tunability into the HHG process. Specifically, for some CEP settings just a change of the time-delay between the two harmonic laser pulses is enough to shift the quasi-continuum from a cut-off at 100 eV to 123 eV. During this tuning process the XUV intensity gradually lowers, and through

time-frequency analysis we showed that this happens because the half-cycle where the electrons are launched gets reduced in amplitude; as a result, the ionization will decrease. The appearance of a quasi-continuum indicates that we have efficiently switched off all the contributions of other half-cycles, except for one. This extinction of other half-cycles' effect is also manifest in the lack of a relatively strong spectral modulation when our two-color waveform is used as opposed to the case when only the fundamental is the driver laser pulse for HHG. We showed furthermore evidences for the existence of a quasi-continuum structure, instead of a pure continuum. It is the result of a quantum path interference of short- and long-trajectories inside one half-cycle of the fundamental laser field. We believe that a change in the phase-matching conditions could lead to a reduction of the long-trajectory contribution, which is necessary for the generation of an isolated attosecond pulse. It may lead then to the generation of tunable attosecond pulses with very little satellite pulses.

Chapter 6

Conclusions and outlook

In conclusion, three major areas of research were presented that are connected through the steps that are necessary prerequisites for attosecond science and more generally for strong-field physics. These stages are pulse generation and characterization. We generated pulses of a near mono-cycle duration that have a well-controlled evolution of the electrical field. We furthermore extended our tools for pulse generation by combining the already broad spectrum of our fundamental with its second-harmonic (SH) field, and it allowed us to modify the electrical field on a sub-cycle time-scale so that the pure sinusoidal time-evolution can be broken. This constitutes the first step towards waveform-synthesis and its ramifications in HHG were presented through spectral measurements. Furthermore, we characterized our consecutive pulses on a single-shot basis in terms of their CEP, which gives us access to the electrical field and with the highest demonstrated precision.

The area of few-cycle high intensity lasers is evolving rapidly. It belongs no longer to far-future dreams that soon multi-TW lasers with pulse durations close to two-cycles will become available [38]; three-cycles are already routinely produced in the lab [39]. They exploit Optical Parametric Chirped-pulse Amplification (OPCPA), a technique that makes systems scalable in energy and capable of supporting extreme amplification bandwidths. When focused, relativistic intensities can be reached. Surely, they are going to revolutionize not only strong-field science, but also in plasma physics for the first time few-cycle pulses will be on hand. In fact, merging the two areas allows us to carry out HHG on solid surfaces, which will let us reach several orders of higher conversion efficiencies than in gases and simultaneously an isolated attosecond pulse will emerge due to the pulses' few-cycle nature. An important step has been taken recently, whereby the harmonics emitted through Coherent Wake Emission (non-relativistic regime) from a solid target were shown to be phase-locked, which is a necessary condition for pulse-formation [146]. Entering the relativistic regime [147], on the other hand requires further improvements on the laser side, so that clean pulses with high contrast and with no post or pre-pulses can be gener-

ated that do not cause a pre-excitation of the plasma. Higher seed for the OPCPA [148], cross-polarized wave-generation (XPW) [149] and again reaching out to plasma physics by employing Plasma Mirrors (PM) [150] are a few possible methods of choice in this respect. The improvement in photon flux will be tangible also when these high energy pulses will be focused on a gas target (with loose focusing) to generate high-harmonic radiation, which will lead to new capabilities, such as the initiation of XUV-XUV pump-probe experiments due to the higher XUV flux. When focused more tightly, pushing out the position of the highest harmonics towards keV energies owing to the cut-off energies' linear dependence on the peak intensity will also be a major milestone. A multi-pronged approach is probably most sensible to reach this goal, because an extension of the cut-off towards higher energies is anticipated also by using a longer driving laser wavelength, so that the electron will have more time to gain energy during its excursion in the laser field. These infrared (IR) laser systems which again rely on the OPCPA concept [60] or on filamentation [151] are currently under development with already very encouraging first results.

As we know, ensuring a controlled electrical field shape for short pulses is critical. However, phase-stabilization of such high-intensity laser systems as mentioned above is challenging, because they typically exhibit more significant intensity and pulse duration fluctuations in comparison with laser systems that are in use today [21]. Our single-shot phase-meter is a promising candidate to provide a solution to this vexing problem. Since our method that we have presented in the thesis does not require any phase-stabilization, we can directly measure each shot's CEP. Such CEP-tagging relaxes on the need for phase-stabilization and without any further attempts to try to control the phase already now experiments can be performed close to or in the relativistic optics regime. We have to note that for an experiment that requires many shots with the same phase in order to obtain maximum count, it is still beneficial to have CEP-stabilization. We saw in chapter 4 that our phase-meter is sensitive to the pulse duration, too. By energy filtering the shots even if there is energy fluctuation, we will be able to tell all important parameters of a pulse, which in turn will allow us to control the phase in a feedback control circuit.

Our single-shot measurement results have even more general significance. Experiments related to HHG, ATI or terahertz emission can now be carried out with non-phase-stabilized lasers and by simple CEP tagging, the dependence of strong-field effects on the electromagnetic waveform can be reconstructed with very low phase jitter. In a short time by measuring a large number of pulses with random CEPs, we can effectively scan over all possible phase values. Gaining access to the CEP of a single laser shot will enable us for the first time to characterize the entire waveform of single ultrashort laser pulses using our apparatus along with well-established single-shot all-optical pulse characteriza-

tion techniques [152, 153]. Our device alone will actually be able to measure not only the CEP, but the pulse duration, as well, and uniquely with a precision that increases towards single-cycle pulses. As the ATI cut-off gives directly the peak intensity, we will be able to tell in one shot three of the most important parameters of a pulse: its CEP, duration and intensity. These powerful features of our CEP measurement have been recognized recently also by the community, and our method will be soon included in the well-known lecture series by Prof. Rick Trebino (Georgia Tech).

Once phase-stabilization becomes available for few-cycle high-intensity lasers, an effective way of approaching the same characteristics of the laser as that of a shorter pulse system is by using the two-color waveform-synthesis technique. For isolated attosecond pulse generation with laser pulses at 800 nm, two-cycle pulses are inevitable. When three-cycle pulses are available [39], the small, but measurable ATI phase-asymmetry might already enable one to realize phase-stabilization with a phase-meter. Consequently, by adding a small amount of SH with the right time-delay [105, 106] it would be possible to create the conditions for the emergence of a continuum, which is indicative of an isolated attosecond pulse. Our technique's applicability is not limited to such NIR systems, as it can be implemented also in other wavelength regions, such as in the IR.

We showed in this thesis that pulses approaching the single-cycle limit, combined with their SH enables us to introduce broad tunability of the continuum. Two quasi-continua were generated: one that is intense and lies low in energy, while the other one is shifted to higher energies, but has a lower intensity associated with it. Switching between them is possible by turning one knob, changing the time-delay between the two harmonic laser pulses. They are quasi-continua, because a slow-modulation in the continuum was visible that is a consequence of a trajectory interference (short and long) inside a half-cycle, which interference was observed for the first time with no special geometrical selection of trajectories. It is a CEP and time-dependent effect, in other words it appears only for some specific waveforms. Since we do not observe this slow modulation for HHG with fundamental only, this phenomenon can be attributed to the presence of the SH. Probably, if an isolated attosecond pulse is desired, by changing the phase-matching conditions it will be possible to eliminate one of the trajectories. Furthermore, we compared HHG with fundamental only and when an SH is added in terms of the spectral manifestation of the isolated attosecond pulse purity. We found that the HHG continuum is smoother with our two-color waveform than when only the fundamental is used and by inference a more pure isolated attosecond pulse may result in the time-domain.

Attosecond sampling [8] of our new waveform will complete waveform-synthesis and ultimate proof will be given to the sub-fs distortions of the wave due to the presence of the SH. Before this characterization, another way of obtaining useful information is the

usage of a device based on frequency-resolved optical gating (FROG) [154]. In our current experiment some parameters were experimentally unknown, and we could extract these only from theory. Such parameters were (i) the pulse duration of the SH, (ii) the amount of negative or positive chirp of the pulses, (iii) the time-delay between the fundamental and the SH in an absolute sense, that is the shift of their pulse peaks. Two versions of the FROG method are particularly well-suited for the measurement of very short light pulses, both in the NIR and UV spectral bands, and they are called Self-Diffraction and Transient-Grating FROG (SD- and TG-FROG) [154–156]. The latter is always phase-matched, while the former for appropriately thin crystals might work, as well.

Application of two laser pulses that are the harmonics of each other is exciting because the ionization step can be confined to one half-cycle of the laser pulse. If the time-delay is such that the electrical field peaks of each of the pulses totally overlap, constructive interference will happen, while for the neighboring half-cycles peak suppression will occur. Thus one ionization event will result for the increased peak, which is not repeated any more in time.

Ideally waveform-synthesis will combine a broad interval of colors, from UV to IR, so spectral ranges spanning multiple octaves. Setting the amplitude and phase of each frequency component will allow for arbitrarily tailored shapes for the driver field, and in turn will permit the manipulation of the generated attosecond pulses. Full control in such a broad spectral range, from XUV to IR will surely find many applications in strong-field science for investigations of processes that are relevant not only for physics, but also for biology and chemistry.

Appendix A

XUV transmission of common materials

For our HHG measurements we had to use various XUV filters. Zr was our material of choice for blocking the fundamental in order to eliminate the saturation of the CCD camera that we used for the spectral characterization of the XUV harmonics. The other two important filters were Si and Al that enabled us to perform a calibration of our measurements, since they have a well-defined, sharp transmission feature. As a result, two energy values became available (73 eV for Al and 100 eV for Si), which completely determined the scale for the energy as seen by the CCD camera, recorded after our grazing-incidence grating (from Hitachi). The plots below show the transmission of 150 nm thick filters for an energy range of 40-170 eV.

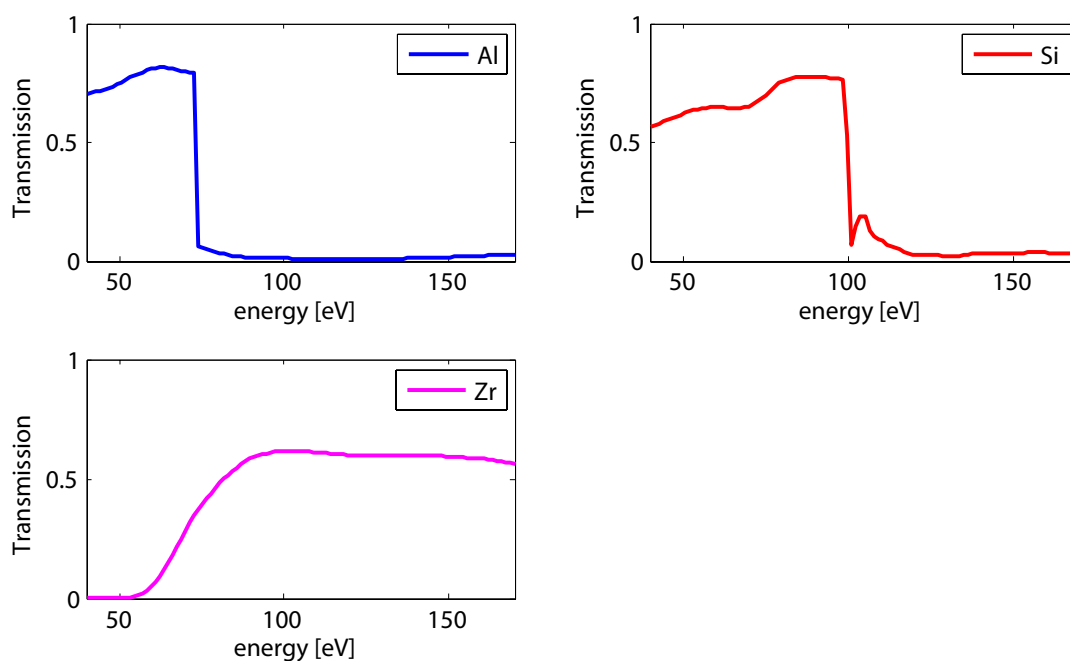


Figure A.1: Transmission of filters that we used during our HHG measurements.

Bibliography

- [1] K. Goda, K. K. Tsia and B. Jalali. *Serial time-encoded amplified imaging for real-time observation of fast dynamic phenomena*. Nature, **458**, 1145–1149 (2009).
- [2] T. H. Maiman. *Stimulated Optical Radiation in Ruby*. Nature, **187**, 493–494 (1960).
- [3] A. J. DeMaria, D. A. Stetser and H. Heynau. *Self mode-locking of lasers with saturable absorbers*. Appl. Phys. Lett., **8**(7), 174–176 (1966).
- [4] J. A. Armstrong, N. Bloembergen, J. Ducuing and P. S. Pershan. *Interactions between light waves in a nonlinear dielectric*. Phys. Rev., **127**, 1918 (1962).
- [5] A. H. Zewail. *Femtochemistry: Atomic-Scale Dynamics of the Chemical Bond*. The Journal of Physical Chemistry A, **104**(24), 5660–5694 (2000).
- [6] P. B. Corkum and F. Krausz. *Attosecond science*. Nat. Phys., **3**, 381–387 (2007).
- [7] R. Kienberger, E. Goulielmakis, M. Uiberacker, A. Baltuška, V. Yakovlev, F. Bammer, A. Scrinzi, T. Westerwalbesloh, U. Kleineberg, U. Heinzmann, M. Drescher and F. Krausz. *Atomic Transient Recorder*. Nature, **427**, 817–821 (2004).
- [8] E. Goulielmakis, M. Uiberacker, R. Kienberger, A. Baltuška, V. Yakovlev, A. Scrinzi, T. Westerwalbesloh, U. Kleineberg, U. Heinzmann, M. Drescher and F. Krausz. *Direct measurement of light waves*. Science, **305**, 1267–1269 (2004).
- [9] D. Bradley, B. Liddy and W. Sleat. *Direct linear measurement of ultrashort light pulses with a picosecond streak camera*. Optics Communications, **2**(8), 391–395 (1971).
- [10] M. Drescher, M. Hentschel, R. Kienberger, M. Uiberacker, V. Yakovlev, A. Scrinzi, T. Westerwalbesloh, U. Kleineberg, U. Heinzmann and F. Krausz. *Time-resolved atomic inner-shell spectroscopy*. Nature, **419**, 803–806 (2002).
- [11] M. Uiberacker, T. Uphues, M. Schultze, A. J. Verhoeef, V. S. Yakovlev, M. F. Kling, J. Rauschenberger, M. N. Kabachnik, H. Schröder, M. Lezius, K. L. Kompa, H.-G.

- Muller, M. J. J. Vrakking, S. Hendel, U. Kleineberg, U. Heinzmann, M. Drescher and F. Krausz. *Attosecond real-time observation of electron tunnelling in atoms*. Nature, **446**, 627–632 (2007).
- [12] A. L. Cavalieri, N. Müller, T. Uphues, V. S. Yakovlev, A. Baltuška, B. Horvath, B. Schmidt, L. Blümel, R. Holzwarth, S. Hendel, M. Drescher, U. Kleineberg, P. M. Eschenique, R. Kienberger, F. Krausz and U. Heinzmann. *Attosecond spectroscopy in condensed matter*. Nature, **449**, 1029–1032 (2007).
- [13] M. I. Stockman, M. F. Kling, U. Kleineberg and F. Krausz. *Attosecond nanoplasmonic-field microscope*. Nature Photonics, **1**, 539–544 (2007).
- [14] L. E. Hargrove, R. L. Fork and M. A. Pollack. *Locking of He–Ne laser modes induced by synchronous intracavity modulation*. Appl. Phys. Lett., **5**(1), 4–5 (1964).
- [15] W. E. Lamb. *Theory of an Optical Maser*. Phys. Rev., **134**(6A), A1429–A1450 (1964).
- [16] T. Brabec and F. Krausz. *Intense few-cycle laser fields: Frontiers of nonlinear optics*. Rev. Mod. Phys., **72**(2), 545–591 (2000).
- [17] G. Steinmeyer, D. H. Sutter, L. Gallmann, N. Matuschek and U. Keller. *Frontiers in Ultrashort Pulse Generation: Pushing the Limits in Linear and Nonlinear Optics*. Science, **286**(5444), 1507–1512 (1999).
- [18] T. Sudmeyer, S. V. Marchese, S. Hashimoto, C. R. E. Baer, G. Gingras, B. Witzel and U. Keller. *Femtosecond laser oscillators for high-field science*. Nature Photonics, **2**, 599–604 (2008).
- [19] C. S. F. K. R. Szipocs, K. Ferencz. *Chirped multilayer coatings for broadband dispersion control in femtosecond lasers*. Opt. Lett., **19**(3), 201 (1994).
- [20] M. Nisoli, S. D. Silvestri, O. Svelto, R. Szipöcs, K. Ferencz, C. Spielmann, S. Sartania and F. Krausz. *Compression of high-energy laser pulses below 5 fs*. Opt. Lett., **22**(8), 522–524 (1997).
- [21] A. L. Cavalieri, E. Goulielmakis, B. Horvath, W. Helml, M. Schultze, M. Fieß, V. Pervak, L. Veisz, V. S. Yakovlev, M. Uiberacker, A. Apolonski, F. Krausz, and R. Kienberger. *Intense 1.5-cycle near infrared laser waveforms and their use for the generation of ultra-broadband soft x-ray harmonic continua*. New J. Phys., **9**, 242 (2007).

- [22] M. Hentschel, R. Kienberger, C. Spielmann, G. A. Reider, N. Milosevic, T. Brabec, P. Corkum, U. Heinzmann, M. Drescher and F. Krausz. *Attosecond metrology*. Nature, **414**, 509–513 (2001).
- [23] G. Farkas and C. Tóth. *Proposal for attosecond light pulse generation using laser induced multiple-harmonic conversion processes in rare gases*. Phys. Lett. A, **168**(5–6), 447–450 (1992).
- [24] T. W. Hänsch. *A proposed sub-femtosecond pulse synthesizer using separate phase-locked laser oscillators*. Opt. Comm., **80**(1), 71–75 (1990).
- [25] R. Holzwarth, T. Udem, J. C. Hänsch, T. W. Knight, W. J. Wadsworth and P. S. J. Russell. *Optical Frequency Synthesizer for Precision Spectroscopy*. Phys. Rev. Lett., **85**, 2264 (2000).
- [26] D. J. Jones, S. A. Diddams, J. K. Ranka, A. Stentz, R. S. Windeler, J. L. Hall and S. T. Cundiff. *Carrier-Envelope Phase Control of Femtosecond Mode-Locked Lasers and Direct Optical Frequency Synthesis*. Science, **288**, 635–639 (2000).
- [27] A. Baltuška, Th. Udem, M. Uiberacker, M. Hentschel, E. Goulielmakis, Ch. Gohle, R. Holzwarth, V. S. Yakovlev, A. Scrinzi, T. W. Hänsch and F. Krausz. *Attosecond control of electronic processes by intense light fields*. nature, **421**, 611–615 (2003).
- [28] E. Goulielmakis, V. S. Yakovlev, A. L. Cavalieri, M. Uiberacker, V. Pervak, A. Apolonski, R. Kienberger, U. Kleineberg and F. Krausz. *Attosecond Control and Measurement: Lightwave Electronics*. Science, **317**(5839), 769–775 (2007).
- [29] T. Junno, K. Deppert, L. Montelius and L. Samuelson. *Controlled manipulation of nanoparticles with an atomic force microscope*. Appl. Phys. Lett., **66**(26), 3627–3629 (1995).
- [30] J. A. Stroscio and D. M. Eigler. *Atomic and Molecular Manipulation with the Scanning Tunneling Microscope*. Science, **254**, 1319–1326 (1991).
- [31] M. F. Kling, C. Siedschlag, A. J. Verhoef, J. I. Khan, M. Schultze, T. Uphues, Y. Ni, M. Uiberacker, M. Drescher, F. Krausz and M. J. J. Vrakking. *Control of Electron Localization in Molecular Dissociation*. Science, **312**, 246 (2006).
- [32] E. Goulielmakis, S. Koehler, B. Reiter, M. Schultze, A. J. Verhoef, E. E. Serebryanikov, A. M. Zheltikov and F. Krausz. *Ultrabroadband, coherent light source based on self-channeling of few-cycle pulses in helium*. Opt. Lett., **33**(13), 1407–1409 (2008).

- [33] V. Pervak, A. V. Tikhonravov, M. K. Trubetskov, S. Naumov, F. Krausz and A. Apolonskiy. *Ultrabroadband, coherent light source based on self-channeling of few-cycle pulses in helium*. App. Phys. B, **87**, 5 (2007).
- [34] G. G. Paulus, F. Grasbon, H. Walther, P. Villoresi, M. Nisoli, S. Stagira, E. Priori and S. De Silvestri. *Absolute-phase phenomena in photoionization with few-cycle laser pulses*. Nature, **414**, 182 (2001).
- [35] T. Wittmann, B. Horvath, W. Helml, M. G. Schätzel, X. Gu, A. L. Cavalieri, G. G. Paulus and R. Kienberger. *Single-shot carrier-envelope phase measurement of few-cycle laser pulses*. Nature Physics, **5**, 357–362 (2009).
- [36] G. G. Paulus, F. Lindner, H. Walther, A. Baltuška, E. Goulielmakis, M. Lezius and F. Krausz. *Measurement of the Phase of Few-Cycle Laser Pulses*. Phys. Rev. Lett., **91**, 253004 (2003).
- [37] F. Tavella, K. Schmid, N. Ishii, A. Marcinkevicius, L. Veisz and F. Krausz. *High-dynamic range pulse-contrast measurements of a broadband optical parametric chirped-pulse amplifier*. Appl. Phys. B, **51**(6), 753–756 (2005).
- [38] D. Herrmann, L. Veisz, R. Tautz, F. Tavella, K. Schmid, V. Pervak and F. Krausz. *Generation of sub-three-cycle, 16-TW light pulses using noncollinear optical parametric chirped-pulse amplification*. Submitted.
- [39] F. Tavella, Y. Nomura, L. Veisz, V. Pervak, A. Marcinkevičius and F. Krausz. *Dispersion management for a sub-10-fs, 10 TW optical parametric chirped-pulse amplifier*. Opt. Lett., **32**(15), 2227–2229.
- [40] C. G. R. Geddes, C. Toth, J. van Tilborg, E. Esarey, C. B. Schroeder, D. Bruhwiler, C. Nieter, J. Cary and W. P. Leemans. *High-quality electron beams from a laser wakefield accelerator using plasma-channel guiding*. Nature, **431**, 538–541 (2004).
- [41] K. Schmid, L. Veisz, F. Tavella, S. Benavides, R. Tautz, D. Herrmann, A. Buck, B. Hidding, A. Marcinkevicius, U. Schramm, M. Geissler, J. M. ter Vehn, D. Habs and F. Krausz. *Few-Cycle Laser-Driven Electron Acceleration*. Phys. Rev. Lett., **102**, 124801 (2009).
- [42] P. B. Corkum. *Plasma perspective on strong-field multiphoton ionization*. Phys. Rev. Lett., **71**(13), 1994–1997 (1993).
- [43] M. Lewenstein, P. Balcou, M. Ivanov, A. Lhuillier and P. Corkum. *Theory of high-harmonic generation by low-frequency laser fields*. Phys. Rev. A, **49**(3), 2117–2132 (1994).

- [44] L. Keldysh. *Ionization in a field of a strong electromagnetic wave*. Sov. Phys. JETP-USSR, **20**, 1307 (1965).
- [45] M. Ammosov, N. Delone and V. Krainov. *Tunnel ionization of complex atoms and atomic ions in a varying electromagnetic-field*. Sov. Phys. JETP-USSR, **91**, 2008 – 2013 (1986).
- [46] G. G. Paulus, W. Becker, W. Nicklich and H. Walther. *Rescattering effects in above-threshold ionization: a classical model*. Journal of Phys. B: Atomic, Molecular and Optical Physics, **27**(21), L703–L708 (1994).
- [47] P. Salières, A. L’Huillier and M. Lewenstein. *Coherence Control of High-Order Harmonics*. Phys. Rev. Lett., **74**(19), 3776–3779 (1995).
- [48] P. B. Corkum, N. H. Burnett and M. Y. Ivanov. *Subfemtosecond pulses*. Opt. Lett., **19**, 1870–1872 (1994).
- [49] Z. Chang. *Single attosecond pulse and xuv supercontinuum in the high-order harmonic plateau*. Phys. Rev. A, **70**(4), 043802 (2004).
- [50] P. Agostini, F. Fabre, G. Mainfray, G. Petite and N. K. Rahman. *Free-Free Transitions Following Six-Photon Ionization of Xenon Atoms*. Phys. Rev. Lett., **42**(17), 1127–1130 (1979).
- [51] G. G. Paulus, W. Nicklich, H. Xu, P. Lambropoulos and H. Walther. *Plateau in above threshold ionization spectra*. Phys. Rev. Lett, **72**, 2851 (1994).
- [52] G. G. Paulus and H. Walther. *The classical and the quantum face of above-threshold ionization*. In Atoms, Solids and Plasmas in Super-Intense Laser Fields (Batani D., Joachain, C.J., Martellucci, S. and Chester, A.N., Eds.), p. 285–300 (2001).
- [53] P. Dietrich, F. Krausz and P. B. Corkum. *Determining the absolute carrier phase of a few-cycle laser pulse*. Opt. Lett., **25**, 16–18 (2000).
- [54] D. B. Milošević, G. G. Paulus and W. Becker. *High-order above-threshold ionization with few-cycle pulse: a meter of the absolute phase*. Opt. Expr., **11**, 1418–1429 (2003).
- [55] S. Chelkowski and A. D. Bandrauk. *Asymmetries in strong-field photoionization by few-cycle laser pulse: Kinetic-energy spectra and semiclassical explanation of the asymmetries of fast and slow electrons*. Phys. Rev. A., **71**, 053815–053819 (2005).

- [56] G. G. Paulus, F. Lindner, D. B. Milošević and W. Becker. *Phase-Controlled Single-Cycle Strong-Field Photoionization*. Phys. Scripta, **T110**, 120 (2004).
- [57] A. McPherson, G. Gibson, H. Jara, U. Johann, T. Luk, I. McIntyre, K. Boyer and C. Rhodes. *Studies of multiphoton production of vacuum ultraviolet-radiation in the rare-gases*. J. Opt. Soc. Am. B, **4**, 595 – 601 (1987).
- [58] M. Ferray, A. L’Huillier, X. F. Li, L. A. Lompré, G. Mainfray and C. Manus. *Multiple-harmonic conversion of 1064 nm radiation in rare gases*. J. Phys. B: At. Mol. Opt. Phys, **21**, L31 (1988).
- [59] J. Seres, E. Seres, A. Verhoef, G. Tempea, C. Strelill, P. Wobrauschek, V. Yakovlev, A. Scrinzi, C. Spielmann and E. Krausz. *Source of coherent kiloelectronvolt X-rays*. Nature, **433**, 596–596 (2005).
- [60] X. Gu, G. Marcus, Y. Deng, T. Metzger, C. Teisset, N. Ishii, T. Fuji, A. Baltuška, R. Butkus, V. Pervak, H. Ishizuki, T. Taira, T. Kobayashi, R. Kienberger and F. Krausz. *“Generation of carrier-envelope-phase-stable 2-cycle 740-μJ pulses at 2.1-μm carrier wavelength*. Opt. Expr., **17**, 62 (2008).
- [61] A. Gordon and F. Kärtner. *Scaling of kev hgh photon yield with drive wavelength*. Opt. Expr., **13**, 2941–2947 (2005).
- [62] P. Colosimo, G. Doumy, C. I. Baga, J. Wheeler, C. Hauri, F. Catoire, J. Tate, R. Chirla, A. M. March, G. G. Paulus, H. G. Muller, P. Agostini and L. F. DiMauro. *Scaling strong-field interactions towards the classical limit*. Nat. Phys., **4**, 386–389 (2008).
- [63] V. S. Yakovlev, M. Ivanov and F. Krausz. *Enhanced phase-matching for generation of soft X-ray harmonics and attosecond pulses in atomic gases*. Opt. Expr., **15**, 15351—15364 (2007).
- [64] E. Gibson, A. Paul, N. Wagner, R. Tobey, D. Gaudiosi, S. Backus, I. Christov, A. Aquila, E. Gullikson, D. Attwood, M. Murnane and H. Kapteyn. *Coherent soft x-ray generation in the water window with quasi-phase matching*. Science, **302**, 95–98 (2003).
- [65] Ph. Antoine, A. L’Huillier and M. Lewenstein. *Attosecond Pulse Trains Using High-Order Harmonics*. **77**(7), 1234–1237 (1996).
- [66] P. M. Paul, E. S. Toma, P. Breger, G. Mullot, F. Audebert, P. Balcou, H. G. Muller and P. Agostini. *Observation of a train of attosecond pulses from high harmonic generation*. Science, **292**, 1689–1692 (2001).

- [67] M. Ivanov and F. Krausz. *Attosecond physics*. Rev. Mod. Phys., **81**, 163–234 (2009).
- [68] M. Nisoli, O. De Silvestri, Svelto, R. Szipocs, K. Ferencz, C. Spielmann, S. Sartania and F. Krausz. *Compression of high-energy laser pulses below 5 fs*. Opt. Lett., **22**, 522 (1997).
- [69] S. Sartania, Z. Cheng, M. Lenzner, G. Tempea, C. Spielmann, F. Krausz and K. Ferencz. *Generation of 0.1 TW 5 fs optical pulses at a 1 kHz repetition rate*. Opt. Lett., **22**(20), 1562–1564 (1997).
- [70] I. P. Christov, J. Zhou, J. Peatross, A. Rundquist, M. M. Murnane and H. C. Kapteyn. *Nonadiabatic Effects in High-Harmonic Generation with Ultrashort Pulses*. Phys. Rev. Lett., **77**(9), 1743–1746 (1996).
- [71] E. Goulielmakis, M. Schultze, M. Hofstetter, V. S. Yakovlev, J. Gagnon, M. Uiberacker, A. L. Aquila, E. M. Gullikson, D. T. Attwood, R. Kienberger, F. Krausz and U. Kleineberg. *Single-Cycle Nonlinear Optics*. Science, **320**, 1614–1617 (2008).
- [72] I. J. Sola, E. Mevel, L. Elouga, E. Constant, V. Strelkov, L. Poletto, P. Villoresi, E. Benedetti, J.-P. Caumes, S. Stagira, C. Vozzi, G. Sansone and M. Nisoli. *Controlling attosecond electron dynamics by phase-stabilized polarization gating*. Nat. Phys., **2**, 319–322 (2006).
- [73] G. Sansone, E. Benedetti, F. Calegari, C. Vozzi, L. Avaldi, R. Flammini, L. Poletto, P. Villoresi, C. Altucci, R. Velotta, S. Stagira, S. De Silvestri and M. Nisoli. *Isolated Single-Cycle Attosecond Pulses*. Science, **314**, 443–446 (2006).
- [74] C. A. Haworth, L. E. Chipperfield, J. S. Robinson, P. L. Knight, J. P. Marangos and J. W. G. Tisch. *Half-cycle cutoffs in harmonic spectra and robust carrier-envelope phase retrieval*. Nature Physics, **3**, 52–57 (2007).
- [75] S. Kim, J. Jin, Y. Kim, I. Park, Y. Kim and S. Kim. *High-harmonic generation by resonant plasmon field enhancement*. Nature, **757**, 153901 (2008).
- [76] C. Gohle, T. Udem, M. Herrmann, J. Rauschenberger, R. Holzwarth, H. A. Schuessler, F. Krausz and Hänsch, T. W. *A frequency comb in the extreme ultraviolet*. Nature, **436**, 234 (2005).
- [77] D. Strickland and G. Mourou. *Compression of amplified chirped optical pulses*. Opt. Commun., **56**(3), 219–221 (1985).

- [78] S. A. Planas, N. L. Pires Mansur, C. H. Brito Cruz and H. L. Fragnito. *Spectral narrowing in the propagation of chirped pulses in single-mode fibers*. Opt. Lett., **18**(9), 699–701 (1993).
- [79] M. Nisoli, G. Sansone, S. Stagira, V. C., S. De Silvestri and O. Svelto. *Ultra-broadband continuum generation by hollow-fiber cascading*. Appl. Phys. B, **75**, 601–604 (2002).
- [80] C. P. Hauri, W. Kornelis, F. W. Helbing, A. Heinrich, A. Couairon, A. Mysyrowicz, J. Biegert and U. Keller. *Generation of intense, carrier-envelope phase-locked few-cycle pulses through filamentation*. Appl. Phys. B., **79**, 673 (2004).
- [81] D. Meshulach, Y. Barad and Y. Silberberg. *Measurement of ultrashort optical pulses by third-harmonic generation*. J. Opt. Soc. Am. B, **14**(8), 2122–2125 (1997).
- [82] A. J. Verhoef, A. Fernández, M. Lezius, K. O’Keeffe, M. Uiberacker and F. Krausz. *Few-cycle carrier envelope phase dependent stereo detection of electrons*. Opt. Lett., **31**, 3520 (2006).
- [83] T. M. Fortier, P. A. Roos, D. J. Jones, S. T. Cundiff, R. D. R. Bhat and J. E. Sipe. *Carrier-Envelope Phase-Controlled Quantum Interference of Injected Photocurrents in Semiconductors*. Phys. Rev. Lett., **92**(14), 147403 (2004).
- [84] K. Osvay, M. Görbe, , C. Grebing and G. Steinmeyer. *Bandwidth-independent linear method for detection of the carrier-envelope offset phase*. Opt. Lett., **32**, 3095–3097 (2007).
- [85] H. R. Telle, G. Steinmeyer, A. E. Dunlop, J. Stenger, D. H. Sutter and U. Keller. *Carrier-envelope offset phase control: A novel concept for absolute optical frequency measurement and ultrashort pulse generation*. Appl. Phys. B, **69**, 327–332 (1999).
- [86] P. A. Roos, X. Li, R. P. Smith, P. J. A., T. M. Fortier and S. T. Cundiff. *Solid-state carrier-envelope phase stabilization via quantum interference control of injected photocurrents*. Opt. Lett., **30**, 735–737 (2005).
- [87] A. Apolonski, P. Dombi, G. G. Paulus, M. Kakehata, R. Holzwarth, T. Udem, C. Lemell, K. Torizuka, J. Burgdörfer, T. W. Hänsch and F. Krausz. *Observation of Light-Phase-Sensitive Photoemission from a Metal*. Phys. Rev. Lett, **92**, 073902 (2004).

- [88] M. Kieß, T. Löffler, M. D. Thomson, R. Dörner, H. Gimpel, K. Zrost, T. Ergler, R. Moshhammer, U. Morgner, J. Ullrich and H. Roskos. *Determination of the carrier-envelope phase of few-cycle laser pulses with terahertz-emission spectroscopy*. Nature Physics, **2**, 327 (2006).
- [89] V. S. Yakovlev and A. Scrinzi. *High Harmonic Imaging of Few-Cycle Laser Pulses*. Phys. Rev. Lett., **91**, 153901 (2003).
- [90] M. F. Kling, J. Rauschenberger, A. J. Verhoef, E. Hasovic, T. Uphues, D. B. Milošević, H. G. Muller and M. J. J. Vrakking. *Imaging of carrier-envelope phase effects in above-threshold ionization with intense few-cycle laser fields*. New Journal of Physics, **10**, 025024 (2008).
- [91] P. Lan, P. Lu, F. Li, Y. Li and Z. Yang. *Carrier-envelope phase measurement from half-cycle high harmonics*. Opt. Expr., **16**, 5868–5873 (2008).
- [92] M. Mehendale, S. A. Mitchell, J. P. Likforman, D. M. Villeneuve and P. B. Corkum. *Method for single-shot measurement of the carrier envelope phase of a few-cycle laser pulse*. Opt. Lett., **25**, 1672–1674 (2000).
- [93] M. Kakehata, H. Takada, Y. Kobayashi, K. Torizuka, Y. Fujihira, T. Homma and H. Takahashi. *Single-shot measurement of carrier-envelope phase changes by spectral interferometry*. Opt. Lett., **26**, 1432–1438 (2001).
- [94] C. M. Kim and C. H. Nam. *Selection of an electron path of high-order harmonic generation in a two-color femtosecond laser field*. J. Phys. B., **39**, 3199–3209 (2006).
- [95] D. B. Milosevič and W. Becker. *Attosecond pulse trains with unusual nonlinear polarization*. Phys. Rev. A., **62**, 011403 (2000).
- [96] P. Dombi, A. Apolonski, Lemell, G. G. Paulus, M. Kakehata, R. Holzwarth, T. Udem, K. Torizuka, J. Burgdörfer, T. W. Hänsch and F. Krausz. *Direct measurement and analysis of the carrier-envelope phase in light pulses approaching the single-cycle regime*. New Journal of Physics, **6**, 39 (2004).
- [97] C. Li, E. Moon, H. Wang, H. Mashiko, C. M. Nakamura, J. Tackett and Z. Chang. *Determining the phase-energy coupling coefficient in carrier-envelope phase measurements*. Opt. Lett., **32**, 796–798 (2007).
- [98] S. Witte, R. T. Zinkstok, W. Hogervorst and K. S. E. Eikema. *Control and precise measurement of carrier-envelope phase dynamics*. Appl. Phys. B., **78**, 5–12 (2004).

- [99] J. Rauschenberger, T. Fuji, M. Hentschel, A.-J. Verhoef, T. Udem, C. Gohle, T. W. Hänsch and F. Krausz. *Carrier-envelope phase-stabilized amplifier system*. *Laser Phys. Lett.*, **3**, 37–42 (2006).
- [100] J. D. Kane and R. Trebino. *Characterization of Arbitrary Femtosecond Pulses Using Frequency-Resolved Optical Gating*. *IEEE J. Quant. Electr.*, **29**, 571 (1993).
- [101] C. Iaconis and I. A. Walmsley. *Spectral phase interferometry for direct electric-field reconstruction of ultrashort optical pulses*. *Opt. Lett.*, **23**, 792 (1998).
- [102] A. Baltuška, M. S. Pshenichnikov and D. A. Wiersma. *Second-Harmonic Generation Frequency-Resolved Optical Gating in the Single-Cycle Regime*. *IEEE J. Quant. Electr.*, **35**, 459 (1999).
- [103] T. Morishita, A. Le, Z. Chen and C. D. Lin. *Accurate Retrieval of Structural Information from Laser-Induced Photoelectron and High-Order Harmonic Spectra by Few-Cycle Laser Pulses*. *Phys. Rev. Lett.*, **100**(1), 013903 (2008).
- [104] Y. Mairesse, A. d. Bohan, L. J. Frasinski, H. Merdji, L. C. Dinu, P. Monchicourt, P. Breger, M. Kovačev, R. Taïeb, B. Carrè, H. G. Muller, P. Agostini and P. Salières. *Attosecond Synchronization of High-Harmonic Soft X-rays*. *Science*, **302**, 1540 (2003).
- [105] T. Pfeifer, L. Gallmann, M. J. Abel, D. M. Neumark and S. R. Leone. *Single attosecond pulse generation in the multicycle-driver regime by adding a weak second-harmonic field*. *Opt. Lett.*, **31**, 975–977 (2006).
- [106] Y. Oishi, M. Kaku, A. Suda, F. Kannari and K. Midorikawa. *Generation of extreme ultraviolet continuum radiation driven by a sub-10-fs two-color field*. *Opt. Expr.*, **14**, 7230–7237 (2006).
- [107] P. Lan, P. Lu, W. Cao, Y. Li and X. Wang. *Attosecond ionization gating for isolated attosecond electron wave packet and broadband attosecond xuv pulses*. *Phys. Rev. A*, **76**, 051801 (2007).
- [108] B. Kim, J. Ahn, Y. Yu, Y. Cheng, Z. Xu and D. E. Kim. *Optimization of multi-cycle two-color laser fields for the generation of an isolated attosecond pulse*. *Opt. Expr.*, **16**, 10331–10340 (2008).
- [109] Z. Zeng, Y. Leng, R. Li and Z. Xu. *Electron quantum path tuning and isolated attosecond pulse emission driven by a waveform-controlled multi-cycle laser field*. *J. Phys. B*, **41**, 215601 (2008).

- [110] W. Hong, P. Lu, P. Lan, Q. Li, Q. Zhang, Z. Yang and X. Wang. *Method to generate directly a broadband isolated attosecond pulse with stable pulse duration and high signal-to-noise ratio*. Phys. Rev. A, **78**, 063407 (2008).
- [111] D. B. Milošević and W. Sandner. *Extreme-ultraviolet harmonic generation near 13 nm with a two-color elliptically polarized laser field*. Opt. Lett., **25**, 1532 (2000).
- [112] T. Pfeifer, L. Gallmann, M. J. Abel, P. M. Nagel, D. M. Neumark and S. R. Leone. *Heterodyne Mixing of Laser Fields for Temporal Gating of High-Order Harmonic Generation*. Phys. Rev. Lett., **97**, 163901 (2006).
- [113] W. Cao, P. Lu, P. Lan, X. Wang and G. Yang. *Efficient isolated attosecond pulse generation from a multi-cycle two-color laser field*. Opt. Expr., **15**, 530 (2006).
- [114] Z. Zheng, Y. Cheng, X. Song, R. Li and Z. Xu. *Generation of an Extreme Ultraviolet Supercontinuum in a Two-Color Laser Field*. Phys. Rev. Lett., **98**, 203901 (2007).
- [115] Z. Zhen and X. Liu. *Extension of the high-order harmonics and an isolated sub-100 as pulse generation in a two-colour laser field*. J. Phys. B, **41**, 125602 (2008).
- [116] X. Song, Z. Zeng, Y. Fu, B. Cai, R. Li, Y. Cheng and Z. Xu. *Quantum path control in few-optical-cycle regime*. Phys. Rev. A, **76**, 043830 (2007).
- [117] H. Merdji, T. Auguste, W. Boutu, J.-P. Caumes, B. Carré, T. Pfeifer, A. Jullien, D. M. Neumark and S. R. Leone. *Isolated attosecond pulses using a detuned second-harmonic field*. Opt. Lett., **32**, 3134 (2007).
- [118] Y. Zheng, Z. Zeng, X. Li, X. Chen, P. Liu, H. Xiong, H. Hui Lu, Z. S., P. Wei, L. Zhang, Z. Wang, J. Liu, Y. Cheng, R. Li and Z. Xu. *Enhancement and broadening of extreme ultraviolet supercontinuum in a relative phase controlled two-color laser field*. Opt. Lett., **33**, 234–236 (2008).
- [119] J. Mauritsson, P. Johnsson, E. Gustafsson, A. L’Huillier, K. J. Schafer and M. B. Gaarde. *Attosecond Pulse Trains Generated Using Two Color Laser Fields*. Phys. Rev. Lett., **97**, 013001 (2006).
- [120] E. Mansten, J. M. Dahlström, P. Johnsson, M. Swoboda, A. L’Huillier and J. Mauritsson. *Spectral shaping of attosecond pulses using two-colour laser fields*. New Journal of Phys., **10**, 083041 (2008).
- [121] N. Ishii, A. Kosuge, T. Hayashi, J. Kanai, T. Itatani, S. Adachi and S. Watanabe. *Quantum path selection in high-harmonic generation by a phase-locked two-color field*. Opt. Expr., **16**, 20876–20883 (2008).

- [122] W. Hong, Y. Li, P. Lu, P. Lan, Q. Zhang and X. Wang. *Control of quantum paths in the multicycle regime and efficient broadband attosecond pulse generation*. J. Opt. Soc. Am. B, **25**, 1684–1688 (2008).
- [123] I. J. Kim, G. H. Lee, S. B. Park, Y. S. Lee, T. K. Kim and C. H. Nam. *Generation of submicrojoule high harmonics using a long gas jet in a two-color laser field*. Appl. Phys. Lett., **92**, 021125 (2008).
- [124] C. F. d. M. Faria, D. B. Milošević and G. G. Paulus. *Phase-dependent effects in bichromatic high-order harmonic generation*. Phys. Rev. A, **61**, 063415 (2000).
- [125] I. J. Kim, C. M. Kim, H. T. Kim, G. H. Lee, Y. S. Lee, J. Y. Park, D. J. Cho and C. H. Nam. *Highly Efficient High-Harmonic Generation in an Orthogonally Polarized Two-Color Laser Field*. Phys. Rev. Lett., **94**, 243901 (2005).
- [126] K. Kondo, Y. Kobayashi, A. Sagisaka, Y. Nabekawa and S. Watanabe. *Tunneling ionization and harmonic generation in two-color fields*. J. Opt. Soc. Am. B, **13**, 424 (1996).
- [127] T. T. Liu, T. Kanai, T. Sekikawa and S. Watanabe. *Significant enhancement of high-order harmonics below 10 nm in a two-color laser field*. Phys. Rev. A, **73**, 063823 (2006).
- [128] U. Andiel, G. D. Tsakiris, E. Cormier and K. Witte. *High-order harmonic amplitude modulation in two-colour phase-controlled frequency mixing*. Europhys. Lett., **47**, 42–48 (1999).
- [129] H. G. Muller, P. H. Bucksbaum, D. W. Schumacher and A. Zavriyev. *Above-threshold ionisation with a two-colour laser field*. J. Phys. B, **23**, 2761–2769 (1990).
- [130] Y.-Y. Yin, C. Chen, D. S. Elliott and A. V. Smith. *Asymmetric photoelectron angular distributions from interfering photoionization processes*. Phys. Rev. Lett., **69**, 2353–2356 (1992).
- [131] D. W. Schumacher, F. Weihe, H. G. Muller and P. H. Bucksbaum. *Phase Dependence of Intense Field Ionization: A Study Using Two Colors*. Phys. Rev. Lett., **73**, 1344–1347 (1994).
- [132] G. G. Paulus, W. Becker and H. Walther. *Classical rescattering effects in two-color above-threshold ionization*. Phys. Rev. A, **52**, 4043–4053 (1995).
- [133] K. J. Schafer and K. C. Kulander. *Phase-dependent effects in multiphoton ionization induced by a laser field and its second harmonic*. Phys. Rev. A, **45**, 8026–8033 (1992).

- [134] H. Mashiko, S. Gilbertson, C. Li, S. D. Khan, M. M. Shakya, E. Moon and Z. Chang. *Double Optical Gating of High-Order Harmonic Generation with Carrier-Envelope Phase Stabilized Lasers*. Phys. Rev. Lett., **100**(10), 103906 (2008).
- [135] Z. Zeng, Y. Cheng, X. Song, R. Li and Z. Xu. *Generation of an Extreme Ultraviolet Supercontinuum in a Two-Color Laser Field*. Physical Review Letters, **98**(20), 203901 (2007).
- [136] D. Charalambidis, P. Tzallas, E. P. Benis, E. Skantzakis, G. Maravelias, L. A. A. Nikolopoulos, A. P. Conde and G. D. Tsakiris. *Exploring intense attosecond pulses*. New Journal of Physics, **10**, 025018 (17pp) (2008).
- [137] N. Dudovich, O. Smirnova, J. Levesque, Y. Mairesse, M. Y. Ivanov, D. M. Villeneuve and P. B. Corkum. *Measuring and controlling the birth of attosecond XUV pulses*. Nat. Phys., **2**, 781–786 (2006).
- [138] P. Baum, S. Lochbrunner and E. Riedle. *Generation of tunable 7-fs ultraviolet pulses: achromatic phase matching and chirp management*. Appl. Phys. B, **79**, 1027–1032 (2004).
- [139] B. E. A. Saleh and M. C. Teich. *Fundamentals of Photonics*. John Wiley and Sons, Inc. (1991).
- [140] L. Gallmann, G. Steinmeyer, U. Keller, G. Imeshev, M. M. Fejer and J.-P. Meyn. *Generation of sub-6-fs blue pulses by frequency doubling with quasi-phase-matching gratings*. Opt. Lett., **26**, 614–616 (2001).
- [141] L. Gallmann, G. Steinmeyer, G. Imeshev, J.-P. Meyn, M. M. Fejer and U. Keller. *Sub-6-fs blue pulses generated by quasi-phase-matching second-harmonic generation pulse compression*. Appl. Phys. B, **74**, 237–243 (2002).
- [142] K. Lizuka. *Elements of Photonics*. John Wiley and Sons, Inc. (2002).
- [143] X.-M. Tong and S.-I. Chu. *Probing the spectral and temporal structures of high-order harmonic generation in intense laser pulses*. Physical Rev. A, **61**, 021802 R! (2000).
- [144] E. Priori, G. Cerullo, M. Nisoli, S. Stagira, S. De Silvestri, P. Villoresi, L. Poletto, P. Ceccherini, C. Altucci, R. Bruzzese and C. de Lisio. *Nonadiabatic three-dimensional model of high-order harmonic generation in the few-optical-cycle regime*. Phys. Rev. A, **61**(6), 063801 (2000).

- [145] E. Mansten, J. M. Dahlström, J. Mauritsson, T. Ruchon, A. L’Huillier, J. Tate, M. B. Gaarde, P. Eckle, A. Guandalini, M. Holler, F. Schapper, L. Gallmann and U. Keller. *Spectral Signature of Short Attosecond Pulse Trains*. Physical Review Letters, **102**(8) (2009).
- [146] Y. Nomura, R. Horlein, P. Tzallas, B. Dromey, S. Rykovanov, Z. Major, J. Osterhoff, S. Karsch, L. Veisz, M. Zepf, D. Charalambidis, F. Krausz and G. D. Tsakiris. *Attosecond phase locking of harmonics emitted from laser-produced plasmas*. Nature Physics, **5**, 124–128 (2009).
- [147] B. Dromey, M. Zepf, A. Gopal, K. Lancaster, M. S. Wei, K. Krushelnick, M. Tatarakis, N. Vakakis, S. Moustazis, R. Kodama, M. Tampo, C. Stoeckl, R. Clarke, H. Habara, D. Neely, S. Karsch and P. Norreys. *High harmonic generation in the relativistic limit*. Nature Physics, **2**, 456–459 (2006).
- [148] F. Tavella, T. Wittmann, K. Schmid, B. Horvath, A. Cavalieri, L. Veisz, A. Marcinkevicius and F. Krausz. *Stronger seed for a multiterawatt few-cycle pulse OPCPA*. CLEO Europe Postdeadline, p. 1 (2007).
- [149] A. Jullien, O. Albert, G. Chériaux, J. Etchepare, S. Kourtev, N. Minkovski and S. M. Saltiel. *A two crystal arrangement to fight efficiency saturation in cross-polarized wave generation*. Opt. Expr., **14**(7), 2760–2769 (2006).
- [150] C. Thaury, F. Quere, J.-P. Geindre, A. Levy, T. Ceccotti, P. Monot, M. Bougeard, F. Reau, P. d’Oliveira, P. Audebert, R. Marjoribanks and P. Martin. *Plasma mirrors for ultrahigh-intensity optics*. Nature Physics, **3**, 424–429 (2007).
- [151] C. P. Hauri, R. B. Lopez-Martens, C. I. Blaga, K. D. Schultz, J. Cryan, R. Chirla, P. Colosimo, G. Doumy, A. M. March, C. Roedig, E. Sistrunk, J. Tate, J. Wheeler, L. F. DiMauro and E. P. Power. *Intense self-compressed, self-phase-stabilized few-cycle pulses at 2 μm from an optical filament*. Opt. Lett., **32**(7), 868–870 (2007).
- [152] W. Kornelis, J. Biegert, J. W. G. Tisch, M. Nisoli, G. Sansone, C. Vozzi, S. De Silvestri and U. Keller. *Single-shot kilohertz characterization of ultrashort pulses by spectral phase interferometry for direct electric-field reconstruction*. Opt. Lett., **28**, 281–283 (2003).
- [153] D. J. Kane and R. Trebino. *Single-shot measurement of the intensity and phase of an arbitrary ultrashort pulse by using frequency-resolved optical gating*. Opt. Lett., **18**, 823 (1993).

-
- [154] R. Trebino, K. W. DeLong, D. N. Fittinghoff, J. N. Sweetser, M. A. Krumbügel, B. A. Richman and D. J. Kane. *Measuring ultrashort laser pulses in the time-frequency domain using frequency-resolved optical gating*. Rev. of Sci. Instr., **68**(9), 3277–3295 (1997).
- [155] U. Graf, M. Fieß, M. Schultze, R. Kienberger, F. Krausz and E. Goulielmakis. *Intense few-cycle light pulses in the deep ultraviolet*. Opt. Express, **16**(23), 18956–18963 (2008).
- [156] M. Li, J. P. Nibarger, C. Guo and G. N. Gibson. *Dispersion-free Transient-grating Frequency-resolved Optical Gating*. Appl. Opt., **38**(24), 5250–5253 (1999).

Acknowledgements

Here I would like to say thank you to all the people who supported me both scientifically and also on a personal level during my Ph.D. studies at MPQ.

First of all, I would like to thank Prof. Ferenc Krausz for giving me the chance to work in his group. The international atmosphere and colleagues with various backgrounds provided a stimulating environment. Moreover, I thank him for the ideal conditions in the laboratories, and his continuous support during my work.

I would like to thank Reinhard Kienberger for his support and for helping me whenever I had problems.

I am thankful to Prof. Wolfgang Zinth for accepting to be the second reviewer of this thesis.

Thank you also to Bettina Schütz, Frau Wild, Karin Fröschl for the support at MPQ.

I am indebted to Ya Cheng and his group for carrying out calculations.

I thank Tibor Wittmann for the scientific and not so scientific discussions, for the innovative work that kept me going even when there was no clear sight of success. I am indebted to Markus Fieß for supporting me during experiments, and for letting himself and me stay "only" until as long as still sensible. His precise attitude is exemplary. I am thankful to Justin Gagnon not only for his unique criticism when reading through parts of this thesis, but also for his creative insights and colorful discussions. Thanks to Daniel Herrmann, whose excitement about physics and all other areas of life is unrivalled. I also thank Franz Tavella for sharing the cleanroom with me and his positive attitude, hard work were inspiring. I am also grateful to Vladislav Yakovlev for the nice discussions and for sharing office-space with me. Thanks, moreover to Wolfram Helml, with whom it was a pleasure to work with in the cleanroom. I am also thankful to Xun Gu, for his friendly and optimistic attitude and for the scientific discussions.

I would like to say thank you also to: Martin Centurion, Yutaka Nomura, Tom Metzger, Yunpei Deng, Karl Schmid, Elisabeth Magerl, Adrian Cavalieri, Takao Fuji, László Veisz, Matthias Kling, Zsuzsanna Major, Kyriaki Kosma, Jens Rauschenberger, Martin Schultze, Atsushi Sugita, and the others in our group and at MPQ.

Lastly, but not the least I thank my family for their 24-hour encouragement.

Curriculum vitae

Contact information

Name Bálint Horváth
Address Schleissheimerstraße 188
80797 München
Germany
Phone +49 (89) 15771729879 mobile
+49 (89) 30005539 home
E-mail balint.horvath@mpq.mpg.de



Personal data

Date and place of birth July 30, 1979 in Salgótarján, Hungary
Citizenship Hungarian **Gender** male

Academic experience and education

Max-Planck-Institut für Quantenoptik in Garching, Germany **09/2004-present**
and **Ludwig-Maximilians-Universität München**, Germany

Doctoral candidate in physics, May 2009

- Dissertation title: “Generation, characterization and sub-cycle shaping of intense, few-cycle light waveforms for attosecond spectroscopy”
- Supervisor: Prof. Dr. Ferenc Krausz

Budapest University of Technology and Economics, Hungary **09/1998-06/2004**
Master of Science in Electrical Engineering, awarded in June 2004

- Thesis title: “Enhanced Performance of the Photonic Oscillator and its Miniaturization by Integrated Optics”
- Supervisor: Prof. Dr. Tibor Bercei
- Major: Microwave Engineering; Minor: Optical Communications

Clemson University, U.S.A. **09/2001-02/2002**

Exchange student as Electrical Engineering student

- Graduate Design Project: Design of a low-noise Dielectric Resonator Oscillator

János Bolyai High School, Salgótarján, Hungary **07/1994-05/1998**

High School Diploma with highest honors, awarded in May 1998

- Advanced level in mathematics, physics and English

Honors

Support from Stanford University to attend SPRC Annual Meeting **09/2007**

Marie Curie “Early Career Researcher” under XTRA network **2004-2005**

Best M.Sc. thesis awards from Siemens and **2004**

Foundation for the Advancement of the Industry in Hungary

Besser Associates (Mountain View, CA, USA) Scholarship **2003**

Scholarship of the Republic of Hungary **2003-2004**

IEEE MTT-S Undergra/Pre-grad Scholarship **2003-2004**

Memberships

Optical Society of America (OSA) Student member **since 2005-present**

Institute of Electrical and Electronics Engineers (IEEE) **2003-2005**

Additional professional experience

**Christian Doppler Laboratory of Surface Optics,
Johannes Kepler University in Linz, Austria**

Research Assistant **06/2003-10/2003**

- topic: designed, optimized, simulated tapered structures for coupling light efficiently from a single-mode fiber to high-index contrast channel waveguide (SOI)
- Supervisor: Prof. Dr. Kurt Hingerl

SchlumbergerSema in West Union, SC, U.S.A.

Internship Trainee

01/2002-05/2002

- topic: involved in the design, testing of a frequency-hopping spread spectrum (FHSS) transceiver operating in the ISM band
- Supervisor: Dr. Larry Savage